



**FAKULTA  
STROJNÍ  
ČVUT V PRAZE**

# **Návrh injektoru pro raketový kapalinový motor na studentskou raketu**

**Design of liquid rocket engine injector for student  
rocket**

**Diplomová práce**

**Diploma thesis**

**Autor**

**Author**

**Daniel Hořejší**

**Vedoucí práce**

**Supervisor**

**Ing. Jaromír Kučera**

**2024**

## I. OSOBNÍ A STUDIJNÍ ÚDAJE

Příjmení: **Hořejší** Jméno: **Daniel** Osobní číslo: **482392**  
Fakulta/ústav: **Fakulta strojní**  
Zadávací katedra/ústav: **Ústav letadlové techniky**  
Studijní program: **Dopravní a transportní technika**  
Specializace: **Transportní technika**

## II. ÚDAJE K DIPLOMOVÉ PRÁCI

Název diplomové práce:

**Návrh injektoru pro raketový kapalinový motor na studentskou raketu**

Název diplomové práce anglicky:

**Design of liquid rocket engine injector for student rocket**

Pokyny pro vypracování:

Proveďte:  
Rešerši požadavků a konceptů injektoru  
Návrhové výpočty injektoru  
Konstrukční návrh včetně pevnostní kontroly  
Návrh testovací báze pro ověření funkčnosti návrhu

Seznam doporučené literatury:

Dle doporučení vedoucího

Jméno a pracoviště vedoucí(ho) diplomové práce:

**Ing. Jaromír Kučera ústav letadlové techniky FS**

Jméno a pracoviště druhé(ho) vedoucí(ho) nebo konzultanta(ky) diplomové práce:

Datum zadání diplomové práce: **26.04.2024**

Termín odevzdání diplomové práce: **24.05.2024**

Platnost zadání diplomové práce: \_\_\_\_\_

Ing. Jaromír Kučera  
podpis vedoucí(ho) práce

Ing. Milan Dvořák, Ph.D.  
podpis vedoucí(ho) ústavu/katedry

doc. Ing. Miroslav Španiel, CSc.  
podpis děkana(ky)

## III. PŘEVZETÍ ZADÁNÍ

Diplomant bere na vědomí, že je povinen vypracovat diplomovou práci samostatně, bez cizí pomoci, s výjimkou poskytnutých konzultací. Seznam použité literatury, jiných pramenů a jmen konzultantů je třeba uvést v diplomové práci.

\_\_\_\_\_  
Datum převzetí zadání

\_\_\_\_\_  
Podpis studenta

# ANOTAČNÍ LIST

Název práce: Návrh injektoru pro raketový kapalinový motor na studentskou raketu

Jméno autora: Daniel Hořejší

Rok: 2024

Ústav: Ústav letadlové techniky

Specializace: Kosmická technika

Vedoucí práce: Ing. Jaromír Kučera

Bibliografické údaje: Počet stran: 83

Počet obrázků: 62

Počet tabulek: 10

Počet grafů: 5

Počet příloh: 6

Klíčová slova: Studentská raketa, Raketový motor, Injektor, EuRoC, CTU Space Research

Abstrakt: Tato diplomová práce se zabývá funkčním a konstrukčním a návrhem injektoru pohonných látek, který bude použit v kapalinovém raketovém motoru. Tento motor je vyvíjen studentským týmem CTU Space Research na soutěž EuRoC. V rámci práce byl navržen první prototyp vstřikovače a obecný způsob ověření jeho parametrů a funkčnosti.

# ANOTATION SHEET

Thesis title: Design of liquid rocket engine injector for student rocket

Author: Daniel Hořejší

Year: 2024

Department: Department of Aerospace Engineering

Specialisation: Space technology

Thesis supervisor: Ing. Jaromír Kučera

Bibliographic data:

Number of pages:	83
Number of figures:	62
Number of tables:	10
Number of graphs:	5
Number of appendices:	6

Keywords: Student rocket, Rocket engine, Injector, EuRoC, CTU Space Research

Abstract: This diploma thesis deals with functional and structural design of a propellant injector, which will be used in a liquid rocket engine. This engine is being developed by a student team CTU Space Research for EuRoC competition. In the thesis the first injector prototype was designed and general means of verification of its parameters were proposed.

# ČESTNÉ PROHLÁŠENÍ

Prohlašuji, že jsem tuto diplomovou práci vypracoval samostatně pod vedením vedoucího práce a že jsem uvedl veškeré použité informační zdroje.

V Praze dne 25.5.2024

.....  
Daniel Hořejší

# Poděkování

Rád bych tímto poděkoval Ing. Kučerovy za vedení práce, přínosné konzultace a ochotu odpovídat na stálé dotazy.

Také bych chtěl poděkovat Ing. Teichmanovi za ochotu, nadšení a pomoc s programem Ansys.

Docentu Kanavalovi za cenné rady a pomoc při výpočtu šroubového spoje.

Pánům Plajdičkovi a Fílovi za jejich bezmeznou ochotu a pomoc při výrobě.

Kolegům Haisovi, Pírovi a Čechurovy za skvělou spolupráci při vývoji motoru.

Všem členů týmu CTU Space Research za jejich tvrdou práci a odhodlání.

Kamarádům Milošovi, Tonče a Lukášovi za ochotu, pomoc a rady při tvorbě práce.

Evičce a Philovy za pomoc při kontrole práce a vlídné povzbuzení.

V neposlední řadě bych rád poděkoval své rodině za obrovskou podporu ve všem, co dělám.

# Nomenclature

$A_F$	Fuel injection area [ $mm^2$ ]
$A_{Fmax}$	Maximum fuel injection area [ $mm^2$ ]
$A_{OX}$	Oxidizer injection area [ $mm^2$ ]
$A_{Pin}$	Inside area of the pintle [ $mm^2$ ]
$BF$	Blockage factor [1]
$c_D$	Discharge coefficient [1]
$D$	Flexural rigidity [ $N \cdot m^2$ ]
$D_F$	Annulus diameter [ $mm$ ]
$D_o$	Radial hole diameter [ $mm$ ]
$D_P$	Pintle diameter [ $mm$ ]
$D_{Pin}$	Inside diameter of the pintle [ $mm$ ]
$D_{Pin,max}$	Maximum inside diameter of the pintle [ $mm$ ]
$D_{Pin,ideal}$	Ideal inside diameter of the pintle [ $mm$ ]
$d$	Diameter [ $mm$ ]
$E$	Modulus of elasticity [ $GPa$ ]
$F$	Force [ $N$ ]
$F_P$	Force inside pintle [ $N$ ]
$h$	Plate thickness [ $mm$ ]
$h_m$	Manifold thickness [ $mm$ ]
$I_{sp}$	Specific impulse [ $N \cdot s \cdot kg^{-1}$ ]
$\dot{m}$	Mass flow [ $kg \cdot s^{-1}$ ]
$\dot{m}_F$	Fuel mass flow [ $kg \cdot s^{-1}$ ]
$\dot{m}_{OX}$	Oxidizer mass flow [ $kg \cdot s^{-1}$ ]
$N$	Number of radial holes [1]
$OF$	Oxidizer to fuel ratio [1]
$p$	Pressure [ $bar$ ]
$p_0$	Ambient pressure [ $bar$ ]
$p_c$	Combustion pressure [ $bar$ ]
$p_{Fmax}$	Maximum fuel pressure drop across injector [ $bar$ ]
$\Delta p_F$	Fuel pressure drop across injector [ $bar$ ]
$\Delta p_{OX}$	Oxidizer pressure drop across injector [ $bar$ ]
$Q$	Loading [ $N$ ]
$q_0$	Continuous load [ $N \cdot mm^{-2}$ ]
$r$	Radius [ $mm$ ]
$sf$	Safety factor [1]
$T_m$	Melting point [ $^{\circ}C$ ]
$t$	Loading per unit length [ $N \cdot m^{-1}$ ]
$TMR$	Total momentum ratio [1]
$v_F$	Fuel injection velocity [ $m \cdot s^{-1}$ ]
$v_{OX}$	Oxidizer injection velocity [ $m \cdot s^{-1}$ ]
$v_{manifold}$	Manifold velocity [ $m \cdot s^{-1}$ ]

# Nomenclature

$\alpha$	Resulting spray angle [ $^{\circ}$ ]
$\eta_{c*}$	Combustion efficiency [1]
$\eta_{cf}$	Nozzle efficiency [1]
$\theta_{pt}$	Angle of radial holes [ $^{\circ}$ ]
$\lambda$	Thermal conductivity
$\rho$	Density [ $kg \cdot m^{-3}$ ]
$\rho_F$	Fuel density [ $kg \cdot m^{-3}$ ]
$\rho_{OX}$	Oxidizer density [ $kg \cdot m^{-3}$ ]
$\nu$	Poisson's ratio [1]
$\sigma_D$	Allowed stress [ $MPa$ ]
$\sigma_{max}$	Maximum stress [ $MPa$ ]
$\sigma_r$	Radial stress [ $MPa$ ]
$\sigma_{red}$	Equivalent stress [ $MPa$ ]
$\sigma_t$	Tangential stress [ $MPa$ ]
$\sigma_{ult}$	Ultimate strength [ $MPa$ ]
$\sigma_y$	Yield strength [ $MPa$ ]
$\nu$	Poisson's ratio [1]
$\varphi$	Bending angle [ $deg$ ]



# Abbreviations

BF	Blockage factor
CAD	Computer Aided Design
CEA	Chemical Equilibrium Applications
CFD	Computational Fluid Dynamics
COTS	Commercial off-the-shelf
CTU	Czech Technical University in Prague
ECSS	European Cooperation for Space Standardization
EuRoC	European Rocketry Challenge
FEM	Finite Element Method
FOSU	Ultimate design factor of safety
FOSY	Yield design factor of safety
GSE	Ground Support Equipment
LOX	Liquid oxygen
MEOP	Maximum expected operational pressure
MDP	Maximum design pressure
NASA	National Aeronautics and Space Administration
OF	Oxidizer to fuel ratio
P&ID	Piping and instrumentation diagram
RCS	Reaction Control System
RP	Rocket Propellant
SRAD	Student researched and developed
SST	Shear stress transport
TMR	Total momentum ratio

# Table of contents

1	Introduction.....	12
1.1	Rules influencing the design .....	13
1.2	Concept overview .....	14
1.3	General design overview .....	16
2	Injector type selection.....	17
2.1	Injector types .....	17
2.1.1	Showerhead.....	17
2.1.2	Impinging elements .....	18
2.1.3	Splashplate .....	20
2.1.4	Pintle.....	21
2.1.5	Coaxial .....	23
2.1.6	Swirl .....	25
2.2	Selection criteria .....	27
2.3	Selection .....	28
3	Design calculations.....	30
3.1	Fluid calculations .....	30
3.1.1	Pintle sizing.....	32
3.1.2	Fuel sizing .....	34
3.1.3	Manifolding .....	36
3.2	Stress calculations.....	39
3.2.1	Material selection.....	40
3.2.2	Pintle wall stress calculations .....	42
3.2.3	Pintle thread stress calculations.....	43
3.2.4	Injector face stress calculations .....	45
3.2.5	Injector head stress calculations .....	48
3.2.6	Bolt connection stress calculation.....	51
4	CAD model.....	57

5	Design verification.....	58
5.1	FEM analysis.....	58
5.1.1	Pintle analysis .....	58
5.1.2	Manifold analysis.....	60
5.2	CFD analysis .....	64
5.2.1	Pintle analysis .....	64
5.2.2	Fuel manifold analysis .....	68
6	Testing campaign basis.....	71
6.1	Testing overview .....	71
6.2	Pressure testing .....	72
6.3	Cold Flow .....	74
6.4	Hot Fire .....	76
7	Conclusion .....	77

# 1 Introduction

This thesis aims to lay the groundwork for design, development, and verification of performance of a liquid rocket engine injector. The injector is part of an engine, which is being developed by CTU Space Research to power a sounding rocket with the goal of competing in the EuRoC competition.

CTU Space Research is a student organisation under Czech Technical University in Prague. Members include students from the faculty of mechanical engineering, faculty of electrical engineering, faculty of information technology as well as students from the Charles University. The team specializes in space related activities. The main annual project is a high-powered rocket developed for EuRoC. Side projects include the development of smaller rockets for component testing and competition in Czech Rocket Challenge and Stratosat projects for atmospheric experiments and testing of sensors avionics and communication.

European Rocketry Challenge is a competition for university students organised by the Portuguese Space Agency. Student teams compete by designing, building, testing and flying sounding rockets in multiple different categories, which are based on the propulsion type of the rocket and target apogee. The competition aims to improve learning, foster innovation, and motivate students to extend themselves beyond the classroom, while learning to work as a team, solving real world problems under the same pressures they will experience in their future careers. [1]

Injector is an essential part of a liquid rocket engine. It provides the combustion with the necessary fuel and oxidizer and influences propellant mixing and atomization, combustion stability and effectivity, and overall performance of the engine.

In this thesis, different injector types are going to be researched, described, and evaluated. Based on the evaluation, optimal injector type is going to be chosen.

Design calculations are going to be performed for the chosen injector type. These will include fluid calculations to ensure the injector meets the engine requirements and stress calculations to ensure adherence of the competition rules and safety of operation.

CAD model based on these calculations and injector design practices is going to be created. FEM analysis is going to be created to verify details of our design. CFD analysis is also going to be created to examine the pressure drops and injection velocities in the injector.

Test basis for testing campaign is going to be proposed. The purpose of this test basis will be to quantify the injector for operation, collect data to verify the design calculations and simulations and to make adjustments to the design to achieve desired operational parameters. The proposed campaign should ensure the engine performance meets the set requirements.

The outcome of this theses should be a design for the first prototype of the injector which is ready to be manufactured and tested according to the proposed testing campaign.

## 1.1 Rules influencing the design

In this chapter, rules influencing the design process of the engine are going to be presented, limitations are going to be explained and requirement competition proposed.

As mentioned in the Introduction, the EuRoC competition is divided into categories based on the propulsion type and target apogee. The categories can be seen in *Table 1.1*.

TARGET APOGEE		3000 M		9000 M	
Origin		COTS	SRAD	COTS	SRAD
Propulsion System	Solid	S3-c	S3	S9-c	S9
	Hybrid	H3-c	H3	H9-c	H9
	Liquid	L3		L9	

Table 1.1 Competition categories [1]

Our team decided to design the rocket for competing in the L9 category. This decision has been made for future flexibility. If the rocket does not perform as advertised or in case of any other unforeseen reason, the target apogee can be adjusted by lowering the burn time, and category can be changed to L3. Rules of the competition allow this change up until the final Technical report. [1]

Launch vehicles shall not exceed total impulse of 40 960 Ns. It is possible, to use multiple stage rockets or multi engine stages. SRAD motors should satisfy high safety requirements. The event officials evaluate the design during Technical Review Process based on technical reports and during flight readiness review. Only if event officials are fully convinced that the design is sufficiently sound, mature, and tested, will teams be allowed to fly. [1]

The engine must be pressure tested. Design burst pressure has to be at least 2 times the maximum expected operating pressure. (3 times if composite materials are used). Proof pressure test has to be performed at 1,5 times the maximum expected pressure for no less than twice the maximum expected system working time. It is also advised to perform a Burst Pressure Test. Hot-fire test of the whole system has to be performed. [1]

This means that proof of calculations, simulations and proof of testing has to be provided for all critical parts of the engine that are identified. It is a good practice to be able to prove a system reliability by a simple calculation, perform a simulation which yields similar results and perform a test to ensure reliability.

It is highly recommended that all propellant tanks are externally pressurized. Propellant loading and unloading process has to be tested and demonstrated. Propellants used have to be non-toxic or declared by the organisers as non-toxic. The system should be able to unload or vent the propellants remotely in case of launch abort. [1]

Launch vehicles have to have sufficient velocity when "departing the launch rail" to ensure stability and that they will follow predictable flight paths. A rail departure velocity of at least 30 m/s is generally acceptable. By exception, a team may request to use detailed analysis to prove stability is achieved at a lower rail departure velocity down to 25 m/s, either by computer simulation or by a test flight. The 30m/s lower take-off velocity is a requirement and not a guideline. [1]

Development of the system will be done with these rules and requirements in mind.

## 1.2 Concept overview

First part of the design process is going to be concept selection. Before we focus on designing the injector itself, we have to establish in what context is the part going to operate.

Based on the competition rules and our team capabilities. We decided to use single stage, single engine setup. We established, that the engine is going to use a pressure-fed cycle. The reason for this choice is the relatively small complexity and reliability of the pressure fed cycle as well as our inability to produce turbopumps.

Pressure-fed cycle uses high pressure gas to pressurize the propellant tanks and force the oxidizer and fuel into the combustion chamber. Ideal pressuriser gas is helium, because of its low density and low reactivity. However, we decided to use nitrogen, mainly because of price and accessibility. Nitrogen has also low reactivity, but this choice will make our system heavier.

Pressure-fed systems can be further divided into Regulated pressure systems and Blowdown systems.

Regulated pressure systems are more complex. They use pressure storage and regulators to keep constant pressure in main storage tanks. This allows the system to provide the engine with constant propellant flow and thus constant thrust, specific impulse and OF ratio. [4]

The Blow down system is simpler, it uses gas stored in the ullage volume of main propellant tanks. This however means, that pressure in the feed system decreases over time, which decreases thrust with burn duration, makes controlling mixture ratio less accurate and can cause blowbacks in the system. [4]

For our application Regulated pressure system was selected. The main reason behind this decision was the ability to control the mixture ratio and decrease the chance of blowback of the engine.

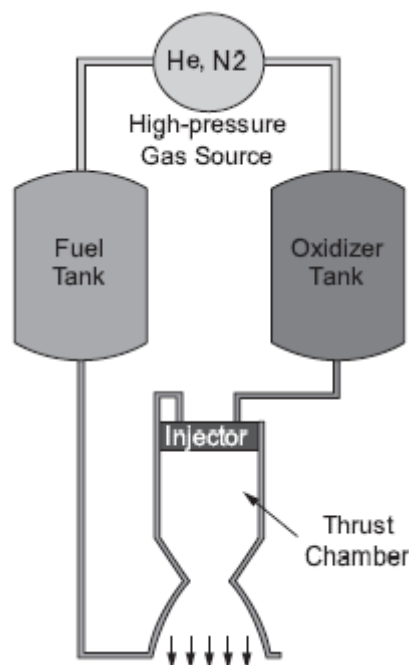


Figure 1.1 Pressure fed cycle schematic [3]

As mentioned before, pressure-fed cycle can be reliable and efficient in terms of propellant usage. Their main drawbacks are limited engine power due to main tank pressure limitation and subsequent chamber pressure limitation. Pressure-fed cycles also require heavier tanks to accommodate for the higher feed pressures.

The design of main propellant tanks is not going to be part of this thesis, however one of the outcomes should be the required pressure for these tanks in order to accommodate desired combustion characteristics.

The engine will use regenerative cooling. This will influence the pressure drop between the main fuel tank and injector. The development of the cooling system is not going to be part of this thesis. The pressure drop along the cooling jacket is going to be taken as an input value.

In cooperation with other colleagues. A combination of nitrous oxide as oxidizer and ethanol as fuel was selected. The selection process itself has considered safety, obtainability, performance, handling, and density.

This combination allows us to avoid cryogenic temperatures and does not require propellant cooling to function, however it rewards cooling by higher performance. These properties are ideal for future development of the system and provide us with opportunity to dive into low temperature operations without it being a requirement. These propellants are relatively safe and nontoxic according to EuRoC rules. They are easily obtainable by our team and provide sufficient specific impulse.

The engine will be supplied with propellants by a feed system on the engine test stand. Requirements on the test stand will be identified and calculated in Chapter 6.3. Based on the test results, rocket feed system requirements will be established. Engine and fluid system together will be referred to as propulsion system.

The rocket propulsion system is going to be serviced by a GSE, which will allow us to fill and unload our propellants remotely, thus enhancing safety. The requirements and general design of this system are going to be introduced in Chapter 1.3.



Figure 1.2 Purdue Space Programme Liquids GSE [15]

### 1.3 General design overview

This chapter will show general design process of the engine that influence our injector design based on the chosen concept, competition rules, requirements, team capabilities and experience.

From past experience a weight estimate of the rocket was made. For this weight estimate, target apogee and rule requirements an engine thrust and burn duration has been calculated using Open Rocket simulation program. These steps were taken in cooperation with other colleagues.

Based on team simulations an engine thrust of 5kN is required with a burn duration of 6s, giving our rocket a total impulse of 30 000 Ns, which is under the maximum impulse set by competition rules. These parameters will ensure desired rail exit velocity with enough reserve thus ensuring rocket stability according to the rules. The simulated apogee is 9 400m.[2] This value will change based on more accurate weight estimations and simulations and with data from hot-fire testing. Burn duration of 6s is therefore just and approximate design value. It should be noted, that in order to comply with competition rules, the engine with the desired thrust should not burn for longer than 8s.

Next step in the design process was to acquire combustion parameters. For this purpose, NASA CEA was used. Combustion pressure of 30 bars was examined. This pressure was chosen due to our experience from past engines and pressure feed system limitations. The analysis was done for our chosen propellant mixture with multiple OF ratios and after a discussion with other team members, OF ratio of 2 was chosen. This ratio does not have the highest possible specific impulse for this propellant combination but significantly lowers the combustion temperature and helps with cooling the engine. Chosen output data from the CEA simulation are displayed in *Table 1.2*.

Pressure ratio	$p_c/p_0$	[1]	37,5
Propellant ratio	$OF$	[1]	2
Molar gas constant	$R$	$[J \cdot K^{-1} \cdot mol^{-1}]$	2,262
Combustion temperature	$T_c$	[K]	2278,7
Specific heat ratio	$\kappa$	[1]	1,2634
Combustion pressure	$p_c$	[bar]	30
Exit Mach number	$M_e$	[1]	2,963
Throat to exit are ratio	$A_e/A_t$	[1]	5
Characteristic velocity	$C^*$	$[m \cdot s^{-1}]$	1491
Thrust coefficient	$c_f$	[1]	0,7005
Specific impulse	$I_{sp}$	$[N \cdot s \cdot kg^{-1}]$	2211,3

Table 1.2 Chosen CEA output data [2]

Other important data for the design process are the combustion chamber dimensions. These were obtained after a from a team member in charge of combustion chamber design. They are throat diameter and chamber diameter. [2]

$$D_t = 40,5 \text{ mm}$$

$$D_c = 90 \text{ mm}$$



## 2 Injector type selection

In this chapter different injector element types are going to be introduced, their pros and cons presented, and selection of an optimal design performed.

### 2.1 Injector types

There are several common element types among rocket engines which have been studied. Most common ones are going to be introduced in this chapter. It is important to note, that not every injector uses only one type of element. It is common to combine them to achieve desired performance, combustion stability and cooling characteristics.

#### 2.1.1 Showerhead

Showerhead injector type is the simplest option, it alternates axial feed holes of fuel and oxidizer. Mixing and atomisation are dependent on the holes and turbulence of the propellants entering the combustion chamber. [11]

This injector type has a poor mixing and atomisation characteristics and thus low combustion efficiency. Nowadays this design is almost never used, due to its inferior performance. [3] [5]

According to [3] this type of injector is relatively easy to manufacture and does not require precision machining. Reality can be somewhat different however as from firsthand experience manufacturing the hybrid engine injector was quite a challenge before suitable manufacturing techniques were discovered. Especially when a defect in one of the holes can mean a scrapped part.

This type of injector was used in one of the X-15 rocket plane engines, Aerobee sustainer engine and Pioneer spacecraft. In more modern engines, showerhead elements are used near the chamber walls due to their excellence for boundary layer cooling. [7]

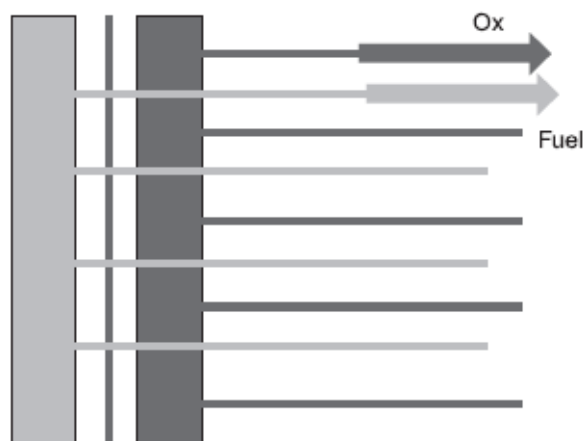


Figure 2.1 Showerhead injector schematic [3]

## 2.1.2 Impinging elements

There are several different configurations of impinging elements. In general, this injector type feeds propellants into the engine through set of holes which are drilled at a certain angle. Streams of the propellants collide and atomise.

A wide variety of configurations exist. Some of the more common configurations can be seen in *Figure 2.2* and will be introduced in higher detail.

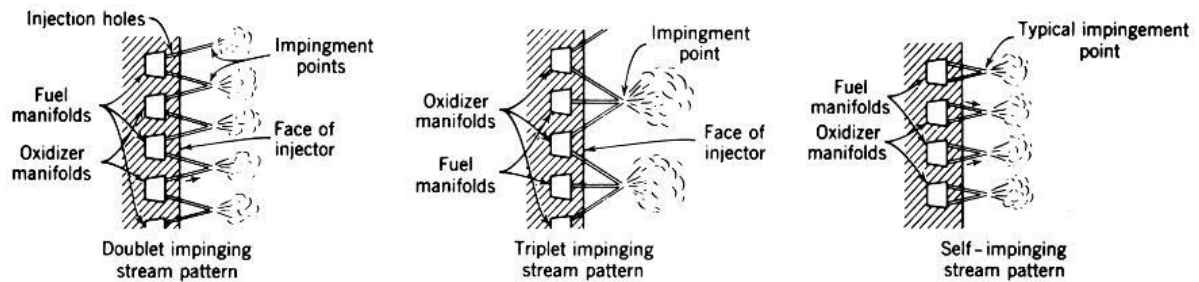


Figure 2.2 Most common impinging elements [11]

### Doublet

The unlike doublet is the most common element type. Fuel and oxidizer impinge with each other in pairs. This creates a fan shaped spray, which ensures large interfacial contact and causes good and uniform liquid phase mixing and good atomisation. This mixing occurs near the impingement point, which causes higher heat stress on the injector face and can be also cause of stream separation in hypergolic propellants. The mentioned elevated heat stress can be also present near chamber walls and cause chamber durability problems. [3] [6] [7]

This element is relatively easy to design. However, it requires tight manufacturing tolerances to work properly. The resulting momentum vector also varies with mixture ratio and this element is not easily throttleable. [6] [7]

### Triplet

In this configuration, two symmetrical outer jets imping together on one axial jet. This eliminates mismatch in stream size and momentum present in doublet elements and forms axially directed spray. This element achieves high level of mixing, combustion efficiency and performance. But it tends to have stability problems due to local variation in mixing. This variation can also cause chamber wall problems. [6] [7]

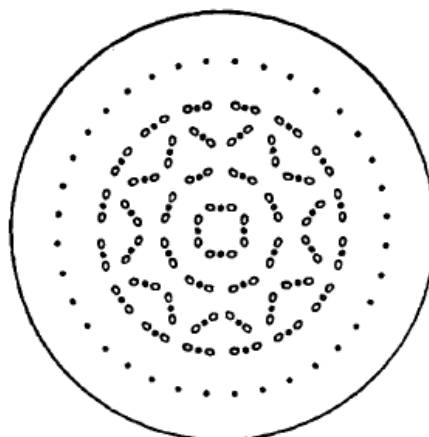


Figure 2.3 Triplet in bipropellant gas generator [5]

### Self-impinging

In this injector type, fuel and oxidizer imping separately in pairs. This forms thin liquid fan and achieves good atomisation. However, there is no mixing within these fans. Mixing happens as a result of interaction between adjacent fuel and oxidizer spray fans or by secondary impingement, this requires increased axial distance to mix fuel and oxidizer. [5] [7]

This arrangement has better combustion stability than unlike impinging patterns. As mentioned, initial mixing is worse, but good design can have a good performance and pretty high combustion efficiency. Furthermore, good arrangement of the elements can display a great wall compatibility and can be easier to manifold compared to other impinging elements. [5] [7]

This element was used for example in the famous F-1 engine powering the Saturn V first stage and Titan I first stage.[7]

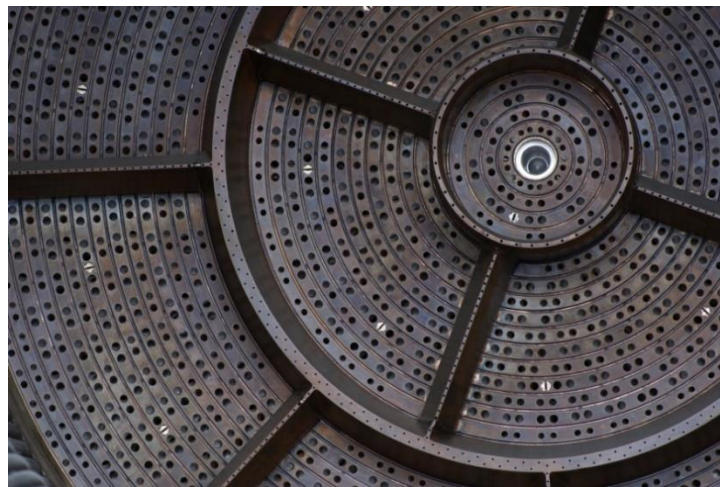


Figure 2.4 F-1 engine with self-impinging injector

Other types of impinging elements also exist. A quadlet has four streams of propellants with one pair of fuel and one pair of oxidizers impinging in one point. Pentad with four streams of one propellant impinging on one axial stream of the second propellant. This element can be used for engines with high OF ratios. [5] [11]

In general, impinging elements can have a high combustion efficiency and can be scalable. However, they are also quite complex and hard to manufacture. The tolerances needed to create the right impinging points, permit the desired mass flows and inject the propellants at desired velocities are tight and mostly out of reach for our current manufacturing capabilities. They also tend to have combustion stability issues. [11]

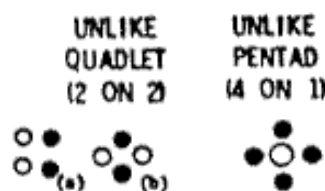


Figure 2.5 Configurations of quadlet and pentad [7]

### 2.1.3 Splashplate

In splashplate injector design, propellants are injected on and deflected by a splash plate, which is attached at a fixed angle at the end of a propellant line or at an intersection of the propellant streams. This creates broad flat sheet which expands and breaks into droplets. Similar to the impinging element, several options exist for impinging individual propellant streams, or combined propellant streams. It also creates similar flow fields downstream of the splashing location to the flow fields created by the impinging elements. [3] [8]

Performance of the splash plate is a function of splash plate angle, gap, and injector orifice size. In general, this element has generally low injection pressure loss, efficient atomisation, and good mixing characteristics. It also has good controllability and thus can be more easily throttled. It can also provide large thrust per element and increase performance for low performance elements. However, it does not further increase performance of high performing impinging elements. [7] [8]

As for manufacturability, the advantage is that this element does not require precise machining of the injection orifices and allows for looser tolerances. On the other hand, the splash plate itself adds additional surface and complexity to the design. Even though the plates are supposed to be cooled by the impinging liquids which should not ignite until they leave the splash plate, improper design, or change in combustion conditions can lead to problems with overheating and even burning of the splash plate when propellants impinge above the plate. [3] [5] [7]

In the US splashplate injectors were used before machining capabilities advanced to the point, where many developers were able to switch to the impinging element approach. This design was generally used in low thrust level assemblies with small number of orifices like Apollo crew module RCS or Gemini spacecraft manoeuvring engines. They have been also used in early version of Lence booster engines and in gas generators of larger engines. [3] [7] [8]

In amateur applications, spray nozzles have been used as injectors. These nozzles can also be counted as splashplate injectors. They provide off-the-shelf solution, which is easy to implement and has good performance characteristics. However, their application is more suitable for hybrid rocket engines.

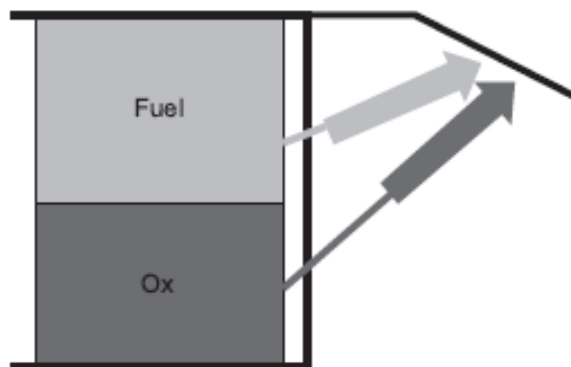


Figure 2.6 Liquid rocket engine splash plate schematic [3]

### 2.1.4 Pintle

Pintle injector is made up of annular hole and a concentric pintle. One of the propellants flows through the annular gap and the other one through the radial holes or slots at the tip of the pintle. The propellants usually impinge as radial jets hit the liquid film sheet at 90 degrees. This creates a spray with good mixing and atomisation. [3] [11]

Well-designed pintle injector can achieve very high combustion efficiency. It is also relatively simple as only single injector element is usually required. The performance can be optimized by varying the annular gap size and sizes and number of radial holes. Pintle element is relatively easy to throttle by controlling flow areas in both annulus and holes. This variation is usually done by translating sleeve. Pintle works well with engines, which need to be repeatedly restarted, because the pintle sleeve can serve as a face shutoff for these engines. This injector type is however not perfectly scalable as the mixing effectiveness drops with the larger size. This means, that it cannot be used for large engines, but this will not be an issue for our application.[3] [7] [8] [11]

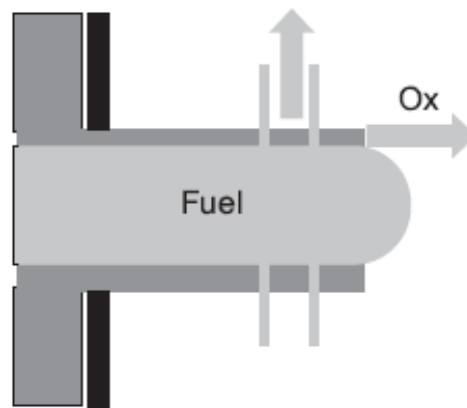


Figure 2.7 Pintle injector schematic [3]

This injector type is inherently stable. The spray created by this element is not perpendicular to the chamber and induces two separate recirculation zones, these zones have positive influences on the combustion stability and the recirculation zone at the centre of the engine enables the combustion zone to be brought into the centre of the combustor and leads to more rapid spray mixing. There has never been an instance of combustion instability associated with pintle engines. This property reduces risk, increases safety and is a huge advantage compared to other injector types. [3] [8] [10]

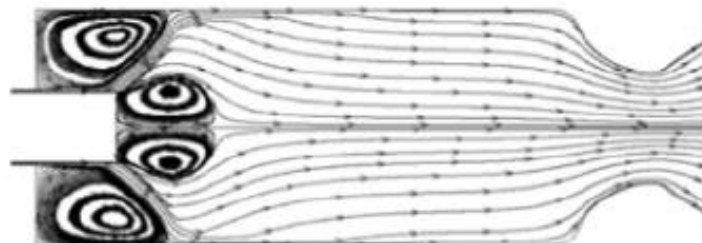


Figure 2.8 Recirculation zones created by the pintle injector [10]

A disadvantage of pintle injector is thermal stress concentration on the tip of the pintle which can lead to overheating. This element also does not have the best combustion wall compatibility and creates hotspots, regenerative cooling should be considered when using this injector type. [7] [11]

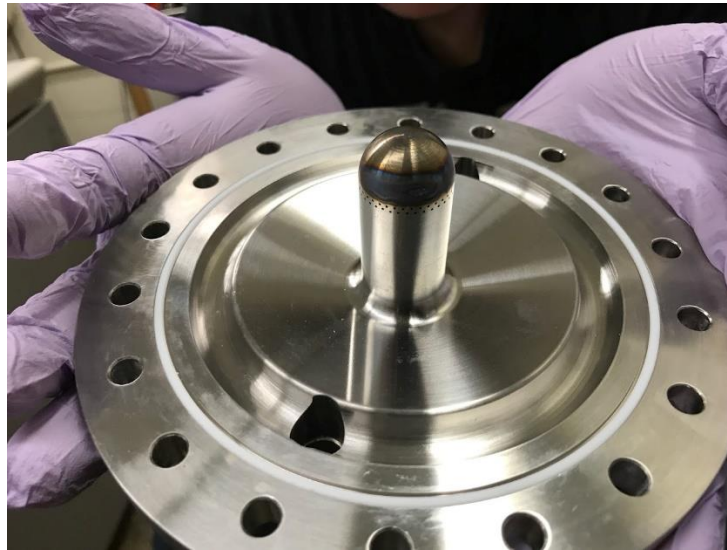


Figure 2.9 Thermal stress concentrated on the pintle tip [15]

Pintle is relatively simple and easy to manufacture since only one element needs to be made. All critical operations mostly consist of drilling holes normal to the local surface and alignment issues and tight tolerances present in other injector types are not present. As there is only one element, manifolding is inherently simpler than in other injector types. [7] [8]

This injector type has been extensively used for testing and operation with hypergolic propellants. It has been famously used in the Lunar Module descent engine and its derivative engine TR201 which has successfully powered the second stage of Delta Launch Vehicle. It is currently used by SpaceX on their Merlin engine and by Blue Origin on the BE-3 engine. It is also used by number of student teams, such as Purdue Space Programme and Delft Aerospace Rocket Engineering. [3] [7] [8] [12]

## 2.1.5 Coaxial

This type of injector consists of two concentric tubes which inject the propellants coaxially. [6] It is the most common type of non-impinging element. It has been used in both liquid/liquid and gas/liquid injectors. It is most suitable for cryogenic engines with fuels like hydrogen or methane, where the fuel absorbs heat from the cooling jacket or in the preburner and turns gaseous. [4] [5]

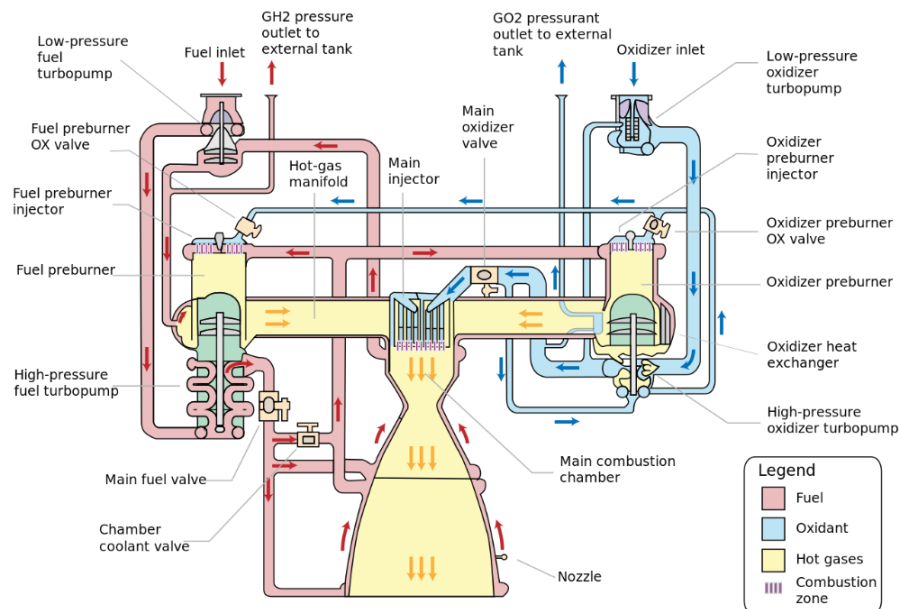


Figure 2.10 RS-25 engine schematic showing liquid/gas injection [16]

The mixing, atomisation and mass distribution are achieved by sheering action of high velocity gaseous fuel on a surface of a slow-moving liquid oxidizer. Typically, the fuel moves up to 10 times faster than the liquid oxidizer. This breaks up the oxygen stream into small droplets. The injector usually has number of elements on its face. The oxidizer tube, which is in the centre tends to be slightly submerged to isolate sensitive flame holding region at the post tip from pressure waves in the combustion chamber. [3] [4] [5]

The fuel surrounding the oxidizer shields, the combustion process and benefits combustion stability. Some engines, like the RS-25 use lengthened elements to serve as cooled baffles to further reduce incidence of combustion instability. For these conditions, the injector has high performance and stable injection. However, throttling the engine can cause combustion instabilities according to [7]. Since the oxidizer is injected under low velocity it has a low oxidizer pressure-drop. On the other hand, the fuel injection requires high pressure drop to achieve high velocity. [4] [5]

This element is thus less suited for liquid fuels. In liquid/liquid case the pressure drop required to achieve velocity relationships to make it work well is difficult to obtain. Therefore, it has poor mixing characteristics in this setting. [4][5]

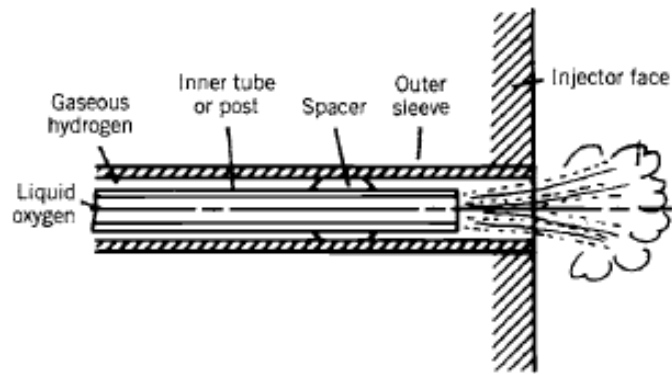


Figure 2.11 Coaxial injector element schematic diagram [4]

Although the geometry appears to be simple, it is quite complex and small changes in geometry can result in significant performance and stability changes. It requires precision manufacturing to ensure concentricity of the tube and surrounding injector body to maintain consistent oxidizer gap. However, sometimes these irregularities are done on purpose to divert oxygen from combustion walls to improve wall compatibility. Because of these requirements, alternative manufacturing methods like platelet injector designs have been used and patented by Aerojet Propulsion Company. [3] [4]

This element has been used in number of engines like American hydrolox engines RS-25, RL-10, M-1 and J-2. For liquid/liquid combination, it has been used in Surveyor vernier engine MIRA 150A. [7]

It is sometimes difficult to differentiate this kind of injector from swirl injectors, because some of the coaxial injectors also introduce a degree of swirl in the injection process.

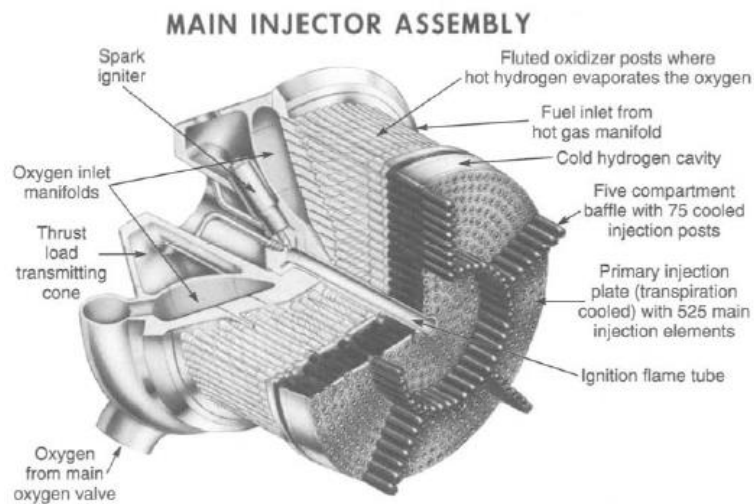


Figure 2.12 RS-25 main injector assembly [4]



## 2.1.6 Swirl

Swirl injector is similar to coaxial type. The difference is that in swirl injector elements, propellants enter their respective swirl chambers through several tangential holes which turn the momentum of injection into a swirling film. Alternatively, this rotating flow can also be generated using vanes positioned inside the chambers.[3] [8]

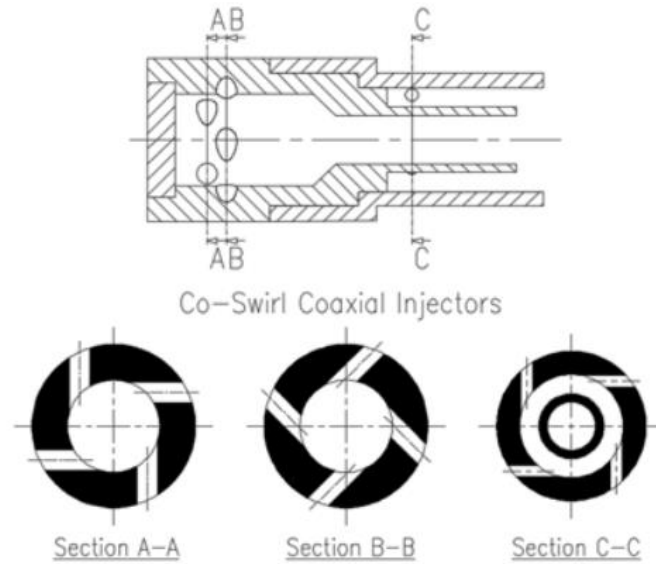


Figure 2.13 Schematic of bi-swirl coaxial injector [14]

These films either exit the injector as two conical sheets with different angles that intersect, rapidly mix, and atomize the propellants or as a conical oxidizer sheet impacting fuel, which is fed directly into the combustion chamber. The swirl injector is more suited for liquid/liquid injector than the coaxial one, it also works very well for gas/liquid or gas/gas injectors. It has relatively low pressure drop. In theory, this type has one of the highest combustion efficiencies and performance. [3] [11]

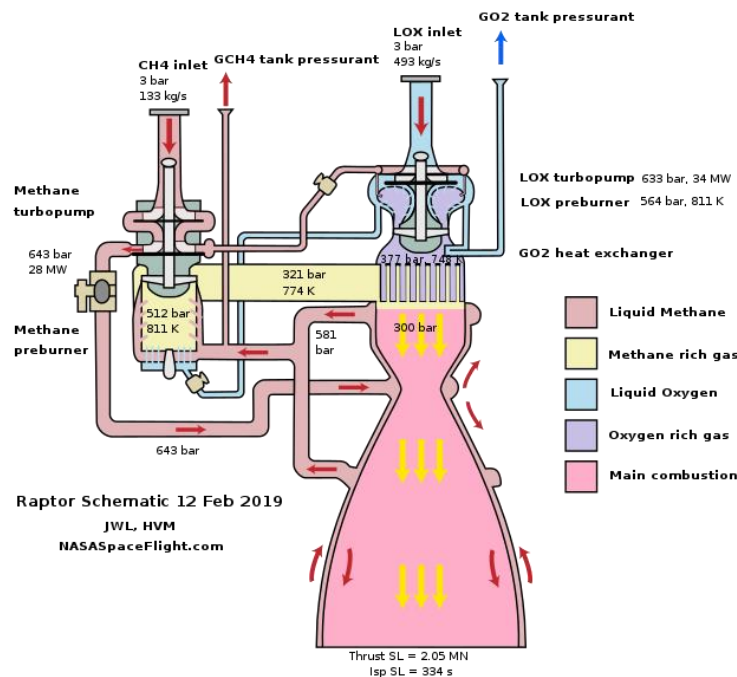


Figure 2.14 Raptor engine schematic showing gas/gas injection [17]

Once again similar to coaxial injector element, fuel tends to be more concentrated on the outer part of the sheet, which isolates the injector face and combustion walls from the hottest gasses. The element also responds to chamber pressure pulsations by forming small waves on the swirling film. It is believed this behaviour can either increase or dampen combustion instabilities depending on injector and chamber design conditions. It has been said that this element can become unstable when throttled. [3] [7]

Spray characteristics of swirl injectors are expressed by the spray cone angle, discharge coefficient, film thickness, breakup length, and droplet size/velocity, are influenced by the injector geometry and flow conditions. It is harder to optimize variables involved in swirling such as the speed and the angle at which the swirling oxidizer is injected for this injector type. [11] [14]

Splitting the injector face into number of elements, which are manufactured separately improves manufacturability. The elements can also have a simpler design and allow for looser tolerances than other designs. However, this increases number of parts and complexity of the injector as a whole. Manufacturing this type of injector remains quite difficult since small changes in concentricity can lead to changes in performance.

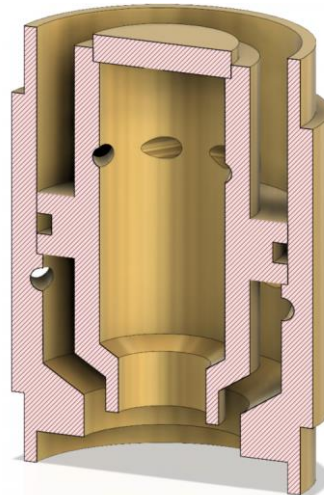


Figure 2.15 Swirl element used by Copenhagen suborbitals [18]

This injector type was used in RD-107, RD-170 and other Russian/Soviet engines and is also being used by Copenhagen suborbitals on BPM-5 and SpaceX on their Raptor engine. [9][13]

## 2.2 Selection criteria

To select optimal design for our application, trade-off analysis as advised by ECSS-E-ST-10C [20] will be used. Criteria, taken into consideration are complexity, manufacturability, combustion stability, combustion efficiency, access to information/experience and potential for future development. The options we are going to choose from are going to be the injector types listed in Chapter 2.1.

Notable characteristics not taken into considerations are wall compatibility, typical pressure loss and axial distance requirements.

After defining our criteria, we will determine the weight of each criterion. Usually, the weight is represented as a percentage of the decision with the sum being 100%. In my analysis, I will not stick to this rule and use numbering from 1 to 5 for better clarity.

Criteria	Justification	Weight
Complexity	Complexity of the design and price are important, but not critical factors in our selection. The biggest difference in complexity is usually due to manifolding.	1
Manufacturability	Since the injector needs to be manufactured on available equipment and with limited experience in precision manufacturing, manufacturability is a top priority in selecting the right design. The engine cannot exist, if its not in our capabilities to make it.	5
Combustion stability	Engine performance is a good indicator as long as the combustion is stable. Injector should give smooth combustion during engine transients and steady state operations. All systems with large amounts of energy have the potential for destructive oscillations, especially when there is a positive feedback loop present. Proper injector design should minimize accumulation within the combustion chamber of unburned propellants which could cause local detonations and thus trigger combustion instability. [5] [6]	4
Combustion efficiency	We want our engine to perform as well as possible. The efficiency of combustion is mainly influenced by propellant mass distribution, local mixture ratios, degree of mixing and droplet atomization and vaporization. Effective and even mixing of the propellants will be achieved through the choice of a suitable injector design. [6]	4
Access to information/experience	To design the injector, enough information and experience needs to be gathered. Our team does not have much practical experience with designing and testing injector designs in general. This makes theoretical sources a welcomed help.	2
Potential for future development	Potential for future development is important metric in our decision making. Philosophy of our team is making steady steps and building on previous experiences. This engine should serve as a baseline for future research of liquid rocket engines in our team. Selected design should be interesting for future development and improvement.	3

Table 2.1 Selection criteria

## 2.3 Selection

To evaluate the performance of each design, we will grade our options. This grading will be done on a scale of 1-5, with 5 being the best possible grade and by using the information obtained in Chapter 2.1. Grades for all injector types for all categories can be seen in *Table 2.2*.

Injector type	Criteria					
	Complexity	Manufacturability	Combustion stability	Combustion efficiency	Access to information	Future development
Showerhead	5	4	5	1	5	1
Impinging	3	1	2	3	4	4
Splashplate	2	3	3	4	1	3
Swirl	3	3	3	5	3	5
Pintle	4	5	5	5	3	5
Coaxial	2	2	4	2	2	2

Table 2.2 Grading of injector types

We can multiply each graded item by the weight assigned to the criteria. The resulting *Table 2.3* also shows the sum of points for each injector type. The injector type with the highest sum of points should be considered as the most optimal option.

Injector type	Criteria						Sum
	Complexity	Manufacturability	Combustion stability	Combustion efficiency	Access to information	Future development	
Showerhead	5	20	20	4	10	3	<b>62</b>
Impinging	3	5	8	12	8	12	<b>38</b>
Splashplate	2	15	12	16	2	9	<b>56</b>
Swirl	3	15	12	20	6	15	<b>71</b>
Pintle	4	25	20	20	6	15	<b>90</b>
Coaxial	2	10	16	8	4	6	<b>46</b>

Table 2.3 Grading with weights

As we can see from *Table 2.3*, the injector type with the highest score is the Pintle, with Swirl type in the second place. Since the grading system by itself does not necessarily show the entire picture a summary for each injector type and reasoning behind the selection is shown in *Table 2.4*.

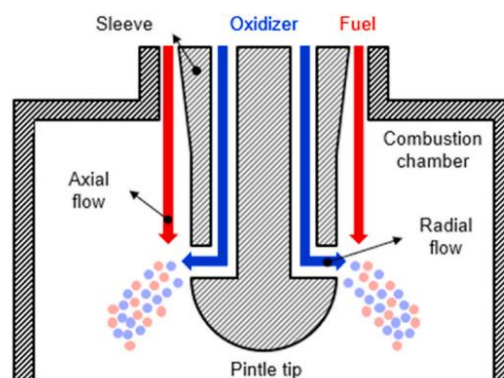


Figure 2.16 Schematic of a chosen injector type [19]

Injector type	Order	Injector type selection summary
Showerhead	3	Showerhead injector type scored high in complexity, manufacturability, combustion stability and access to information. Its main drawbacks were combustion efficiency and future development. This type was the simplest and safest option but did not offer much in terms of performance. Our team would also not be able to improve much on the design in the future.
Impinging	6	Impinging injector offered reasonable combustion efficiency, complexity and option for future development. This type suffered most in terms of combustion stability and manufacturability. It was concluded that it would be very difficult to design and manufacture this injector type properly. This fact would automatically disqualify impinging injector from further consideration.
Splashplate	4	Splashplate injector type was determined to be complex with relatively small number of sources to draw from. The complexity would also make manufacturing more difficult. Even though this type has reasonable combustion efficiency and potential for future development, it is not suitable as the basis for our injector. A splash element can however serve as a supplement to the chosen injector type.
Swirl	2	Swirl injector type was a strong candidate. It scored high in most categories. The main reason this injector type was not chosen were complexity and manufacturability. It would be much more difficult and time consuming to manufacture each element separately compared to other injector types. On the other hand, this element would be a great option if metal 3D printing was available due to its great combustion efficiency and option for future development.
Pintle	1	<b>Pintle injector type scored high in all categories. It is relatively simple, easy to manufacture, provides good combustion efficiency and great combustion stability. Furthermore, it allows for future development and improvements. It could for example be modified for thrust regulation. This makes the pintle injector the best option for our application.</b>
Coaxial	5	Coaxial injector type is not suitable for our application. Its main advantages result from the use of cryogenic propellants, which is not our case. It is complex and requires tight tolerances. Combustion efficiency with liquid sprays is also poor.

Table 2.4 Injector type selection summary

The selected Pintle injector has many possible configurations and design details. Since the engine will be regeneratively cooled, the injector will have oxidizer in the pintle with annular fuel flow around it. This configuration is called oxidizer centric pintle and can be seen in Figure 2.16.

With the main characteristics and concept chosen, more detailed calculations and design choices will be performed in Chapter 3.

## 3 Design calculations

In this chapter, analytical calculations are going to be performed. These calculations will give us an idea of the dimensions for the design of the injector. We will build on these calculations in Chapter 5, where more detailed simulations are going to be performed.

### 3.1 Fluid calculations

In this chapter, the main dimensions of the injector are going to be calculated and designed based on the manufacturing capabilities, engine requirements and common practices in pintle injector design.

First, we need to calculate the mass flow of propellants needed to supply the engine to achieve the desired thrust  $F$ . For this purpose, we will use Equation (3.1) which was introduced in source [3]. In this equation, we will use theoretical specific impulse  $I_{sp}$  from CAE simulation introduced in Table 1.2, nozzle efficiency  $\eta_{cf}$  and combustion efficiency  $\eta_{c*}$ . These efficiencies are introduced to better reflect the real-world scenario. According to source [3], typical combustion efficiencies range from 95% for well-designed LOX/RP engines to 99% for well-designed LOX/H<sub>2</sub> engines. We will be choosing a value of 0,95 as the lower of the mentioned cases. Arguably, this value could be even lower to give ourselves a higher margin of safety of achieving the prescribed thrust. The efficiency  $\eta_{cf}$  reflects nozzle divergence, boundary layer and kinetic losses. For large nozzles, this efficiency ranges around 97% to 99%, but for smaller nozzles, the value can drop to low 90s. For our case, we will choose a value of 0,92 as our engine is on the smaller side.

$$\dot{m} = \frac{F}{I_{sp} \cdot \eta_{c*} \cdot \eta_{cf}} = \frac{5\,000}{2211 \cdot 0,95 \cdot 0,92} = 2,587 \text{ kg/s} \quad (3.1)$$

Based on the OF ratio, we can divide the total mass flow into oxidizer mass flow and fuel mass flow.

$$\dot{m}_{OX} = \dot{m} \cdot \frac{OF}{1 + OF} = 2,587 \cdot \frac{2}{1 + 2} = 1,725 \text{ kg/s} \quad (3.2)$$

$$\dot{m}_F = \dot{m} \cdot \frac{1}{1 + OF} = 2,587 \cdot \frac{1}{1 + 2} = 0,863 \text{ kg/s} \quad (3.3)$$

Next, we will choose a pressure drop across the injector. The pressure drop across the injector is usually set at value from 15% to 25% of the combustion chamber pressure according to source [4]. Source [5] also mentions, that a good pressure drop starting point is 20% of the combustion pressure. Sufficient pressure drop will give us a good injection velocities. This aids atomisation and droplet breakup. We will use the 20% value as a pressure drop for the oxidizer inlet.

$$\Delta p_{OX} = 0,2 \cdot p_c = 0,2 \cdot 30 = 6 \text{ bar} \quad (3.4)$$

Knowing the pressure drop for the oxidizer, we can calculate the injection velocity of the oxidizer from Equation (3.5). In this equation, we will assume the previously calculated pressure drop  $\Delta p_{OX}$  of 6 bars and nitrous oxide density  $\rho_{OX}$  of  $755 \text{ kg/m}^3$ , which was taken from a Coolprop library for liquid state at room temperature. The equation also contains a discharge coefficient  $c_D$ , a starting value of 0,9 has been chosen for this coefficient. This value is on the high end of the values given in

source [3] and matches the value for short tube with rounded entrance and diameter of 1,57mm in *Figure 3.1*. The value of this coefficient will be further studied during Cold Flow testing and CFD simulations in Chapter 5.2.

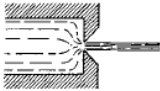
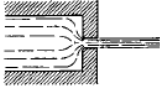
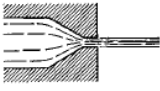
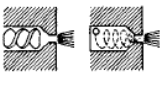
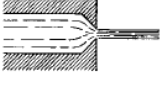
Orifice Type	Diagram	Diameter (mm)	Discharge Coefficient
Sharp-edged orifice		Above 2.5 Below 2.5	0.61 0.65 approx.
Short-tube with rounded entrance $L/D > 3.0$		1.00 1.57 1.00 (with $L/D \sim 1.0$ )	0.88 0.90 0.70
Short tube with conical entrance		0.50 1.00 1.57 2.54 3.18	0.7 0.82 0.76 0.84–0.80 0.84–0.78
Short tube with spiral effect		1.0–6.4	0.2–0.55
Sharp-edged cone		1.00 1.57	0.70–0.69 0.72

Figure 3.1 Injector discharge coefficients [4]

With all the values chosen, we can perform the calculation.

$$v_{OX} = c_D \cdot \sqrt{\frac{2 \cdot \Delta p_{OX}}{\rho_{OX}}} = 0,9 \cdot \sqrt{\frac{2 \cdot 6 \cdot 10^5}{755}} = 35,88 \text{ m/s} \quad (3.5)$$

The calculated injection velocity for oxidizer of 35,88 m/s should be sufficient for our application, prevent blowback of the engine and will be chosen for the first prototype of the engine. The pressure drop and resulting injection speed can be changed down the line based on the cold flow and hot fire testing data and are highly dependent on the parameters of the rocket feed system. However, for the first prototype of the engine, pintle MEOP will be set to 36 bars.

### 3.1.1 Pintle sizing

Design of the pintle from fluid point of view is mainly influenced by Equation (3.6) sourced from [3] and Equation (3.7). The value of blockage factor BF in Equation (3.6) should be approximately equal to 1. This ensures, that the whole pintle is covered by radial oxidizer spray, that can be impacted by the axial fuel flow from the annulus. The Equation (3.7) is simple mass flow equation and ensures, that the desired mass flow is supplied to the engine.

$$BF = \frac{N \cdot D_o}{\pi \cdot D_p} \quad (3.6)$$

$$\dot{m}_{OX} = A_{OX} \cdot v_{OX} \cdot \rho_{OX} \quad (3.7)$$

We can rewrite the Equation (3.7) to reflect our manufacturing method. To inject oxidizer from the pintle, we will use series of radial holes, the area is thus calculated as an area of one hole multiplied by the number of holes drilled. The decision to use radial holes, instead of rectangular slots was made to ease manufacturing. The slots would be better suited if oxidizer flow regulation was implemented due to the linear change of area resulting in linear change of oxidizer mass flow.

$$\dot{m}_{OX} = \frac{\pi \cdot D_o^2}{4} \cdot N \cdot v_{OX} \cdot \rho_{OX} \quad (3.8)$$

Pintle diameter  $D_p$  can be expressed by using the two introduced Equations (3.6) and (3.8). The resulting Equation (3.9) will be used for our calculations.

$$D_p = \frac{4 \cdot \dot{m}_{OX}}{v_{OX} \cdot \rho_{OX} \cdot \pi^2 \cdot D_o} \quad (3.9)$$

We already calculated the mass flow  $\dot{m}_{OX}$ , injection speed  $v_{OX}$  and know the oxidizer density  $\rho_{OX}$ . The radial hole diameter  $D_o$  is going to be dependent on the drill sizes available to us and be used as a variable we use to determine the pintle diameter  $D_p$  and number of radial holes  $N$ . The drill sizes examined range from 0,8 mm to 1,8 mm. The number of holes will be then calculated by Equation (3.10), which was derived from Equation (3.6) by substituting the desired value for blockage factor BF of 1.

$$N = \frac{\pi \cdot D_p}{D_o} \quad (3.10)$$

The values calculated for chosen hole diameters are displayed in *Table 1.1*. The values in the *Theoretical* columns are the exact values resulting from Equation (3.9) and Equation (3.10). The values in the columns titled *Chosen* are the values that were selected for each hole diameter. This is necessary to round the number of holes to a whole number and to set a diameter that has BF of 1 or slightly greater and that works with actual geometry of the injector that is going to be introduced in further chapters. The *Results* columns show the actual resulting mass flow and blockage factor for the chosen parameters. Highlighted in red is the selected combination of parameters.





### 3.1.2 Fuel sizing

Sizing of the fuel inlet annulus is going to be governed by Equation (3.11). The total momentum ratio TMR in this equation should be equal to 1 according to [3]. This would ensure a resulting spray of 45° degrees. We can however examine a wider variety of momentum ratios based on the angles they produce. The relation between total momentum ratio TMR and the angle of the resulting spray  $\alpha$  can be seen in Equation (3.12).

$$TMR = \frac{\dot{m}_F \cdot v_F}{\dot{m}_{OX} \cdot v_{OX}} \quad (3.11)$$

$$TMR = \tan \alpha \quad (3.12)$$

Equation (3.12) was derived from a relation between oxidizer and fuel spray seen in Figure 3.3.

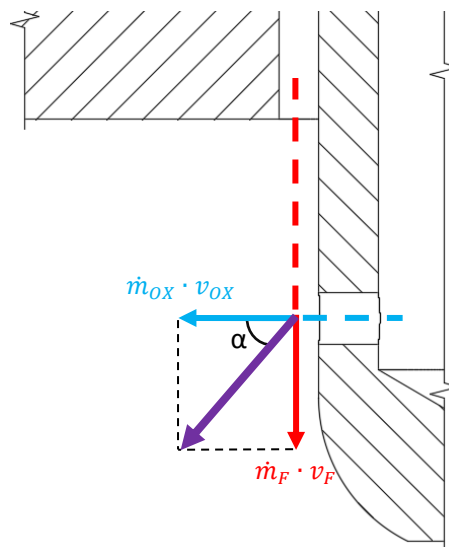


Figure 3.3 Relation between TMR and spray angle

We have already calculated oxidizer mass flow  $\dot{m}_{OX}$ , fuel mass flow  $\dot{m}_F$  and oxidizer injection speed  $v_{OX}$ . By putting together Equation (3.11) and Equation (3.12), we can derive a formula that will put fuel injection speed  $v_F$  as a function of resulting spray angle  $\alpha$ . The result can be seen in Equation (3.13).

$$v_F = \tan \alpha \cdot \frac{\dot{m}_{OX} \cdot v_{OX}}{\dot{m}_F} \quad (3.13)$$

Knowing the fuel injection speed  $v_F$ , we can rewrite a simple mass flow equation to obtain the required annulus area  $A_F$ .

$$A_F = \frac{\dot{m}_F}{v_F \cdot \rho_F} \quad (3.14)$$

We can also write a generic formula for computing the area of annulus.

$$A_F = \frac{\pi \cdot D_F^2}{4} - \frac{\pi \cdot D_P^2}{4} \quad (3.15)$$

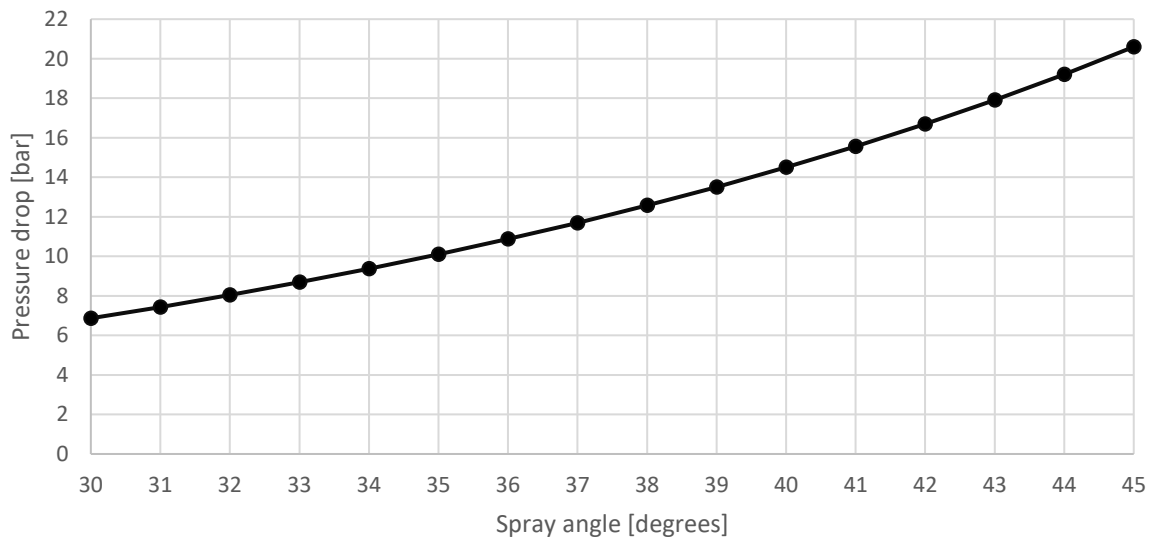
Outside diameter of the pintle  $D_P$  in Equation (3.15) was chosen in pintle sizing part of this chapter.  $D_F$  is the outside diameter of the annulus and also the diameter of the hole in the injector face. The value of the diameter  $D_F$  can be calculated from Equation (3.16), which was obtained by putting together Equation (3.14) and Equation (3.15).

$$D_F = \sqrt{\frac{4 \cdot \dot{m}_F}{\pi \cdot v_F \cdot \rho_F} + D_P^2} \quad (3.16)$$

Apart from calculating the dimensions of the annulus, we can also use the fuel injection speed  $v_F$ , fuel density  $\rho_F$  and discharge coefficient  $c_D$  to calculate the needed fuel pressure drop  $\Delta p_F$ .

$$\Delta p_F = \frac{v_F^2 \cdot \rho_F}{2 \cdot c_D^2} \quad (3.17)$$

Equations (3.13),(3.16) and (3.17) give us a direct relation, between the resulting spray angle  $\alpha$ , diameter of the injector face hole  $D_F$  and required fuel pressure drop  $\Delta p_F$ . We will mainly examine the relation between the resulting spray  $\alpha$  and required fuel pressure drop  $\Delta p_F$ , since pressure drop is the main requirement for the feed system and will have the biggest influence on the selection of final parameters. The required pressure drops depending on the resulting spray angles can be seen in *Graph 3.1*.



Graph 3.1 Relation between pressure drop and resulting spray angle

As can be seen in *Graph 3.1*, the angles examined range from 30° to 45°. After a careful consideration of the introduced variables several design decisions were made. For the initial pressure drop, we will be aiming for 10 bars with resulting spray angle of 35°. These values were chosen to not overstrain the fuel feed system. However, we still want to keep the ability to examine the option of TMR equal to 1 that was recommended by [3], if testing shows that this option is feasible, and the feed system

allows it. That is why the fuel injection part of the injector will be designed to withstand MEOP for the largest considered pressure drop, which is equal to 51 bars. The consequential stress calculation for this fact will be performed in Chapter 3.2.

We also want to have the ability to lower the needed pressure drop, if testing shows, that the feed system does not meet the desired performance. This decision will have two consequences. The first consequence are the dimensions of the annulus. To facilitate the mass flow for the lowest pressure drop, the annulus will have to be sized accordingly. The sizing of the annulus will be done for 6,87 bars, which corresponds to the resulting spray angle of 30°. This leads to a second major design decision. The pintle will be used to adjust the area of the annulus by having a taper and by having the ability to be moved by screwing. This results in a chosen connection between the pintle and the injector head in a form of a thread. This adjustment will be done in between testing and will not allow for active regulation of the fuel flow. It can however be further developed to perform this task.

Table 3.2 shows the results of the calculations and design decisions made in this chapter.

Design spray angle	Design fuel injection speed	Design fuel injection area	Annulus diameter	Design fuel pressure drop	MEOP for highest pressure drop	Design TMR
$\alpha$ [°]	$v_F$ [m/s]	$A_F$ [mm <sup>2</sup> ]	$D_F$ [mm]	$\Delta p_F$ [bar]	$p_{Fmax}$ [bar]	$TMR$ [-]
35	50,25	26,5	20,5	10,1	51	0,7

Table 3.2 Fuel sizing results

### 3.1.3 Manifolding

There are several different manifold types used for rocket engines. In general, manifolds are responsible for delivering propellants to the injector orifices. A well-designed manifold should produce a uniform flow with lowest possible pressure losses. To achieve these two requirements, we want our manifold volume to be as large as possible. However, this creates a problem with so called dribble volume. Volume of the manifold prolongs the engine startup and shutdown, during which the dribbled propellants combust at reduced pressures and with poor efficiency. This is especially an issue with engines which work in shorter pulses. [5] [7]

Dribble volume can be eliminated by using a face shutoff injector. Pintle is an ideal injector type for this solution. Face shutoff could be utilized during future development when active control of the injector is implemented for thrust regulation.

Oxidizer manifold will simply be the inner volume of the pintle. To calculate the ideal flow cross section for the pintle, we will use a rule of thumb introduced in source [5]. This rule states that manifold should have four times the flow area of the total area of injection orifices fed by it. This rule written as mathematical formula is shown in Equation (3.18).

$$A_{pin} = 4 \cdot A_{ox} \quad (3.18)$$

We know from Chapter 3.1.1 that the oxidizer injection area can be calculated by Equation (3.19).

$$A_{OX} = \frac{\pi \cdot D_o^2}{4} \cdot N \quad (3.19)$$

The inner cross section of the pintle can be calculated from Equation (3.20).

$$A_{Pin} = \frac{\pi \cdot D_{Pin}^2}{4} \quad (3.20)$$

By putting Equations (3.19),(3.20) and (3.18) together, we can form an Equation (3.21) for ideal inner pintle diameter in this manifold approach.

$$D_{Pin,ideal} = \sqrt{4 \cdot D_o^2 \cdot N} = \sqrt{4 \cdot 1,3^2 \cdot 48} = 18 \text{ mm} \quad (3.21)$$

From the value of the ideal inner diameter of the pintle and stress calculations for the pintle performed in Chapter 3.2.2, we can establish an actual value of the inner diameter of the pintle.

$$D_{Pin} = 17 \text{ mm}$$

For fuel manifolding, we will not select any specific manifold type described in [7]. Instead, we will design the fuel manifold to have a semi cylindrical shape. It will be fed from the cooling channels on the outer diameter and will deliver the propellant to the annulus located at the centre of the injector face. To design the dimensions of this manifold, we will combine two different approaches. The first approach taken from source [5] has been already used for the pintle where the area of the manifold should be 4 times larger than the area of the injector inlet. The second approach is introduced in source [7] and simply suggests, that the propellant speed in manifold should not go above 3 m/s.

For the first approach, we will take the largest possible injector fuel inlet area, which is calculated for the lowest expected pressure drop shown in *Graph 3.1*.

$$A_{Fmax} = 32,1 \text{ mm}^2$$

Flow area of a cylindrical manifold can be calculated by Equation (3.22).

$$A_F = \pi \cdot d \cdot h_m \quad (3.22)$$

From the fuel inlet area and manifold flow area, we can express Equation (3.23) that calculates the required manifold thickness at a given diameter  $d$ .

$$h_m = \frac{4 \cdot A_{Fmax}}{\pi \cdot d} \quad (3.23)$$

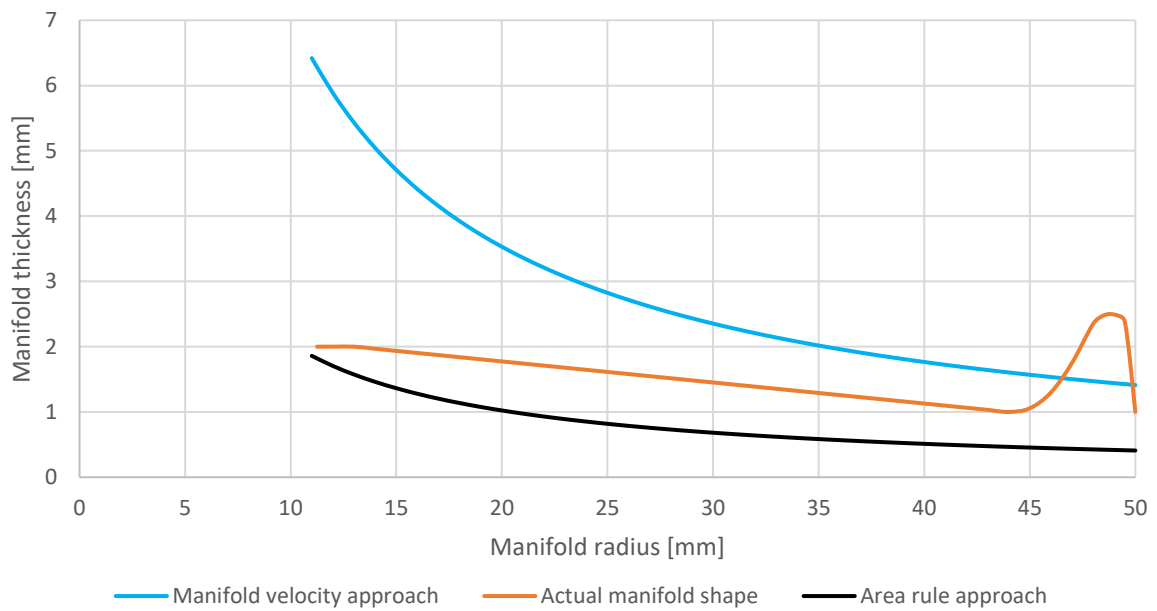
The second approach can be derived from a mass flow equation as shown in Equation (3.24).

$$A_F = \frac{\dot{m}_F}{v_{manifold} \cdot \rho_F} \quad (3.24)$$

By using Equation (3.22) and Equation (3.24), we can derive Equation (3.25) that determines the manifold thickness based on the fuel mass flow  $\dot{m}_F$ , fuel density  $\rho_F$ , manifold speed  $v_{manifold}$  and at a given diameter  $d$ .

$$h_m = \frac{\dot{m}_F}{v_{manifold} \cdot \rho_F \cdot \pi \cdot d} \quad (3.25)$$

Results from Equation (3.23) and Equation (3.25) for the two different approaches along with contour of the actual shape of the manifold acquired by iterative approach can be seen plotted in Graph 3.2.



Graph 3.2 Fuel manifold design

As can be seen from the Graph 3.2, the outer part of the manifold fulfils both approaches and serves as a ring manifold to ensure even fuel distribution. Rest of the fuel manifold is designed to only meet the area approach requirements. This design is done to lower the dribble volume while keeping the area needed for even distribution and low pressure losses. The fuel manifold was further studied in Chapter 5.2.2. Cutout detail of the pressure losses in the fuel manifold can be seen in Figure 5.23.

## 3.2 Stress calculations

Before doing more detailed design work, we need to find critical areas of our design and get an idea of the basic dimensions. To do that, we will make a basic drawing of the assembly and analyse it. The injector is going to be constructed of three main parts. The pintle, the injector face and the injector head. A simple drawing with the basic layout can be seen in *Figure 3.4*.

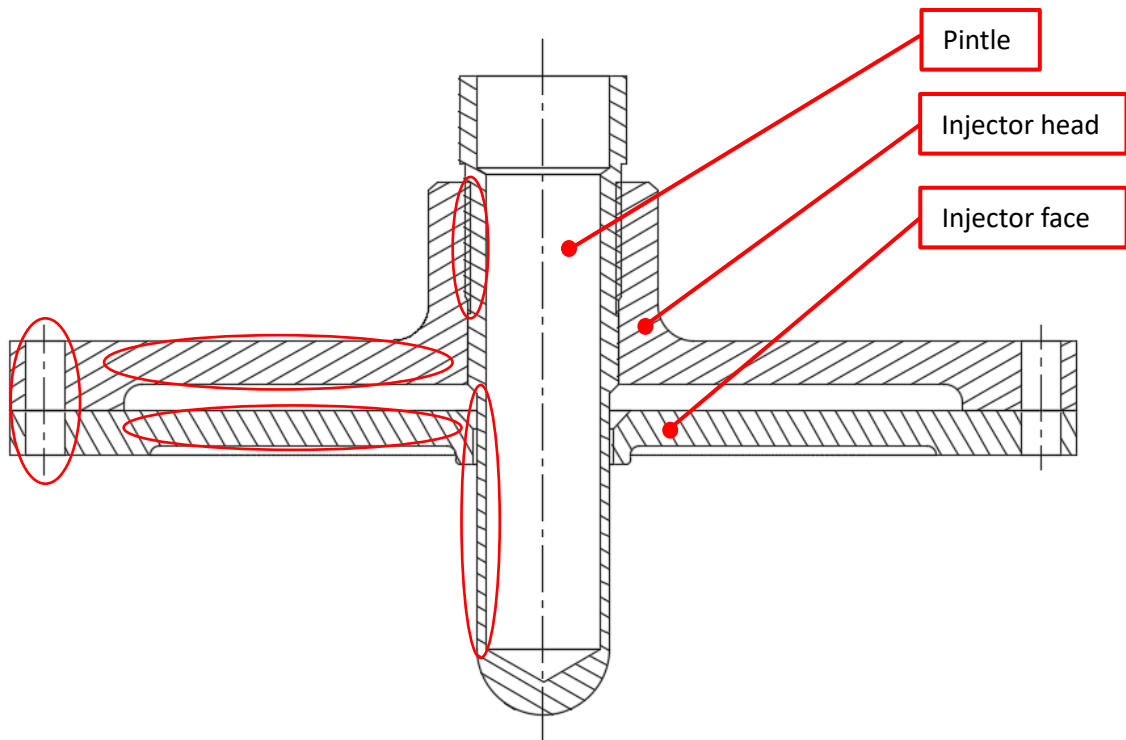


Figure 3.4 Basic layout of the injector

As we can see in *Figure 3.4* several critical areas of the design that need to be verified by stress calculations have been identified and circled in red. The calculations will be done for every part of the assembly in separate chapters. For the pintle, the minimum wall thickness has been determined as a point of concern. Load on the thread connecting the pintle to the injector head has also been deemed as a potential weak spot and will be checked. For the injector face design, the minimal plate thickness has been identified as critical. For the injector head, the smallest allowable thickness will be determined. The bolted connection between the injector face, injector head and chamber has been identified as a point of concern and will be calculated in detail.

### 3.2.1 Material selection

Before performing calculations for the critical parts, a material selection is going to be performed for all components of the injector assembly. There are a few materials suggested by source [7]. These materials include stainless steels, copper alloys, aluminium alloys and nickel alloys such as Inconel. The selection was also aided by information obtained from ECSS-Q-ST-70-71C Rev.1. [22]

Ideally, we want our chosen materials to be corrosion and heat resistant, light weight, strong and easy to process. But most importantly, the materials must be obtainable. Inquiry was made to suppliers and sponsors and the materials available for our project and their properties are listed in *Table 3.3*.

Material	Type	Yield strength	Ultimate strength	Modulus of elasticity	Density	Poisson's ratio	Melting point	Thermal conductivity
-	-	$\sigma_y$	$\sigma_{ult}$	E	$\rho$	$\nu$	$T_m$	$\lambda$
-	-	[MPa]	[MPa]	[GPa]	[ $kg/m^3$ ]	[1]	[°C]	[ $W/(m \cdot K)$ ]
Stainless	1.4057	739 <sup>1)</sup>	924 <sup>1)</sup>	210 <sup>5)</sup>	7 700 <sup>5)</sup>	0,3 <sup>5)</sup>	1450 <sup>5)</sup>	25 <sup>5)</sup>
Aluminium	EN AW7075-T6	503 <sup>2)</sup>	572 <sup>2)</sup>	71,7 <sup>2)</sup>	2 810 <sup>2)</sup>	0,33 <sup>2)</sup>	477 <sup>2)</sup>	130 <sup>2)</sup>
Copper	EN 13601	50 <sup>3)</sup>	200 <sup>3)</sup>	117 <sup>3)</sup>	8 920 <sup>3)</sup>	0,34 <sup>4)</sup>	1083 <sup>3)</sup>	391 <sup>3)</sup>
Brass	EN 12164	230 <sup>3)</sup>	360 <sup>3)</sup>	97 <sup>3)</sup>	8 470 <sup>3)</sup>	0,31 <sup>4)</sup>	875 <sup>3)</sup>	123 <sup>3)</sup>
Titanium	6Al-4V	869 <sup>6)</sup>	920 <sup>6)</sup>	113,8 <sup>2)</sup>	4 430 <sup>2)</sup>	0,342 <sup>2)</sup>	1604 <sup>2)</sup>	6,7 <sup>2)</sup>
1) Documentation provided by the supplier [23] 2) Values taken from source [24] 3) Values taken from source [25] 4) Values taken from source [26] 5) Values taken from source [27] 6) Internal CTU Space Research documentation [2]								

Table 3.3 Properties of selected materials

Injector face is highly stressed part that form the closed end of the combustion chamber. It may be subject to combustion products and suffer thermal strains. Injector face is associated with large portion of mechanical failures of injectors. [7] For our design, stainless steel 1.4057 was chosen. This material was chosen due to good corrosion and heat resistance and great mechanical properties. It is also obtainable in the desired dimensions. Processing of this material is outside the capabilities of our workshop and will be outsourced.

Injector face is going to be manufactured from, aluminium alloy 7075-T6. Aluminium was chosen for its low density and high strength. It is also obtainable in the desired dimensions, and it can be processed in our team workshop. Injector head is going to be loaded by the manifold pressure of the fuel. Temperature of the fuel will be elevated from chamber cooling. This introduces an unknown variable to our design process because the heat loading of the part will be determined during the first hot fire. The operational duration of the engine suggests that heat stress should not be a concern. However, the part will still be verified with higher factor of safety since mechanical properties of aluminium decrease with elevated temperatures. The part will be modified during future iterations based on the data obtained from the testing campaign.



The pintle is going to be stressed by the oxidizer pressure and by heat from the combustion. Brass was chosen for the first prototype because it is easy to process and has reasonable mechanical and thermal properties. Manufacturing of one of the early prototypes can be seen in *Figure 3.5*. All stress calculations will be done for this material. Furthermore, a thermal analysis of the pintle is going to be performed in Chapter 5.2.1. Outcome of this analysis will aid us in the material selection for the final design that will be utilized during the first hot fire. Ultimately, the final design of the pintle will probably utilize titanium 6AL-4V which was provided to our team by a sponsor. This change will lower the weight of the part, improve the heat resistance, and increase the allowable oxidizer pressure. Condition for using titanium is going to be our ability to process this material.



Figure 3.5 Manufacturing of the first pintle prototype from brass

The injector assembly will be constructed from different materials some of which have very different electropotential, which is visible in *Figure 3.6*. This increases the risk of galvanic corrosion. Since the assembly will not operate for long periods of time, no precautions are going to be made. However, presence of galvanic corrosion will be monitored and if any signs of galvanic corrosions are found, zinc plating will be used as sacrificial anode.

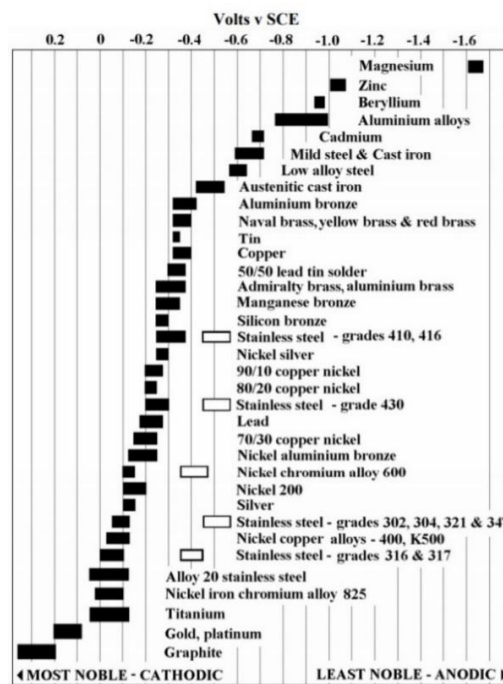


Figure 3.6 Galvanic table [28]

### 3.2.2 Pintle wall stress calculations

First thing we will calculate is the minimal wall thickness of the pintle. We can approximate the pintle as internally pressurized cylinder with non-negligible wall thickness. For calculations under this approximation, we will use the theory and equations introduced in sources [30] and [31]. For wall thickness calculation under this approximation, it does not matter if the pressure vessel is closed off or if it has open ends. As we can see from the Figure 3.7 the biggest stress concentration is on the inner wall of the vessel.

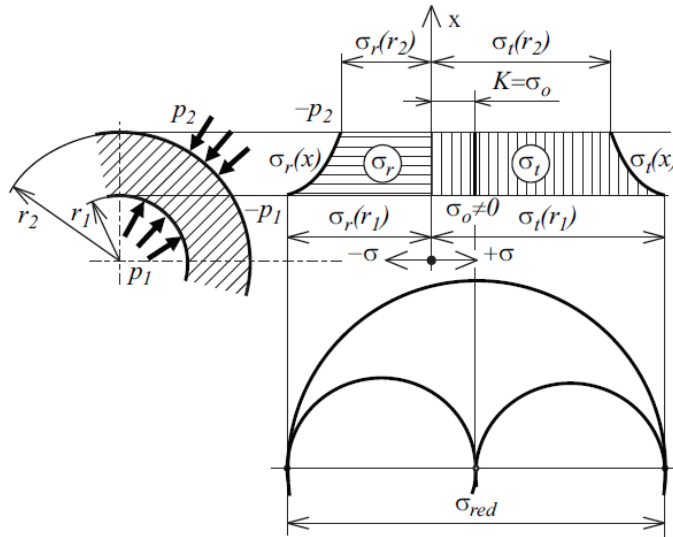


Figure 3.7 Stress distribution in internally pressurized vessel [30]

Using maximum shear stress approach, we can calculate the critical stress as difference between circumferential and radial stress. As mentioned, this fact can also be seen in Figure 3.7.

$$\sigma_{red} = \sigma_t(r_1) - \sigma_r(r_1) \leq \sigma_D \quad (3.26)$$

After substituting the formulas for radial and circumferential stresses we get a general equation for internally pressurized vessels.

$$\sigma_{red} = 2 \cdot \frac{p_1 \cdot r_1^2 - p_2 \cdot r_2^2}{r_2^2 - r_1^2} + p_1 - (-p_1) \quad (3.27)$$

We can simplify this formula and derive the commonly used Equation (3.28) for allowed pressure difference.

$$(p_1 - p_2) \leq \frac{\sigma_D}{2} \cdot \left[ 1 - \left( \frac{r_1}{r_2} \right)^2 \right] \quad (3.28)$$

By rearranging Equation (3.28), inputting the outer radius of the pintle, MEOP set in Chapter 3.1 and yield stress for our chosen material divided by safety factor, we can obtain a formula for the maximum inner radius of the pintle. The outer pressure will be taken as zero. This simplification will make our calculation more conservative.

$$r_{1max} = \sqrt{r_2^2 - \frac{2 \cdot r_2^2 \cdot (p_{OX} - p_0)}{\frac{\sigma_y}{sf_p}}} = \sqrt{9,75^2 - \frac{2 \cdot 9,75^2 \cdot (3,6 - 0)}{\frac{230}{2}}} = 9,44 \text{ mm} \quad (3.29)$$

Knowing the value of maximum inner radius, we will choose an actual diameter, that we are able to manufacture by drilling and that also leaves enough material so that we do not crumple the walls during milling.

$$D_{pin} = 17 \text{ mm}$$

A consideration was also given to a case, where the pintle is in the injector with fuel flowing and no pressure inside of the injector. This case would not be a standard occurrence during operation and could potentially occur in only two cases. A fuel-only cold flow and a pressure test. During a pressure test, only part with non-critical thickness of the pintle is going to be stressed. During a fuel-only cold flow test, the pressure drop will ensure, that the critical part of the pintle is not overstressed. This pressure drop can be seen in *Figure 5.22* and *Figure 5.24* in Chapter 5.2.2. The most critical loading case will be taken from Chapter 5.2.1 where the result of the pintle simulation showed a possibility, of the oxidizer pressure reaching 40 bars. The maximum stress will be calculated in Equation (3.30).

$$\sigma_{max} = \frac{2 \cdot (p_{OX} - p_0)}{1 - \left(\frac{r_1}{r_2}\right)^2} = \frac{2 \cdot (4 - 0)}{1 - \left(\frac{8,5}{9,75}\right)^2} = 33,34 \text{ MPa} \quad (3.30)$$

We can take the critical value of stress and calculate factor of safety according to ECSS standards.

$$FOSY_{pintle} = \frac{\sigma_y}{\sigma_{max} \cdot sf_p} = \frac{230}{33,3 \cdot 2} = 3,45 \quad (3.31)$$

$$FOSU_{pintle} = \frac{\sigma_{ult}}{\sigma_{max} \cdot sf_p} = \frac{360}{33,3 \cdot 2} = 5,4 \quad (3.32)$$

The safety factor for the pintle  $sf_p$  was taken as 2, which is the default value set by the competition rules. As we can see from Equations (3.31) and (3.32), the both factors of safety is are well above the threshold set by the competition rules, this means the pintle meets the competition requirements.

### 3.2.3 Pintle thread stress calculations

The next part of the pintle that has been identified as critical is the thread connecting the pintle to the injector head.

First step in analysing the pintle thread is going to be finding the critical force acting upon this connection. This highest force identified is caused by the inner pressure acting axially on the pintle. This force is calculated in Equation (3.33) and will be present during an oxidizer only cold flow. A force caused by the fuel pressure acting axially during a fuel only cold flow on the pintle taper was also considered but was not deemed critical compared to the inside pressure force. During normal

operation these two forces will be acting opposite to each other, thus not being as critical. The value  $d_{pinmax}$  is the largest inside diameter of the pintle taken from the 3D model.

$$F_P = p_{OX} \cdot \frac{\pi \cdot d_{Pin,max}^2}{4} = 3,6 \cdot \frac{\pi \cdot 19^2}{4} = 1\,021\,N \quad (3.33)$$

Based on the outside diameter of the pintle, the taper needed for closing the anulus and wall thickness calculations, thread M24x1 has been chosen. Thread stripping failure, that can be seen in *Figure 3.8*, has been identified as the only critical failure mode. To calculate the stress acting on the thread, we will be using Equation (3.34). The value  $z$  in this equation is the number of active threads and the values  $d_2$  and  $H_1$  are parameters of the chosen thread.

$$\sigma_{max} = \frac{F_P}{z \cdot \pi \cdot d_2 \cdot H_1} = \frac{1021}{8 \cdot \pi \cdot 23,35 \cdot 0,542} = 3,21\,MPa \quad (3.34)$$

We can see that the chosen thread will not be critically loaded, and the factors of safety will not be calculated. Furthermore, the stress value is low enough to consider using a screw thread mechanism for fuel regulation in further development of the injector.

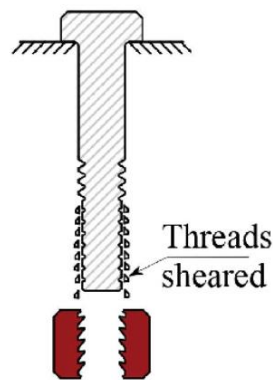


Figure 3.8 Thread stripping failure [33]

In addition to performed stress calculations, the pintle tip will also require special attention. However, the material thickness of the tip is more influenced by manufacturing methods and heat stress than by mechanical stress. Heating of the pintle tip is going to be studied in Chapter 5.2.1.

### 3.2.4 Injector face stress calculations

To calculate the thickness of the injector face, we will approximate the part as a thin circular plate, with a hole in the middle and clamped edges. For calculations we will use the theory and equations introduced in sources [30] and [31]. The most critical loading case will be during cold flow, when there will be pressure stressing the part from the top and no pressure on the bottom. A simplified schematic of our case used for the calculations can be seen in *Figure 3.9*.

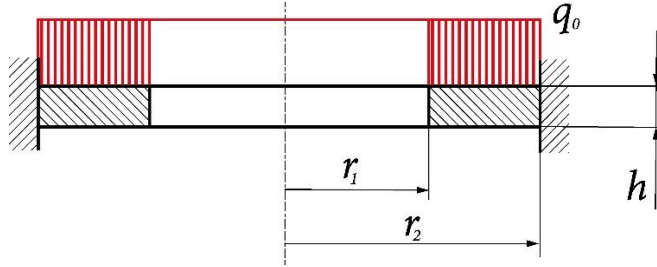


Figure 3.9 Injector face calculation schematic [2]

Coordinates of the plate range from the radius of the hole  $r_1$  to the outer radius of the plate  $r_2$ . This can be expressed as interval that can be seen in Equation (3.35).

$$x \in (r_1; r_2) \quad (3.35)$$

For circular plate with clamped edges and hole in the middle, the following boundary conditions need to be fulfilled. The angle at the outer diameter  $\varphi(r_2)$  needs to be equal to zero and the radial stress at the inner diameter of the plate  $\sigma_r(r_1)$  needs to be equal to zero. We can see these boundary conditions written in Equation (3.36) and Equation (3.37).

$$\varphi(r_2) = 0 \quad (3.36)$$

$$\sigma_r(r_1) = 0 \quad (3.37)$$

The used theory introduces general differential Equation (3.38) for loaded thin circular plates.

$$\left[ \frac{1}{x} \cdot (\varphi(x) \cdot x)' \right]' = -\frac{t(x)}{D} \quad (3.38)$$

For our case, loading per unit length is calculated in Equation (3.39). Where continuous loading  $q_0$  will be equal to fuel MEOP of the highest possible pressure drop  $p_{Fmax}$  determined in Chapter 3.1.2.

$$t(x) = \frac{Q(x)}{2 \cdot \pi \cdot x} = \frac{q_0 \cdot \pi \cdot (x^2 - r_1^2)}{2 \cdot \pi \cdot x} = \frac{q_0 \cdot (x^2 - r_1^2)}{2 \cdot x} \quad (3.39)$$

Flexural rigidity of the flat plate is expressed in Equation (3.40). Where  $E$  is the Young's modulus,  $\nu$  is the Poisson's ratio and  $h$  is the thickness of the plate.

$$D = \frac{E \cdot h^3}{12 \cdot (1 - \nu^2)} = \frac{E^* \cdot h^3}{12} \quad (3.40)$$

By inserting Equation (3.39) and Equation (3.40) into Equation (3.38) we obtain a differential equation for our load case.

$$\left[ \frac{1}{x} \cdot (\varphi(x) \cdot x)' \right]' = - \frac{12 \cdot q_0 \cdot (x^2 - r_1^2)}{2 \cdot x \cdot E^* \cdot h^3} \quad (3.41)$$

To simplify further calculations, we will make substitutions shown in Equation (3.42) and Equation (3.43).

$$B = \frac{6 \cdot q_0}{E^* \cdot h^3} \quad (3.42)$$

$$C = \frac{6 \cdot q_0 \cdot r_1^2}{E^* \cdot h^3} \quad (3.43)$$

After implementing these substitutions, we receive a differential Equation (3.44).

$$\left[ \frac{1}{x} \cdot (\varphi(x) \cdot x)' \right]' = -B \cdot x + \frac{C}{x} \quad (3.44)$$

By integrating Equation (3.44), we can obtain general solution for bending angle of the plate as can be seen in Equation (3.45).

$$\varphi(x) = -\frac{B \cdot x^3}{8} + C \cdot \left( \frac{x \cdot \ln(x)}{2} - \frac{x}{4} \right) + \frac{C_1 \cdot x}{2} + \frac{C_2}{x} \quad (3.45)$$

Rate of angle change can be obtained by derivation and can be seen in Equation (3.46).

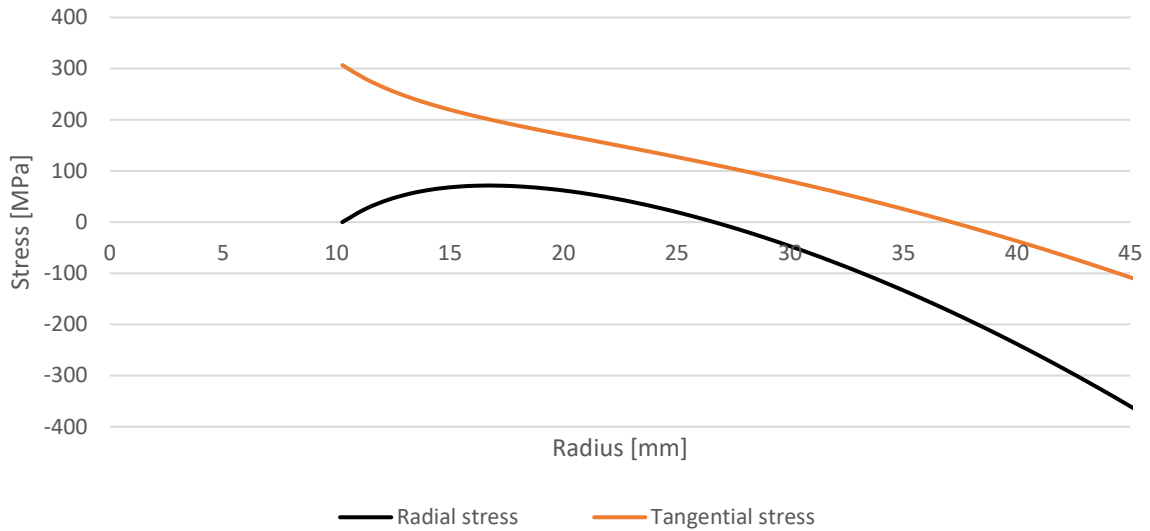
$$\varphi'(x) = -\frac{3 \cdot B \cdot x^2}{8} + C \cdot \left( \frac{\ln(x)}{2} + \frac{1}{4} \right) + \frac{C_1}{2} - \frac{C_2}{x^2} \quad (3.46)$$

To complete the calculation, we need to calculate the constants  $C_1$  and  $C_2$  using the boundary conditions set in Equation (3.36) and Equation (3.37). After doing so, we can combine the results with Equation (3.47) and Equation (3.48).

$$\sigma_r(x) = E^* \cdot \frac{h}{2} \cdot \left( \varphi'(x) + \nu \cdot \frac{\varphi(x)}{x} \right) \quad (3.47)$$

$$\sigma_t(x) = E^* \cdot \frac{h}{2} \cdot \left( \frac{\varphi(x)}{x} + \nu \cdot \varphi'(x) \right) \quad (3.48)$$

The inner radius  $r_1$  is directly related to the outer diameter of the annulus calculated in Chapter 3.1.2 and will be equal to 10,25 mm. The outer radius of the plate  $r_2$  was determined by the chamber dimensions and will be equal to 45 mm. Plate thickness was iterated until desired properties of the plate were reached. The final thickness was 4,5 mm. By substituting this plate geometry along with the properties from Table 3.3 for our chosen material to equations derived in this chapter, we can plot Graph 3.3.



Graph 3.3 Injector face stress distribution

Graph 3.3 shows stress distribution in the plate for our case. As we can see, the most critical loading will be on the outer edge of the plate. We can deduce the largest magnitude of stress.

$$\sigma_{max} = -366 \text{ MPa}$$

The calculation can be compared to results for a similar case obtained by using calculation software MITcalc. The critical value given by this software can be seen below.

$$\sigma_{max} = -367 \text{ MPa}$$

As we can see, our results match the results from MITcalc software, which can give us greater confidence in our calculations. We can also observe that the thickness of the plate is ten times smaller than the radius of the plate. This ratio meets the assumptions of the thin plate theory and should give us more accurate results according to both sources [30] and [31]. Finally, we can calculate the factors of safety for the proposed solution.

$$FOS_{Y_{face}} = \frac{\sigma_y}{\sigma_{max} \cdot sf_f} = \frac{739}{366 \cdot 2} = 1,01 \quad (3.49)$$

$$FOS_{U_{face}} = \frac{\sigma_{ult}}{\sigma_{max} \cdot sf_f} = \frac{924}{366 \cdot 2} = 1,26 \quad (3.50)$$

The safety factor for the injector face  $sf_f$  was taken as 2, which is the default value set by the competition rules. As we can see from Equations (3.49) and (3.50), the yield factor of safety is approximately equal to 1 and the ultimate factor of safety is 1,26. These results meet the competition requirements. Full derivation of equations in this chapter used for the creation of Graph 3.3 can be seen in Appendix A.

### 3.2.5 Injector head stress calculations

To calculate the required thickness of the injector head, we will approximate the part as a thin circular plate, with a hole in the middle and simply supported edges. For calculations we will use the theory and equations introduced in sources [30] and [31]. This part will experience loading caused by fuel pressure stressing the part from the bottom. A simplified schematic used for our case can be seen in *Figure 3.10*.

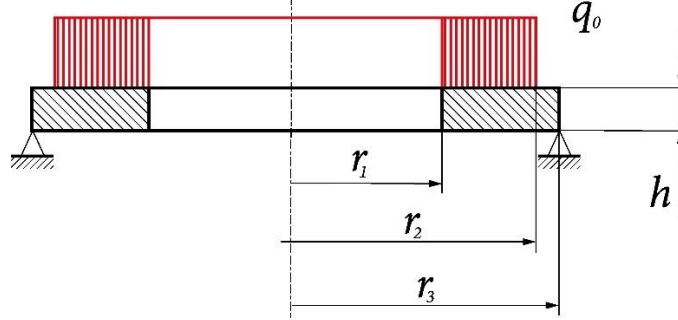


Figure 3.10 Injector head calculation schematic [2]

Since the pressure loading does not go past the outer manifold radius  $r_2$ , we will divide the calculation into two sections. The first section will be described on an interval seen in Equation (3.51).

$$x_I \in \langle r_1; r_2 \rangle \quad (3.51)$$

The second section of the plate will be described on an interval shown in Equation (3.52).

$$x_{II} \in \langle r_2; r_3 \rangle \quad (3.52)$$

The boundary conditions for this calculation will be as follows. The radial stress on the inner diameter of the plate  $\sigma_r^I(r_1)$  will be equal to zero. Since the plate is simply supported, the radial stress on the outer diameter will be also equal to zero  $\sigma_r^{II}(r_3)$ . To ensure continuity of the plate, the radial stress for the first section  $\sigma_r^I(r_2)$  has to be equal to the radial stress for the second section  $\sigma_r^{II}(r_2)$  on the common radius  $r_2$ . The bending angle of the plate for the first section  $\varphi_I(r_2)$  must be also equal to the bending angle of the plate for the second section  $\varphi_{II}(r_2)$  on the common radius  $r_2$ . All boundary conditions can be seen written as mathematical formulas in Equations (3.53) thru (3.56).

$$\sigma_r^I(r_1) = 0 \quad (3.53)$$

$$\varphi_I(r_2) = \varphi_{II}(r_2) \quad (3.54)$$

$$\sigma_r^I(r_2) = \sigma_r^{II}(r_2) \quad (3.55)$$

$$\sigma_r^{II}(r_3) = 0 \quad (3.56)$$

In solution for both sections, we will be using the differential Equation (3.38) for loaded thin circular plates introduced in Chapter 3.2.4.



The derivation of general solution for bending angle of the first section of the plate is similar to the one shown in Chapter 3.2.4. The final expression can be seen in Equation (3.57). It is important to note, the difference between the solution from Chapter 3.2.4 and the one shown in Equation (3.57). The solutions will have different constants that will be derived from boundary conditions and parameters of the plate.

$$\varphi_I(x) = -\frac{B_I \cdot x^3}{8} + C \cdot \left( \frac{x \cdot \ln(x)}{2} - \frac{x}{4} \right) + \frac{C_1 \cdot x}{2} + \frac{C_2}{x} \quad (3.57)$$

By derivation of Equation (3.57), we obtain Equation (3.58) which describes the rate of angle change in the first section of the plate.

$$\varphi_I'(x) = -\frac{3 \cdot B_I \cdot x^2}{8} + C \cdot \left( \frac{\ln(x)}{2} + \frac{1}{4} \right) + \frac{C_1}{2} - \frac{C_2}{x^2} \quad (3.58)$$

For the second section, loading is going to be a constant. Loading per unit length is calculated in Equation (3.59). Continuous loading  $q_0$  will be once again equal to fuel MEOP of the highest possible pressure drop  $p_{Fmax}$  which was determined in Chapter 3.1.2.

$$t(x) = \frac{Q(x)}{2 \cdot \pi \cdot x} = \frac{q_0 \cdot \pi \cdot (r_2^2 - r_1^2)}{2 \cdot \pi \cdot x} = \frac{q_0 \cdot (r_2^2 - r_1^2)}{2 \cdot x} \quad (3.59)$$

Knowing the loading per unit length, we can substitute Equation (3.40) for flexural rigidity and Equation (3.59) for loading per unit length into general Equation (3.38) and obtain an Equation (3.60) for our case.

$$\left[ \frac{1}{x} \cdot (\varphi_{II}(x) \cdot x)' \right]' = -\frac{12 \cdot q_0 \cdot (r_2^2 - r_1^2)}{2 \cdot x \cdot E^* \cdot h^3} \quad (3.60)$$

To simplify the calculation, we will make substitution shown in Equation (3.61).

$$B_{II} = \frac{6 \cdot q_0 \cdot (r_2^2 - r_1^2)}{E^* \cdot h^3} \quad (3.61)$$

Implementing the substitution to we receive a differential Equation (3.62).

$$\left[ \frac{1}{x} \cdot (\varphi_{II}(x) \cdot x)' \right]' = -\frac{B_{II}}{x} \quad (3.62)$$

General solution will be obtained by integration. The final expression for bending angle of the second section of the plate can be seen in Equation (3.63).

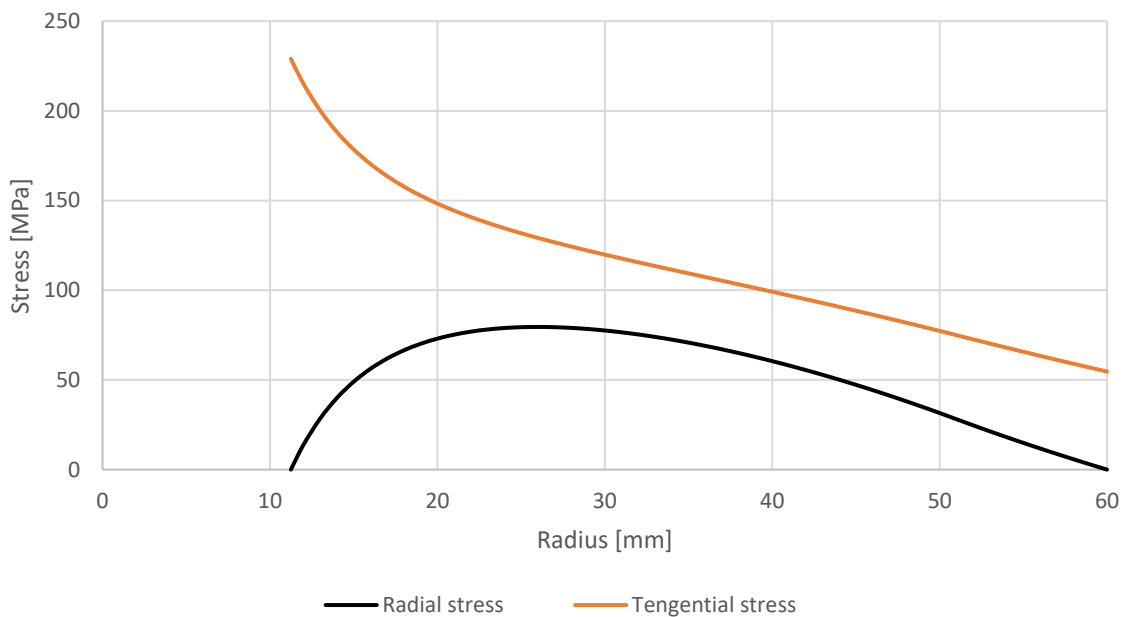
$$\varphi_{II}(x) = -B_{II} \cdot \left( \frac{x \cdot \ln(x)}{2} - \frac{x}{4} \right) + \frac{C_3 \cdot x}{2} + \frac{C_4}{x} \quad (3.63)$$

By derivation, we obtain Equation (3.64) which describes the rate of angle change in the second section of the plate.

$$\varphi_{II}'(x) = -B_{II} \cdot \left( \frac{\ln(x)}{2} + \frac{1}{4} \right) + \frac{C_3}{2} - \frac{C_4}{x^2} \quad (3.64)$$

Finally, we can take the boundary conditions from Equations (3.53) thru (3.56), Equations (3.57) and (3.63) for bending angle in both sections of the plate, Equations (3.58) and (3.64) for rate of angle change in both sections of the plate and Equation (3.47) for radial stress, put them together and calculate constants  $C_1$ ,  $C_2$ ,  $C_3$  and  $C_4$ . Doing so will give us the exact solution for our case, which can be once again put to Equations (3.47) and (3.48).

To obtain the stress distribution, we will input the parameters of the plate. The inner radius  $r_1$  will be taken from the CAD model of the injector assembly and will be directly related to dimensions of the pintle. The final value of this parameter will be equal to 11,25 mm. The outer radius of the manifold  $r_2$  was also taken from the final CAD model. This variable is directly tied to chamber dimensions and will be equal to 51 mm. The outer radius of the plate  $r_3$  was once again taken from the CAD model and was set as the radius of the bolts, which is equal to 60 mm. Plate thickness was iterated until desired properties of the plate were reached. The final thickness was 13 mm. By substituting this plate geometry along with the properties from Table 3.3 for our chosen material to equations derived in this chapter, we can plot Graph 3.4.



Graph 3.4 Injector head stress distribution

Graph 3.4 shows stress distribution in the plate for our case. As we can see, the most critical loading will be on the inner edge of the plate. We can deduce the largest magnitude of stress from the graph.

$$\sigma_{max} = 229 \text{ MPa}$$

The calculation can be compared to results for a similar case obtained by using calculation software MITcalc. The critical value given by this software can be seen below.

$$\sigma_{max} = 285 \text{ MPa.}$$

As we can see, our results are in the same range as the results from MITcalc software. This result can give us a certain confidence in our analytical calculations. The small difference in the results is caused by the inability of the MITcalc software to process multiple sections for the same case. This meant, that the MITcalc calculation was done for slightly different inputs. We can also observe that the thickness of the plate is approximately five times smaller than the radius of the plate. This ratio is right on the edge of the assumptions of the thin plate theory introduced in sources [30] and [31]. This increases the level of inaccuracy in our results. That is why we will rely more heavily on the results given by FEM analysis. We will introduce features such as ribs and iterate the design. We can still calculate the factors of safety for the proposed solution.

$$FOSY_{head} = \frac{\sigma_y}{\sigma_{max} \cdot sf_h} = \frac{503}{229 \cdot 2,15} = 1,02 \quad (3.65)$$

$$FOSU_{head} = \frac{\sigma_{ult}}{\sigma_{max} \cdot sf_h} = \frac{572}{229 \cdot 2,15} = 1,16 \quad (3.66)$$

The safety factor for the injector head  $sf_h$  was increased to 2,15, this was done due to uncertainties introduced in Chapter 3.2.1. As we can see from Equations (3.65) and (3.66), the yield factor of safety is approximately equal to 1 and the ultimate factor of safety is 1,16. These results meet the competition requirements. Full derivation of equations used for the creation of *Graph 3.4* can be seen in Appendix B.

### 3.2.6 Bolt connection stress calculation

The last part of the injector that has been identified as critical is the bolt connection which connects the injector face, injector body and the thrust chamber of the engine. Calculation of this connection will be done in accordance with the ECSS-E-HB-32-23A. Nomenclature in this chapter was taken from the same source and may differ from the rest of the thesis. [29]

First step in the calculation is going to be identifying the force acting upon the connection. The largest loading is going to be caused by the fuel in the manifold. We will use Equation (3.67) to calculate the magnitude of loading.  $d_m$  is the maximum manifold diameter and will be taken from the 3D model.  $d_{p,max}$  is the large pintle diameter and will be also taken from the 3D model.

$$F_{B,c} = p_F \cdot \frac{\pi \cdot (d_m^2 - d_{p,max}^2)}{4} = 5,1 \cdot \frac{\pi \cdot (102^2 - 22,5^2)}{4} = 39\,645,8\,N \quad (3.67)$$

This force will be distributed to the individual bolts. Loading of each bolt will be dependent on the number of bolts used. We can calculate the bolt loading in Equation (3.68).

$$F_B = \frac{F_B}{N_B} \quad (3.68)$$

We have to design the connection to withstand twice the actual force that is why, we will put the safety factor  $sf_b$  equal to 2. We can calculate the required residual prestressing of the joint by using Equation (3.69)

$$Q_0 = F_B \cdot sf_b \quad (3.69)$$

A selection has been made from the configurations shown in Table 3.4.

	Weight	$F_B$	$Q_0$
	[g]	[N]	[N]
18x M8	222	2202,5	4405
16x M8	197	2478	4956
12x M8	148	3304	6608
18x M6	108	2202,5	4405
16x M6	96	2478	4956
12x M6	72	3304	6608

Table 3.4 Bolt connection configurations

The selected configuration was 18x M6, 10.9 bolts. The selection was done using weight of the configuration and strength checks performed using MITcalc software. The chosen bolts will be screwed to the combustion chamber flange. We will be thus conducting our calculations for bolt connection with a bolt stud. Loading is going to be considered axial and static. The calculation will not take into account thermal induced loads. Equations were modified to exclude thermal loading. Calculations will be only performed for the chosen configuration. The calculation may be updated in the future if the hot fire testing shows, that the thermal loading of the bolts has significance.

Fastener parameters				
Parameter	Nomenclature	Calculation	Value	Units
Nominal diameter	$d$	-	6	mm
Thread pitch	$p$	-	1	mm
Pitch diameter	$d_2$	-	5,35	mm
Minor diameter	$d_3$	-	4,773	mm
Stress diameter	$d_s$	-	5,062	mm
Bolt head diameter	$D_h$	-	10	mm
Hole diameter	$D$	-	6,4	mm
Mean bearing radius	$d_{uh}$	$0,5 \cdot (D_h + D)$	8,2	mm
Thread angle	$\alpha$	-	60	deg
Minor area	$A_3$	$\frac{\pi \cdot d_3^2}{4}$	17,893	mm <sup>2</sup>
Stress area	$A_s$	$\frac{\pi \cdot d_s^2}{4}$	20,121	mm <sup>2</sup>
Nominal area	$A_{nom}$	$\frac{\pi \cdot d^2}{4}$	28,274	mm <sup>2</sup>
Helix angle	$\varphi$	$\arctan\left(\frac{p}{\pi \cdot d_2}\right)$	3,4°	deg

Figure 3.11 Bolt parameters

Value of 0,5 is going to be chosen for preload ratio  $\gamma$ . For the chosen bolt class and size, preload force is calculated in Equation (3.70).

$$F_V = \gamma \cdot \sigma_y \cdot A_s = 0,5 \cdot 900 \cdot 20,121 = 9054,4 \text{ N} \quad (3.70)$$

Preload loss due to embedding is assumed to be 5% of the maximum preload. We can calculate the value in Equation (3.71).

$$F_z = 0,05 \cdot F_V = 0,05 \cdot 9054,4 = 452,7 \text{ N} \quad (3.71)$$

The coefficient of friction of the thread interface  $\mu_{th}$  was chosen as 0,16. This value was advised by a more experienced colleague. Local friction angle can be calculated in Equation (3.72).

$$\rho = \arctan\left(\frac{\mu_{th}}{\cos\left(\frac{\alpha}{2}\right)}\right) = \arctan\left(\frac{0,16}{0,866}\right) = 10,468^\circ \quad (3.72)$$

Torque present at the thread interface is given by Equation (3.73). We can input the parameters and calculate the value of the torque in Equation (3.74).

$$M_{th} = F_V \cdot \frac{d_2}{2} \cdot \tan(\varphi + \rho) \quad (3.73)$$

$$M_{th} = 9054,4 \cdot \frac{5,35 \cdot 10^{-3}}{2} \cdot \tan(3,405 + 10,468) = 5,981 \text{ Nm} \quad (3.74)$$

Under head torque between the clamped part and fastener can be calculated from Equation (3.75). Value of coefficient of friction between the bolt head and the clamped part  $\mu_{uh}$  was set to 0,14. This value was advised by a more experienced colleague.

$$M_{uh} = F_V \cdot \frac{\mu_{uh} \cdot d_{uh}}{2 \cdot \sin\left(\frac{\lambda}{2}\right)} = 9054,4 \cdot \frac{0,14 \cdot 8,2 \cdot 10^{-3}}{2 \cdot \sin\left(\frac{180}{2}\right)} = 5,197 \text{ Nm} \quad (3.75)$$

Now we can find out the total torque applied can be calculated as a sum of the individual torques.  $M_p$  in Equation (3.76) is the prevailing torque. The value was taken from source [29].

$$M_{app} = M_{th} + M_{uh} + M_p = 5,981 + 5,197 + 0,2 = 11,38 \text{ Nm} \quad (3.76)$$

The maximum and minimum bounds of the applied torque are calculated in Equations (3.77) and (3.78).  $\omega$  is the torque wrench accuracy. The value will be taken  $\pm 6\%$ . This value was suggested by a team report. [2]

$$M_{app,max} = (1 + \omega) \cdot M_{app,nom} = (1 + 0,06) \cdot 11,38 = 12,06 \text{ Nm} \quad (3.77)$$

$$M_{app,min} = (1 - \omega) \cdot M_{app,nom} = (1 - 0,06) \cdot 11,38 = 10,70 \text{ Nm} \quad (3.78)$$

Maximum in-service preload can be calculated from Equation (3.79). Uncertainty factors for torque measured lubricated bolts  $\varepsilon$  were taken from source [29] as  $\pm 25\%$ . Value of coefficient of friction were once again taken from a more experienced colleague.

$$F_{V,max} = \frac{(1 + \varepsilon) \cdot M_{app,max} - M_{p,min}}{\frac{d_2}{2} \cdot \left( \tan(\varphi) + \frac{\mu_{th,min}}{\cos\left(\frac{\alpha}{2}\right)} \right) + \frac{d_{uh}}{2} \cdot \mu_{uh,min}} \quad (3.79)$$

$$F_{V,max} = \frac{(1 + 0,25) \cdot 12,06 - 0,2}{\frac{5,35 \cdot 10^{-3}}{2} \cdot \left( 0,0595 + \frac{0,14}{0,866} \right) + \frac{8,2 \cdot 10^{-3}}{2} \cdot 0,12} = 13\,729,7\,N \quad (3.80)$$

Similarly to maximum in-service preload, we will calculate the minimum in-service preload from Equation (3.81).

$$F_{V,min} = \frac{(1 - \varepsilon) \cdot M_{app,min} - M_{p,max}}{\frac{d_2}{2} \cdot \left( \tan(\varphi) + \frac{\mu_{th,max}}{\cos\left(\frac{\alpha}{2}\right)} \right) + \frac{d_{uh}}{2} \cdot \mu_{uh,max}} - F_Z \quad (3.81)$$

$$F_{V,min} = \frac{(1 - 0,25) \cdot 10,70 - 1,2}{\frac{5,35 \cdot 10^{-3}}{2} \cdot \left( 0,0595 + \frac{0,18}{0,866} \right) + \frac{8,2 \cdot 10^{-3}}{2} \cdot 0,16} - 452,7 = 4\,741,7\,N \quad (3.82)$$

As we can see from the results, the minimum in-service preload is higher than the required prestressing. This is a necessary condition for applicability of the chosen solution.

Now, we will calculate the maximum stress in the bolt from pretension. We will start by calculating polar section modulus from Equation (3.83).

$$W_p = \frac{\pi \cdot d_3^3}{16} = \frac{\pi \cdot (4,773 \cdot 10^{-3})^3}{16} = 2,1325 \cdot 10^{-8} m^3 \quad (3.83)$$

Minimum moment absorbed by friction under the fastener head is given by Equation (3.84).

$$M_{uh,min} = \frac{d_{uh}}{2} \cdot F_{V,max} \cdot \mu_{uh,min} = \frac{8,2 \cdot 10^{-3}}{2} \cdot 13\,729,7 \cdot 0,12 = 6,75\,Nm \quad (3.84)$$

Maximum shear stress due to torsion can be then calculated from Equation (3.85).

$$\tau_{max} = \frac{M_{app,max} - M_{uh,min}}{W_p} = \frac{12,06 - 6,75}{2,1325 \cdot 10^{-8}} = 248,6 \cdot 10^6\,Pa = 248,6\,MPa \quad (3.85)$$

Maximum pretension stress is given by Equation (3.86).

$$\sigma_{V,max} = \frac{F_{V,max}}{A_s} = \frac{13\,729,7}{20,121} = 682,4\,MPa \quad (3.86)$$

Von Mises equivalent stress can be obtained from Equation (3.87).

$$\sigma_{v.m.} = \sqrt{\sigma_{V,max}^2 + 3 \cdot \tau_{max}^2} = \sqrt{682,4^2 + 3 \cdot 248,6^2} = 807 \text{ MPa} \quad (3.87)$$

Factors of safety for tightening can be calculated from Equations (3.88) and (3.89).

$$FOSY_{ti} = \frac{\sigma_{ult}}{\sigma_{v.m.}} = \frac{900}{807} = 1,11 \quad (3.88)$$

$$FOSU_{ti} = \frac{\sigma_{ult}}{\sigma_{v.m.}} = \frac{1000}{807} = 1,24 \quad (3.89)$$

As we can see from the results, both factors of safety are above one. Ideally, we would want the yield factor of safety to be at least 1,2. However, the proposed solution meets the operation requirements. Especially considering that the results from our MITcalc calculations support these results.

Next, we also want to calculate the factors of safety for thread failure under axis loads. To do that, we will first calculate substitution lengths for deformations. The values in Equations (3.90) thru (3.92) were suggested by source [29].

$$L_{h,sub} = 0,5 \cdot d = 0,5 \cdot 6 = 3 \text{ mm} \quad (3.90)$$

$$L_{eng,sub} = 0,33 \cdot d = 0,33 \cdot 6 = 1,98 \text{ mm} \quad (3.91)$$

$$L_{n,sub} = 0,4 \cdot d = 0,4 \cdot 6 = 2,4 \text{ mm} \quad (3.92)$$

Fasteners compliance can be calculated from Equation (3.93). We will assume that all the parts have to same Young's module. The value of Young's module was taken from the MITcalc library.

$$\delta_b = \frac{1}{E_b} \cdot \left[ \frac{L_{h,sub}}{A_{nom}} + \frac{L_{eng,sub}}{A_3} + \frac{L_{n,sub}}{A_{nom}} + \frac{L_b}{A_3} \right] \quad (3.93)$$

$$\delta_b = \frac{1}{211000} \cdot \left[ \frac{3}{28,274} + \frac{1,98}{17,893} + \frac{2,4}{28,274} + \frac{12}{17,893} \right] = 4,6 \cdot 10^{-6} \text{ mm/N} \quad (3.94)$$

We will use Equation (3.95) to calculate compliance of the clamped parts. The equation differs from the ECSS standard but is generally used for this purpose.

$$\delta_c = \frac{4 \cdot l_f}{\pi \cdot E_f \cdot (D_h^2 - D^2)} + \frac{4 \cdot l_h}{\pi \cdot E_h \cdot (D_h^2 - D^2)} \quad (3.95)$$

$$\delta_c = \frac{4 \cdot 4}{\pi \cdot 210000 \cdot (10^2 - 6,4^2)} + \frac{4 \cdot 8}{\pi \cdot 71700 \cdot (10^2 - 6,4^2)} = 2,8 \cdot 10^{-6} \text{ mm/N} \quad (3.96)$$

Force ratio can be calculated from Equation (3.97). A loading plane factor  $n$  was suggested by a more experienced colleague. Force ratio with loading plane adjustment can be calculated in Equation (3.98).

$$\Phi = \frac{\delta_c}{\delta_c + \delta_b} = \frac{2,8 \cdot 10^{-6}}{2,8 \cdot 10^{-6} + 4,6 \cdot 10^{-6}} = 0,379 \quad (3.97)$$

$$\Phi_n = n \cdot \Phi = 0,75 \cdot 0,379 = 0,285 \quad (3.98)$$

Factors of safety for thread failure under axis loads can be calculated from Equations (3.99) and (3.100).

$$FOSY_{LOAD} = \frac{A_s \cdot \sigma_y}{F_{V,max} + \Phi_n \cdot F_B \cdot sf_b} = \frac{20,121 \cdot 900}{13\,729,7 + 0,285 \cdot 2202,5 \cdot 2} = 1,21 \quad (3.99)$$

$$FOSU_{LOAD} = \frac{A_s \cdot \sigma_{ult}}{F_{V,max} + \Phi_n \cdot F_B \cdot sf_b} = \frac{20,121 \cdot 1000}{13\,729,7 + 0,285 \cdot 2202,5 \cdot 2} = 1,35 \quad (3.100)$$

These factors of safety are acceptable. MITcalc calculation gave a  $FOSY_{LOAD}$  equal to 1,37.

Lastly, we want to check the the factors of safety for crushing of flanges. Maximum compressive stress can be calculated by Equation (3.101).

$$\sigma_{uh,max} = \frac{F_{V,max}}{S_{uh}} = \frac{F_{V,max}}{\frac{\pi \cdot (D_h^2 - D^2)}{4}} = \frac{13\,729,7}{\frac{\pi \cdot (10^2 - 6,4^2)}{4}} = 296 \text{ MPa} \quad (3.101)$$

Subsequent margins of safety can be calculated by Equations (3.102) and (3.103). The values of maximum allowable flange stresses for aluminium were taken from the source [29].

$$FOSY_{CR} = \frac{\sigma_{br,y}}{\sigma_{uh,max} \cdot sf_b} = \frac{593}{296 \cdot 2} = 1 \quad (3.102)$$

$$FOSU_{CR} = \frac{\sigma_{br,ult}}{\sigma_{uh,max} \cdot sf_b} = \frac{689}{296 \cdot 2} = 1,16 \quad (3.103)$$

We can see from the performed calculations, that the compressive stresses are within safety limits and rule requirements. This calculation will cover an anomaly seen in Chapter 5.1.2, where stress around fastener holes is elevated to significant levels.



## 4 CAD model

A 3D model was created in Autodesk Fusion. The model was based on work performed in Chapter 3 and went through many iterations.

Creation of the pintle started from the dimension of the tip. A taper was then created to allow for injection area control. Thread was chosen with the smallest possible pitch for pintle control. Sealing spots were identified. Based on size constrains-seal grooves were made and seals selected. Viton O-rings were chosen due to their compatibility with Ethanol and temperature resistance [32]. Port was created that allowed for installation of a pressure transducer for fuel manifold measurements. Ribs were created to reinforce the injector head.

*Figure 4.1* shows the final 3d model of the injector without the fasteners, seals and pressure transducer.

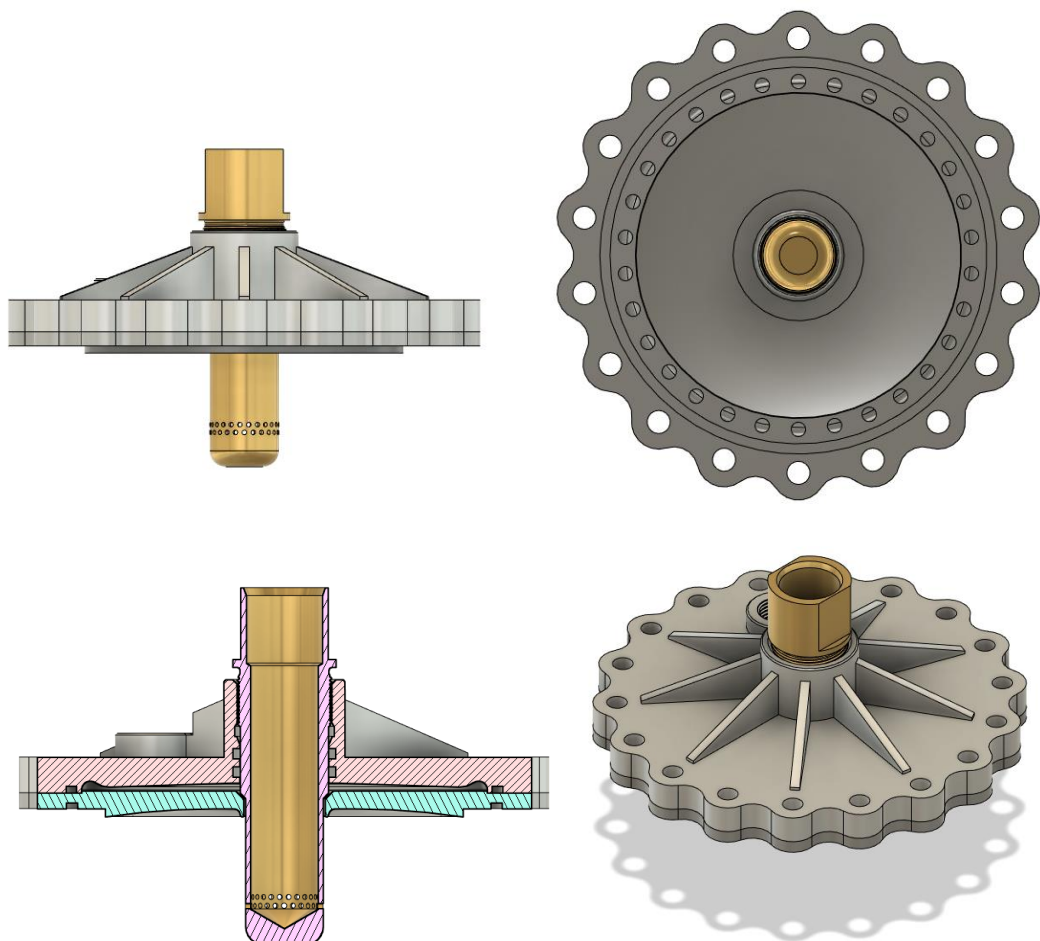


Figure 4.1 Injector 3D model

## 5 Design verification

We will create numerical simulations to verify the final design of the injector. These simulations will give us an idea of the assembly properties. The simulations will be updated and adjusted based on the real-world data obtained from testing campaign which has been proposed in Chapter 6.

### 5.1 FEM analysis

We will use finite element method to enhance our analytical tools. The analytical calculations were conducted for simplified cases and did not take into account certain design details of the parts. Software used will be Autodesk Fusion Simulation Extension. Specifically, we will use simple static stress simulation for both cases.

#### 5.1.1 Pintle analysis

Firstly, we will analyse the 3D model of the pintle. Unlike in our simplified calculations in Chapter 3.2.2 the actual pintle will feature a set of radial holes near the tip. These holes can cause potentially dangerous stress concentration and warrant further investigation. A standard linear static analysis is going to be used to analyse the expected loading case. Material properties of brass in the simulation were taken from the fusion library. For the final iteration a mesh that consisted of approximately 2,6 million tetrahedral elements was created. Pressure loading of 4 MPa was applied to the entire inside area of the pintle. This value was taken from the analysis results in Chapter 5.2.1 The top of the pintle was constrained in all directions. This constrain was used to anchor the part in space and did not influence the outcome of the simulation. The meshed part can be seen in *Figure 5.1*.



Figure 5.1 Pintle FEM analysis mesh

Since the radial holes were identified as critical part of the pintle, element size around them was decreased to 0,25 mm. Detail of the mesh around these holes can be seen in *Figure 5.2*. Computational power could be saved by utilizing symmetry. This option was not chosen due to the fact, that the current simulation took a reasonable amount of time.

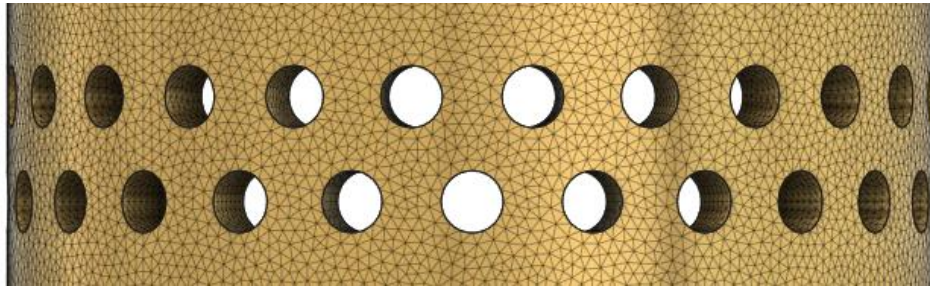


Figure 5.2 Detail of the mesh around radial holes

We can see the overall results of our analysis in *Figure 5.3*. The image shows, that the overall stress in the part is similar to our calculations. It is also visible, that the highest stress concentration will occur near the radial holes.

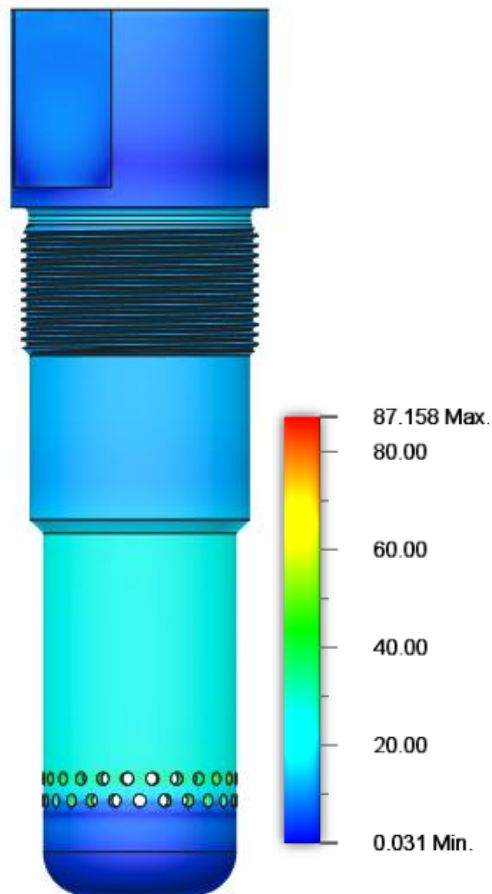


Figure 5.3 Results of pintle FEM analysis

Detailed image of the stress concentration near radial holes can be seen in *Figure 5.4*. The scale was limited from the bottom to only show stress above 30 MPa. This is the approximate value of maximum stress calculated in Chapter 3.2.2. This means that only sections highlighted exceed the assumed maximum stress.

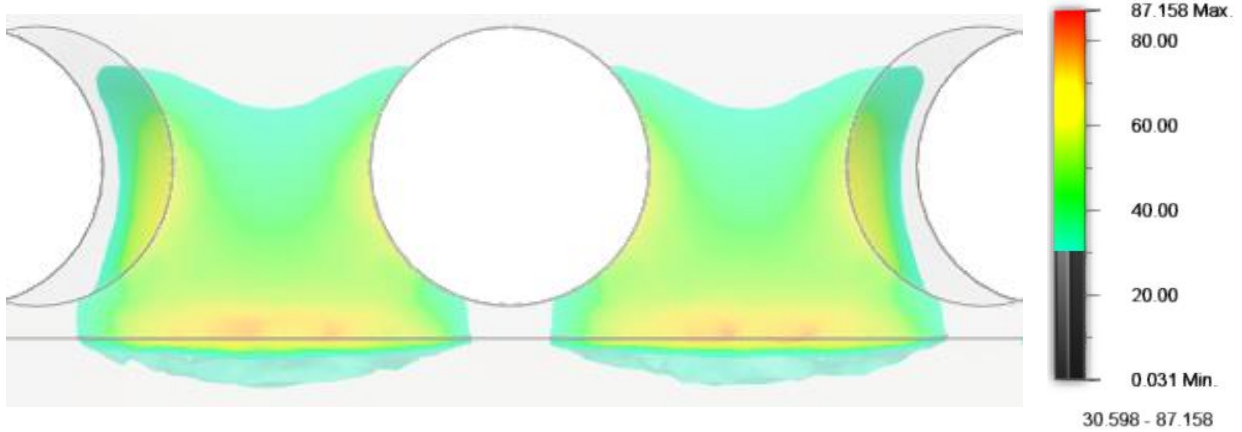


Figure 5.4 Stress concentration near radial holes

We can take the maximum von Mises stress from the analysis and calculate yield and ultimate factors of safety.

$$FOSY_{pintle,FEM} = \frac{\sigma_y}{\sigma_{max} \cdot sf_p} = \frac{230}{87 \cdot 2} = 1,32 \quad (5.1)$$

$$FOSU_{pintle,FEM} = \frac{\sigma_{ult}}{\sigma_{max} \cdot sf_p} = \frac{360}{87 \cdot 2} = 1,84 \quad (5.2)$$

The safety factor for the pintle was taken from Chapter 3.2.2. As we can see in Equations (5.1) and (5.2), both factors of safety are lower compared to the calculations from Chapter 3.2.2. More importantly, they are still larger than one. The FEM analysis thus proves, that the pintle meets the competition and safety requirements.

### 5.1.2 Manifold analysis

In this chapter, we will analyse 3D models of the injector face, injector head and cold flow manifold. Unlike in our simplified calculations in Chapter 3.2 the actual parts feature a number of smaller design features. They also interact with each other. That is why it was decided, to analyse the entire manifold assembly. A standard linear static analysis is going to be used to analyse the expected loading case. Material properties of stainless steel and aluminium in the simulation were taken from the fusion library. For the final iteration a mesh that consisted of approximately 460 thousand tetrahedral elements was created. Pressure loading of 5,1 MPa was applied to the surface of the manifold, that will be in contact with the fuel. The value of pressure loading was taken from calculations in Chapter 3.1.2. Contacts were made between the parts. Contact type used was separation. This contact prescribes, that bodies cannot penetrate each other, but can separate from each other, or slide on one another. Thys contact type needs to have defined coefficients of static friction  $\mu_s$ . These coefficients were set to 0,74 for steel-on-steel contacts and to 0,61 for aluminium-on-steel contacts. These values were taken from source [34].

Figure 5.5 shows a complete mesh of the assembly. The figure also shows connectors used to constrain the parts together. Bolted connectors were used. These connectors simulate the preload from bolts, which were calculated in Chapter 3.2.6. The preload value chosen was maximum in-service preload calculated in Equation (3.80).

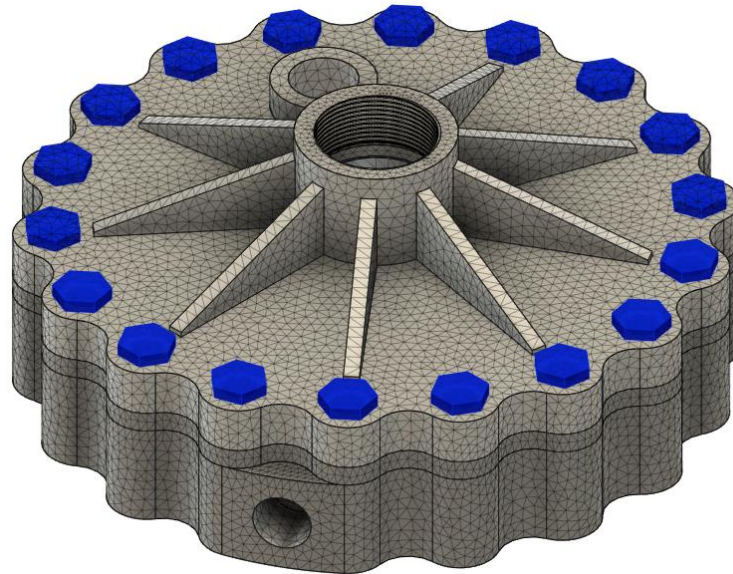


Figure 5.5 Manifold FEM mesh

Figure 5.6 shows the overall stress distribution in the injector face. As we can see, the loading does not reach critical levels. Figure 5.7 shows a detail of the only area in the part, where the simulated stress surpasses the values calculated in Chapter 3.2.4. This stress peak was not deemed critical. The rest of the part experiences lower stress levels compared to our analytical calculations. This is because during the design process, additional reinforcing features of the injector face were created. Factors of safety will not be calculated for this simulation, instead values from Chapter 3.2.4 will be used.

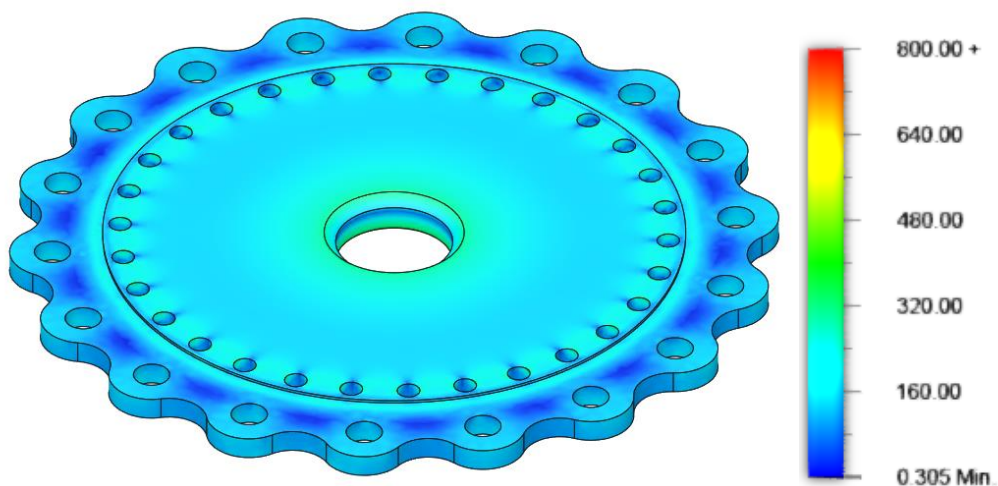


Figure 5.6 Injector face von Mises stress

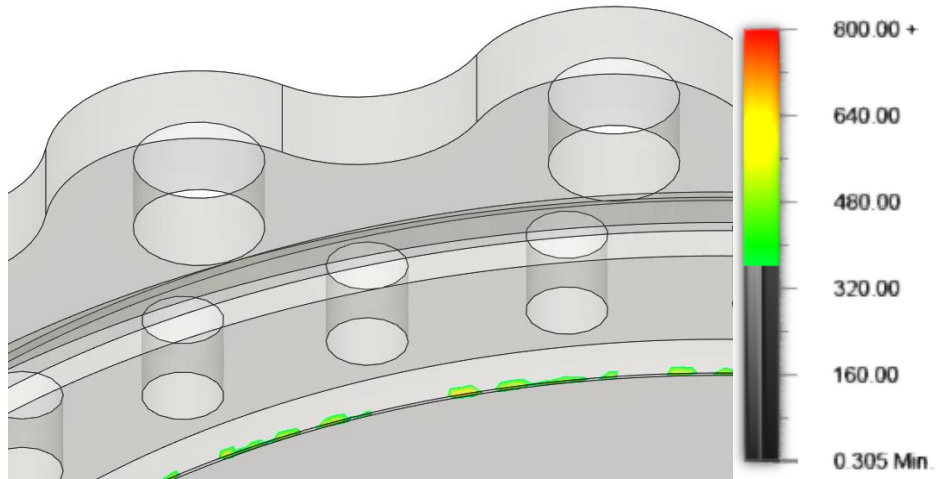


Figure 5.7 Injector face FEM detail

Figure 5.8 shows the contact pressure distribution in the injector head contact. As we can see, the loading does not reach critical limit, which were introduced in Chapter 3.2.6. The actual result for maximum contact pressure in the injector head from the simulation was 126 MPa. This value is lower compared to the maximum compressive stress under the bolt head calculated in Equation (3.101).

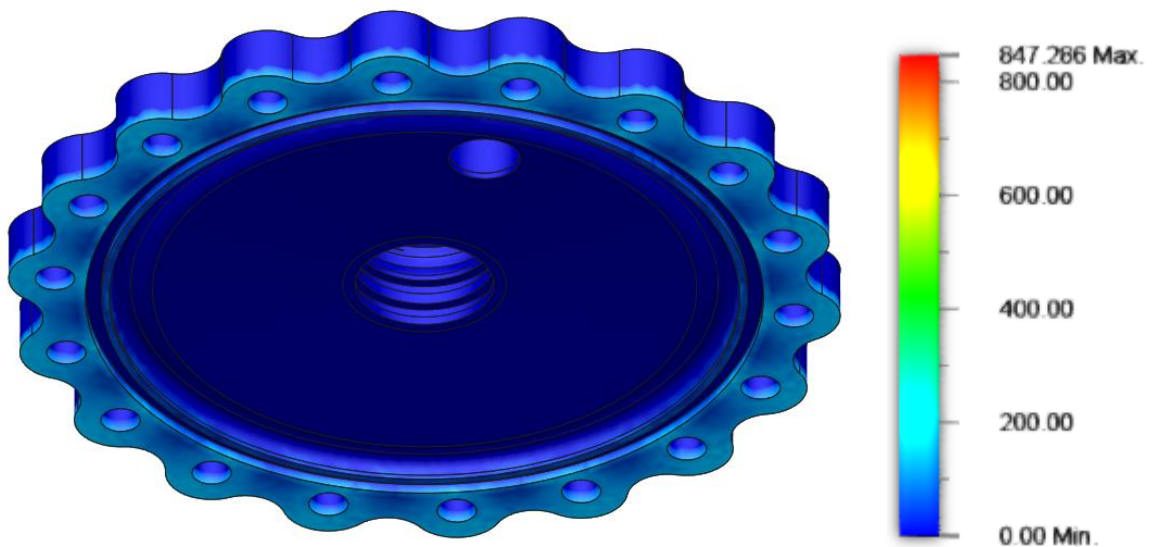


Figure 5.8 Injector head contact pressure

Figure 5.9 shows the stress distribution in the injector head, as we can see, major stress concentration occurs under the bolt heads. Rest of the part is not critically loaded. It is my suspicion, that this is caused by the imperfections in the FEM program used. It would be desirable to conduct a more detailed FEM analysis during future development. Details of the major stress concentration can be seen in Figure 5.10 and Figure 5.11. It has been decided that this concentration will not be critical during real world operations, since the connection was checked using analytical calculations in Chapter 3.2.6. Factors of safety will not be calculated for this simulation, instead values from Chapter 3.2.5 will be used.

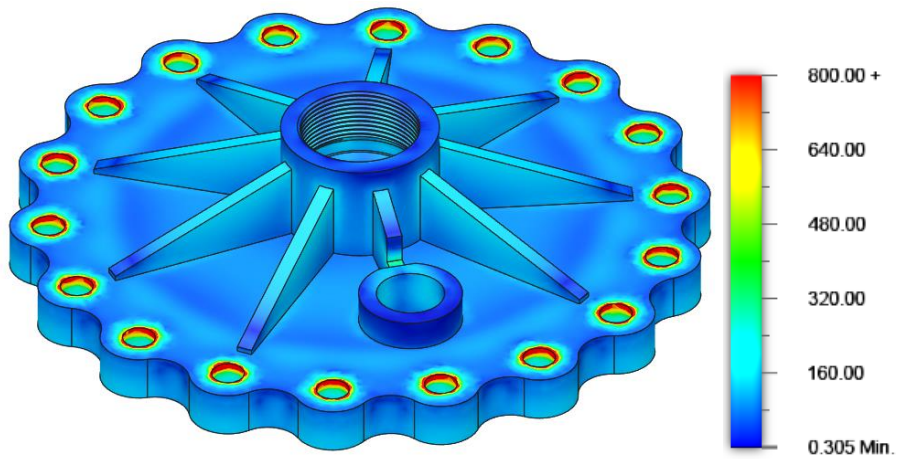


Figure 5.9 Stress distribution in the injector head

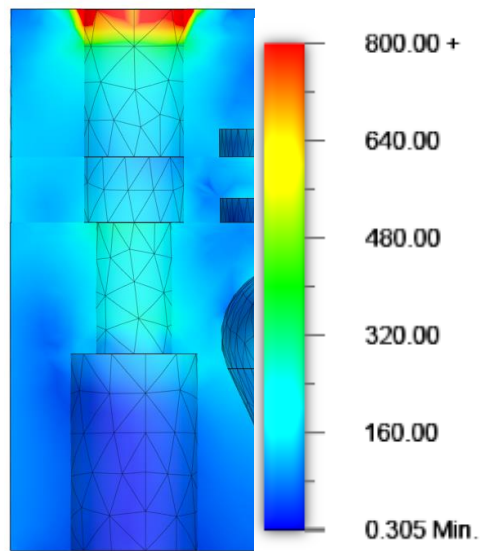


Figure 5.10 Stress distribution along the bolted connection

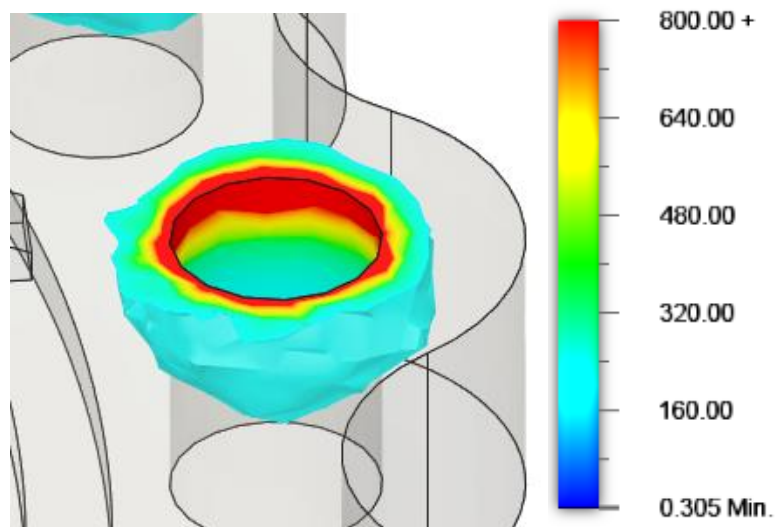


Figure 5.11 Detail of the stress concentration under the bolt head

## 5.2 CFD analysis

To verify our fluid calculations a CFD analysis of the injector assembly is going to be performed. The assembly will be split to two parts. These parts will be analysed separately. Ansys Fluent 2021 R2 will be used to conduct the simulations.

### 5.2.1 Pintle analysis

To analyse the oxidizer pressure drop and injection velocity a simplified model of the pintle tip was created. In this model, two volume regions were generated. One for the oxidizer inside the pintle and the other one for the pintle body. Material properties for the brass body were taken from the Ansys library. Oxidizer properties were also taken from the Ansys library, only density was adjusted to the value used for liquid calculations in Chapter 3.1. SST  $k-\omega$  turbulence model was used. The final mesh composed from 867,5 thousand poly-hexcore and prism cells and can be seen in *Figure 5.12*. The prism cells were used to improve analysis in the boundary layer. Symmetry could have been utilized to reduce computational demands, however the current pintle simulation did not require such measures.



Figure 5.12 Pintle CFD mesh

The size of elements was decreased around the radial holes. This was done to increase resolution of the oxidizer flow through these holes, which is the most important part of the pintle simulation. Detail of the mesh with visible prism cells around the edge of the hole can be seen in *Figure 5.13*.

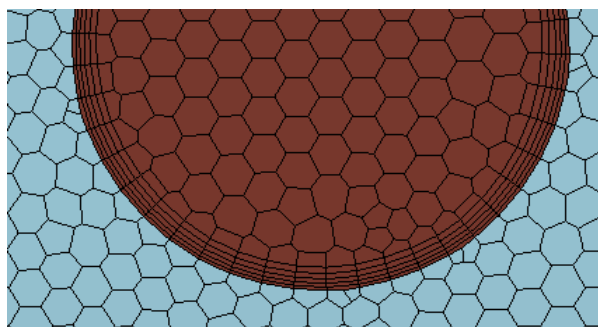


Figure 5.13 Detail of prism cells in radial hole



Another detailed mesh view can be seen in *Figure 5.14*. This figure shows the border between both volumetric regions and the increased density of cells near radial holes.

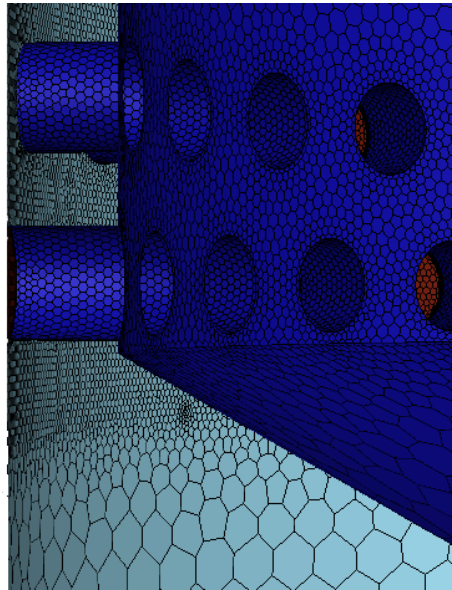


Figure 5.14 Detail of the pintle mesh

The analysis type was set to steady state. Boundary condition for the pintle top was set to mass flow inlet with the mass flow value taken from calculations in Chapter 3.1. The radial holes were setup as pressure outlet with the value of pressure set to  $0 Pa$ . This setup will show the absolute value of oxidizer pressure drop. Both boundary conditions can be seen in *Figure 5.15*.

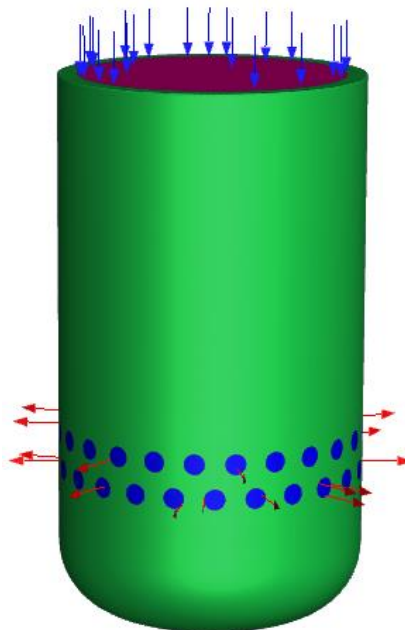


Figure 5.15 Pintle boundary conditions

The result of the simulation can be seen in *Figure 5.16*. The figure shows pressure and velocity profiles on a zoomed in cutout of the pintle. The average oxidizer injection speed given by the simulation was  $37,7 \text{ m/s}$ . This value is higher compared to our results from Chapter 3.1. We can also see that the oxidizer pressure drop is larger than expected. The calculations in Chapter 3.1.1 were done for an oxidizer pressure drop of  $6 \text{ bars}$ . Resulting pressure drop from the simulation is  $10,7 \text{ bars}$ . This difference could have been caused by wrong selection of discharge coefficient in Equation (3.5). It has been decided to keep the current design of the pintle and verify the simulations by cold flow testing the part. If the data collected from this initial cold flow support the results of the simulation, discharge coefficient will be adjusted and injection area of the pintle changed.

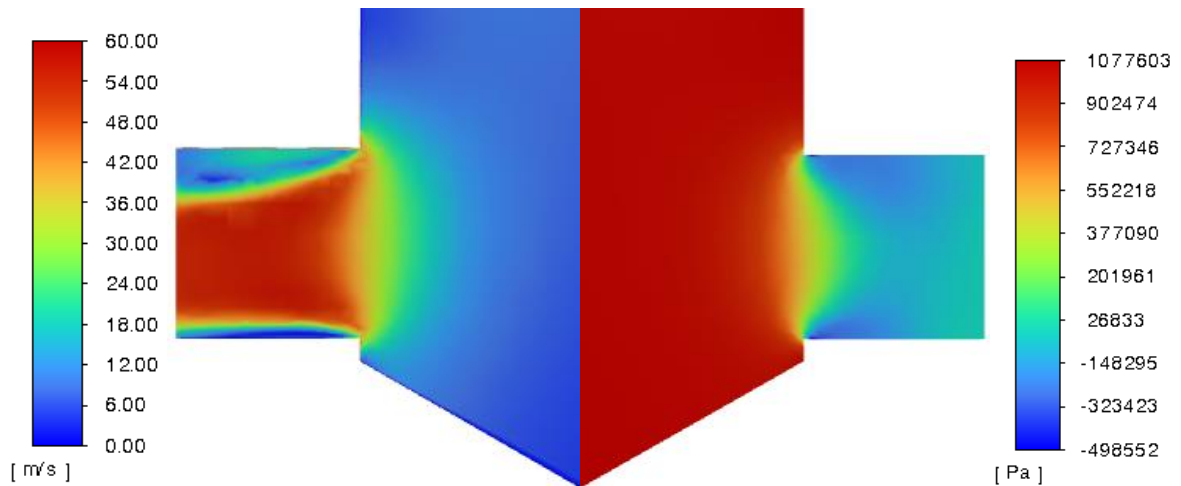


Figure 5.16 Nitrous oxide injection parameters

A second simulation was created for water as an injection medium. This simulation utilized the same model with adjusted properties for the liquid. Properties of water were taken from the Fluent library. This simulation was done as benchmark for cold flow testing. Since the first cold flows will be done with water, comparison to this simulation will be used to verify the simulation and decide the potential change in injection area. *Figure 5.17* shows velocity and pressure profiles on a zoomed in cutout of the pintle. The average injection speed from the radial hole was  $28,6 \text{ m/s}$ . More important is the pressure drop. We will be comparing the pintle pressure measured during a water cold flow to the  $8 \text{ bars}$  from this simulation.

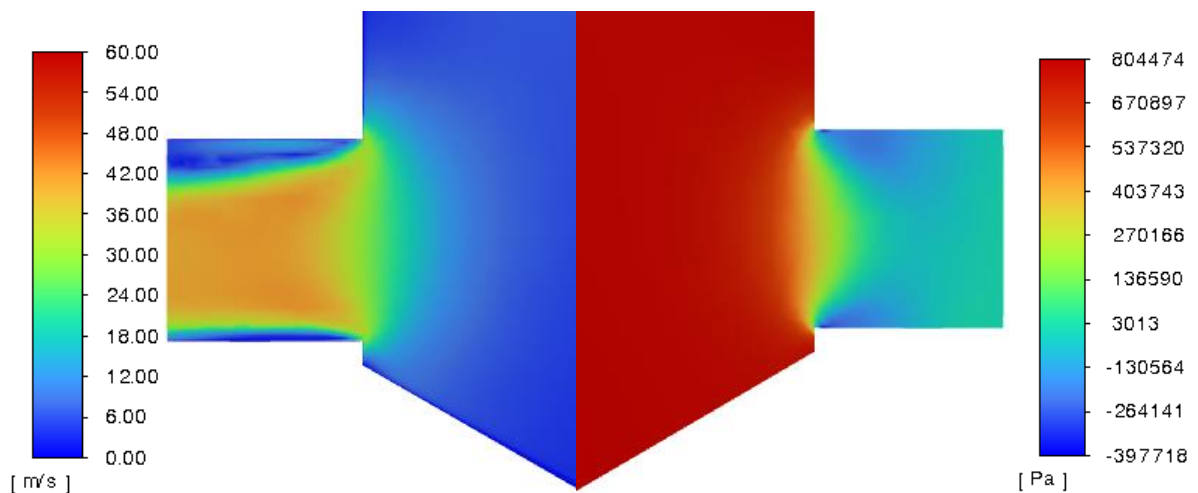


Figure 5.17 Pintle injection parameters for water

Last analysis performed for the pintle was a thermal stress analysis. As we know from our research in Chapter 2.1.4, pintle injectors are prone to heat concentration in the pintle tip, which can lead to overheating of the part. The analysis was conducted on the same mesh as for the earlier pintle simulations.

The analysis type was switched to transient and energy equation was turned on. Initial temperatures of the pintle body and the oxidizer were set to 273 K. The temperature of combustion was set to 2 000 K. This value was taken from NASE CEA which was introduced in Chapter 1.3. The value of heat transfer coefficient was set to  $2879 \text{ W} \cdot \text{m}^{-2} \cdot \text{K}^{-1}$ . This value was taken from team documentation [2] since it was used for chamber cooling analysis. The exact value of this coefficient is an unknown and lowers the confidence in the final results. Material properties were taken from the Ansys library. Time step was set to 0,1 s and the total number of time steps was set to 80. This combination of parameters will let us simulate the longest expected hot fire duration of 8 s. This value was determined in Chapter 1.3. The final result of the simulation can be seen in Figure 5.18.

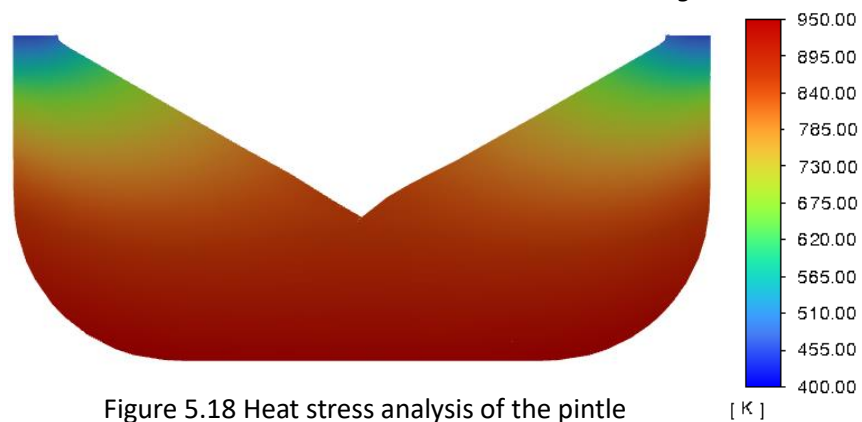
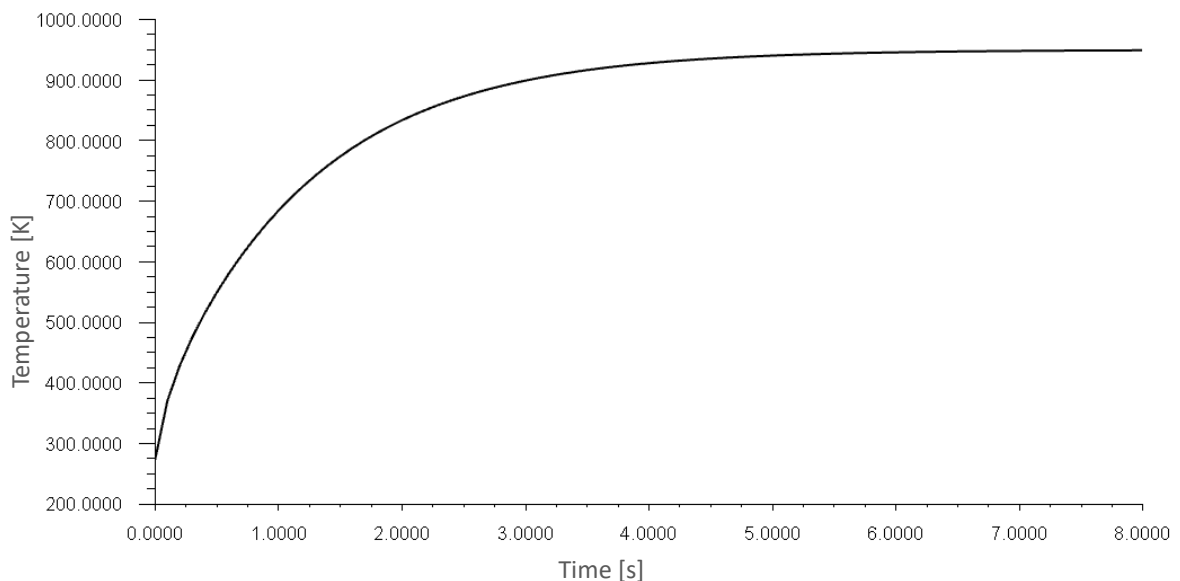


Figure 5.18 Heat stress analysis of the pintle

The maximum temperature reached was 950 K. This temperature is lower than the melting point shown in Table 3.3. However, it is still higher than a comfortable operational temperature range for brass. Graph 5.1 shows the maximum temperature of the pintle in time. As we can see the temperature stabilises after 4 seconds. Based on these results, we could theoretically conduct a shortened hot fire test to test the brass pintle. Final decision on this matter is outside of the scope of this thesis. We can however state that a switch to titanium for the final design is desirable.



Graph 5.1 Pintle tip temperature in time

## 5.2.2 Fuel manifold analysis

To analyse the manifold pressure losses, fuel pressure drop and fuel injection velocity a simplified model of the fuel volume which will be inside the manifold and anulus was created. This model was a 6 degree section cut and heavily utilized symmetry of the part. Shape of the cutout can be seen in *Figure 5.19*.

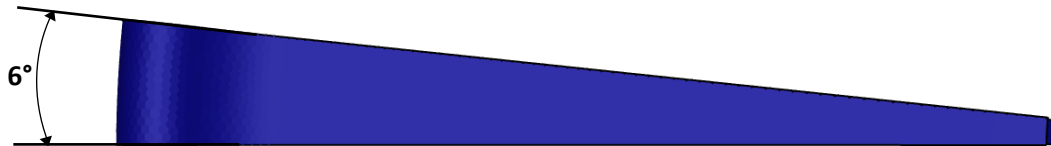


Figure 5.19 Fuel manifold cutout

Same as in the CFD analysis of the pintle, SST  $k-\omega$  turbulence model was used. The final mesh was made up of 36 thousand polyhedral and prism cells. The prism cells were used to improve analysis in the boundary layer. The mesh with a zoomed in cutout can be seen in *Figure 5.20*. The decision to use the symmetry and lower the computational demands of the simulation was made to ease future simulations. It is planned to use this model to simulate the engine startup time mentioned in Chapter 3.1.3. This simulation will have to use a transient analysis type with really small time step and drastically increase the computational demands.

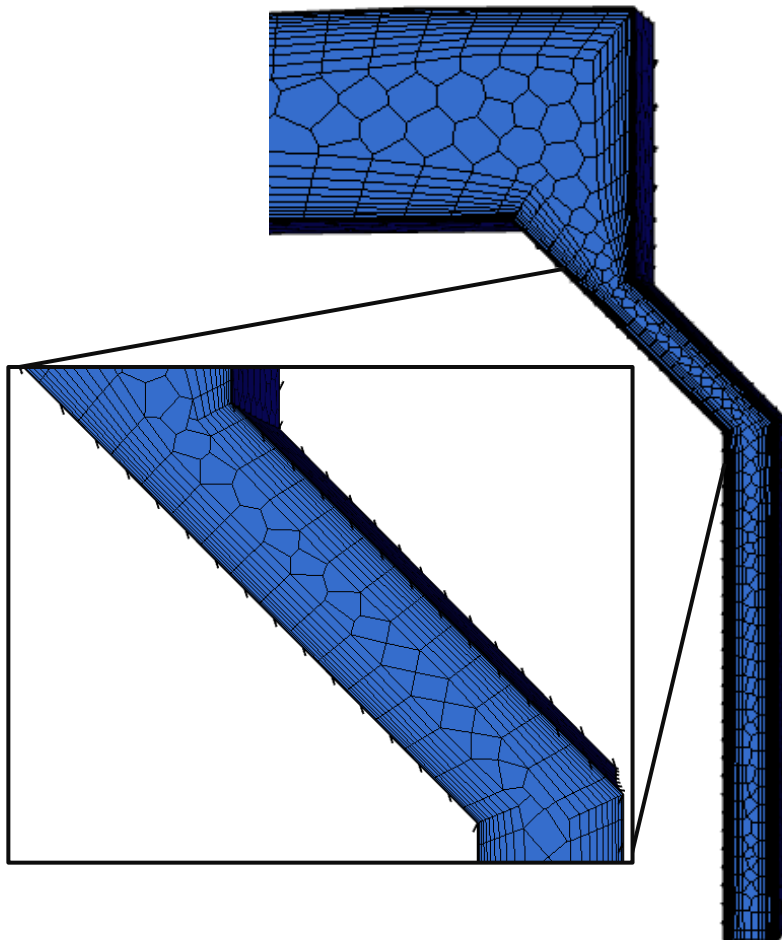


Figure 5.20 Fuel injection mesh

The analysis type was set to steady state. Boundary condition for the manifold were set the following way. The cooling channel fuel inlet was set to mass flow inlet with the mass flow value taken from calculations in Chapter 3.1. Since the CFD model use was a section cut of the actual part. The value of the mass flow had to be adjusted according to Equation (5.3).

$$\dot{m}_{F,CFD} = \frac{\dot{m}_F}{60} = \frac{0,863}{60} = 1,438 \cdot 10^{-2} \text{ kg/s} \quad (5.3)$$

The radial holes were setup as pressure outlet with the value of pressure set to 0 Pa. This setup will show the absolute value of fuel pressure drop. Both boundary conditions can be seen in Figure 5.21.

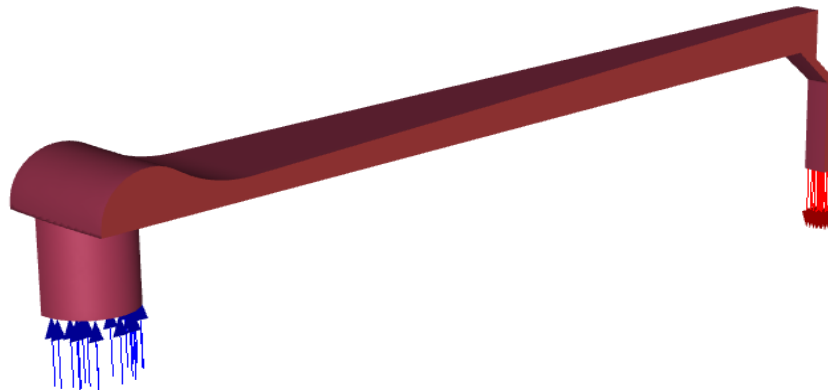


Figure 5.21 Manifold boundary conditions

The result of the simulation can be seen in Figure 5.22. The figure shows pressure and velocity profiles on a zoomed in cutout of the annulus. The average fuel injection speed given by the simulation was 42,4 m/s which is lower compared to the calculated value from Chapter 3.1.2. This would suggest that the injection area should be lowered. On the other hand, the pressure drop is very similar to the results from Chapter 3.1.2.

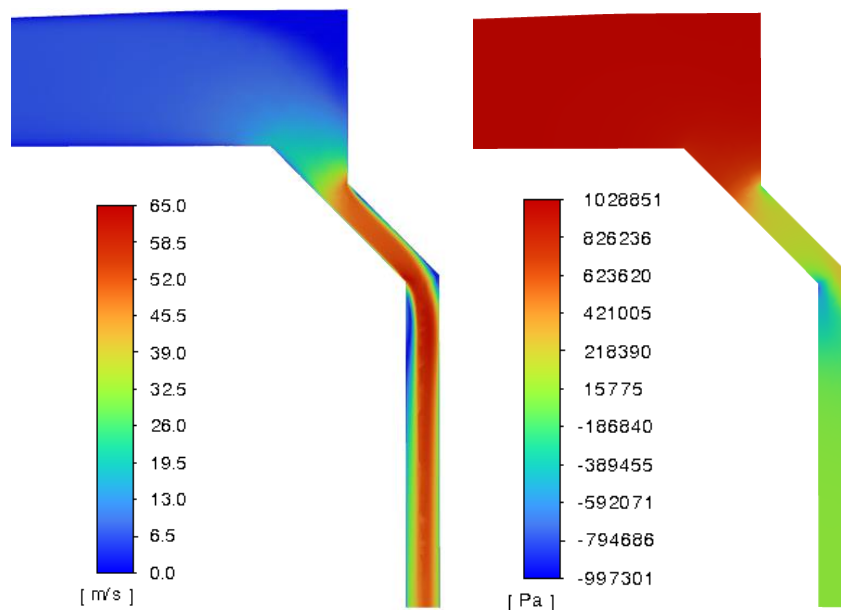


Figure 5.22 Ethanol injection parameters

Another result that can be taken from the simulation is the manifold pressure drop. *Figure 5.23* shows pressure profile in a cutout of the manifold with pressure scale limited around 10 bars. As we can see from the picture, the pressure drop along the manifold is almost negligible.



Figure 5.23 Manifold pressure losses

A second simulation with the same settings was created for the fuel manifold. The only change in this simulation was using water as the injection medium. Properties of water were once again taken from the Fluent library. This simulation was done as benchmark for cold flow testing. Since the first cold flows will be done with water, comparison to this simulation will be used to verify the simulation and decide the potential adjustments to the pintle position and annulus injection area. Velocity and pressure profiles in the annulus can be seen in *Figure 5.24*. The average injection speed through the annulus was 27,5 m/s. According to the simulation, the pressure drop for water cold flow should be equal to 6,6 bars.

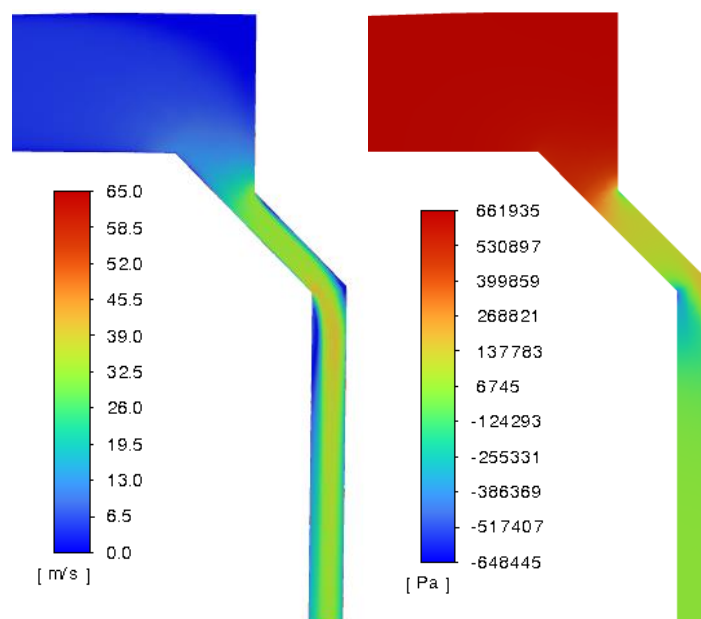


Figure 5.24 Fuel injection parameters for water

## 6 Testing campaign basis

To ensure the injector is safe to operate, complies with the competition rules and performs in accordance with our calculations a testing campaign will be proposed in this chapter.

### 6.1 Testing overview

The testing campaign will draw from our team experience with developing the hybrid engine. We will divide this campaign into three separate groups based on the general nature of the performed tests. Each group will be described in bigger detail in its own chapter. In order to accommodate the transition to our liquid engine, new testing infrastructure is going to be constructed and current infrastructure is going to be updated. Requirements on the infrastructure will be defined based on the needs of the testing campaign in the relevant chapters. We will also manufacture custom parts whenever needed to facilitate the testing. These parts will also be introduced in the relevant chapters.

The testing campaign will start with pressure testing of the injector assembly. This will ensure that manufactured parts have been designed and manufactured properly and verify their ability to withstand the expected pressure with required safety coefficients. Details of the pressure testing can be seen in Chapter 6.2

Next part of the campaign will be cold flow testing. Cold flows will serve to validate our simulations, calibrate the injector setting, obtain general data, test the support infrastructure, and aid in creation of the starting sequence. An example of a cold flow test performed on our hybrid engine injector can be seen in *Figure 6.1*. Methodology of cold flow testing will be further described in Chapter 6.3.

Last part of our testing campaign will be a series of hot fires. These will serve for final evaluation of the engine. Procedure and requirements for these tests will be described in Chapter 6.4.



Figure 6.1 Hybrid injector cold flow test [2]

## 6.2 Pressure testing

To ensure all critical load cases are covered, and that the injector complies with the competition rules, the assembly will be subjected to two separate qualification pressure tests. These tests are going to be done in our faculty laboratory and supervised by the faculty staff. The pressurisation is going to be done using a manual hydraulic pump which can be seen in *Figure 6.2*. The pressure will be measured in three different ways. By the pressure gauge present on the hydraulic pump, by the pressure transducer mounted to the pintle and connected to our team measuring cards and by a strain gauge mounted on the hydraulic cylinder connected to measuring equipment used by our faculty laboratory. These measurements are going to be compared for better accuracy.

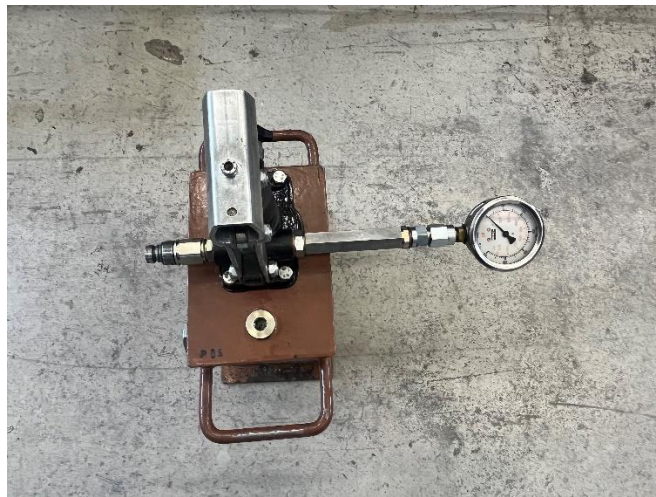


Figure 6.2 Manual hydraulic pump

During the first pressure test the pintle is going to be filled with water and pressurized up to MDP of 60 bars, ensuring this part is able to withstand 1,5 times the maximum expected operational pressure (MEOP). To connect the pressure transducer, while simultaneously connecting the hydraulic cylinder, a custom part will be manufactured. Model of this part can be seen in *Figure 6.3*. A set of strain gauges is going to be placed on the thinnest part of pintle wall to measure radial and tangential deformations. This gauge will be connected to the lab measuring equipment. Data from these gauges will be compared to our calculations and FEM analysis.

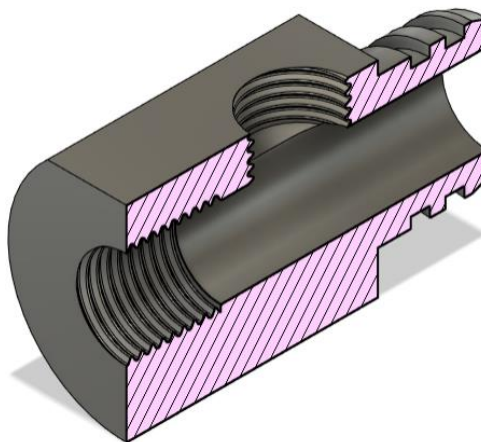


Figure 6.3 Pressure test adapter



During a second pressure test, the fuel manifold will be filled with water and pressurized up to MDP of 76 bars, which is 1,5 times larger than the maximum expected operating pressure (MEOP) for the highest possible pressure drop calculated in Chapter 3.1. During this test, the entire injector is going to be assembled. The pintle will be in a closed position. This test will not only ensure, that the injector face and the injector head are able to withstand the fuel pressure, but it will also ensure the pintle is able to withstand the outside pressure of the fuel during a fuel only cold flow. Strain gauges are going to be placed along the injector face and injector head. Data from these gauges will be compared to our calculations and FEM analysis. In order to distribute the water to the fuel manifold, a custom part called “Cold flow flange” is going to be manufactured. This part will substitute the chamber of the engine during our testing and will also be used in subsequent cold flows.

CAD image of the cold flow flange can be seen in *Figure 6.4*. This part will be manufactured using a welding robot. This manufacturing method has been chosen due to availability and simplification of design, where only one part needs to be manufactured. The material available for this part was stainless steel AISI 316L Since this part is for ground testing only, the higher weight is not a concern. The manufacturing method influenced the minimal wall thickness and shape of the ring channel, which has a distinct water drop shape to enable printing by layers.

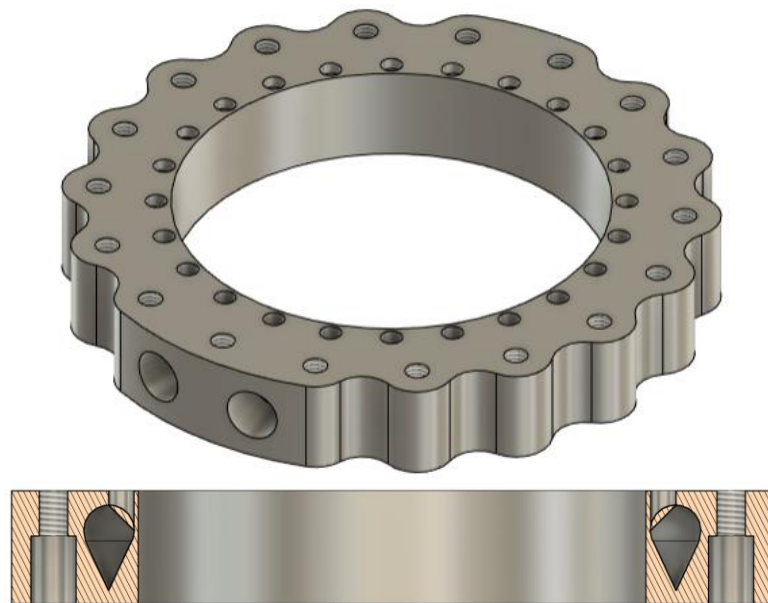


Figure 6.4 Cold flow flange

The whole testing procedure will be done in accordance with first qualification test article described in ECSS-E-SR-32-02C [36]. A full testing procedure created for all pressure tests can be seen in Appendix C.

### 6.3 Cold Flow

To ensure the injector performs as expected, a series of cold flows will be performed. These cold flows will be performed on our mobile engine test stand that is being developed.



Figure 6.5 Oxidizer only cold flow

To ensure we are able to perform all the necessary testing, we will form requirements on the test stand. These requirements will ensure, the stand will be able to service our engine. First, we will calculate the minimum volumes for propellant tanks to perform a full duration test. As mentioned in Chapter 1.3. The longest burn should not go above 8 s. The calculation can be seen in Equations (6.1) and (6.2).

$$V_{OXtank} = \frac{\dot{m}_{OX} \cdot t_{max}}{\rho_{OX}} = \frac{1,725 \cdot 8}{755} = 0,0182 \text{ m}^3 = 18,2 \text{ l} \quad (6.1)$$

$$V_{Ftank} = \frac{\dot{m}_F \cdot t_{max}}{\rho_F} = \frac{0,863 \cdot 8}{648} = 0,0107 \text{ m}^3 = 10,7 \text{ l} \quad (6.2)$$

Maximum operating pressures of both propellant tanks will be suggested. A value of 100 *bars* was chosen to give us the ability to test wide variety of operating pressures.

Pressure transducers were chosen for the purposes of our testing campaign. The selection was made based on past experience, measuring range, sensor output and price. The model chosen was AO027. This sensor has range to 100 *bars* and accuracy of 0,3% of full scale. [35]



Figure 6.6 Chosen pressure transducer [35]

A P&ID with suggested parameters was created. Elements of the P&ID will be referenced in the individual test procedures. The entire diagram can be seen in Appendix F.

A fuel only water cold flow will be used to verify our calculations from Chapter 3.1.2 and simulation results from Chapter 5.2.2. Multiple different operational pressures will be tested to analyse the performance of the fuel manifold. The initial operating pressure will be set to value calculated in Chapter 3.1.2. Fuel only water cold flows will be done with Cold flow flange which was introduced in Chapter 6.2 and can be seen in *Figure 6.4*. Pressures will be measured by the pressure transducers mounted to the cold flow manifold and fuel manifold. These sensors will be connected to our team measuring cards.

An oxidizer only water cold flow will be used to verify our calculations from Chapter 3.1.1 and simulation results from Chapter 5.2.1. Multiple different operational pressures will be tested to analyse the performance of the pintle. The initial operating pressure will be set to value calculated in Chapter 3.1. Pressure inside the pintle will be measured by the pressure transducer mounted to the pintle and connected to our team measuring cards.

Full water cold flow will be done to analyse at atomisation. Atomisation should be observed by high-speed camera end evaluated qualitatively. The initial operating pressure will be set to value resulting from previous cold flows. Pressures will be measured by the pressure transducers mounted to the cold flow manifold, fuel manifold and pintle. These sensors will be once again connected to our team measuring cards.

The final cold flow test will be propellant cold flow. The first propellant cold flow will be done with the cold flow flange. Pressures will be measured in the same manner as in the water cold flow. If this test is successful a second cold flow of the entire engine assembly will be done. Timing of the propellant injection is going to be recorded to create a starting sequence for hot fire of the engine. Pressures around the engine will be measured by pressure transducers mounted according to the schematic shown in *Figure 6.7* and connected to our team measuring cards. The difference in pressure between the engine manifold and the injector fuel manifold will give us an idea about pressure losses in the cooling channels. Operating pressures will be adjusted accordingly.

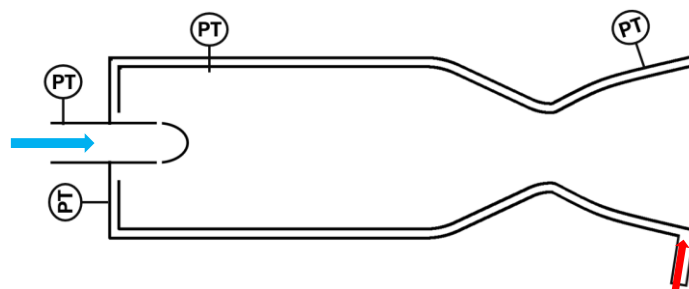


Figure 6.7 Pressure transducer placement [2] (*modified*)

General test procedure for all cold flow types can be seen in Appendix D.

## 6.4 Hot Fire

A final type of test in our campaign will be a so-called hot fire. Hot fire will be used for final evaluation of the engine and will be done with equipment from the final cold flow test with the full engine assembled. The operating pressures and countdown starting sequence will also be set during the final cold flow. The initial hot fire duration will be set to half of operational duration. In this case, the value will be 3s. Hot fire testing will be done exclusively on our test site in Bratronice. The testing site can be seen in *Figure 6.8*. Ignition of the engine will be done by a custom-made igniter which will be developed during future design work.



Figure 6.8 Bratronice test site [2]

We will measure pressures at locations determined in the final cold flow which are shown in Chapter 6.3. Additionally, we will measure temperatures along the outside of chamber the chamber wall, on the injector head and near two different bolt connections. These measurements will be done with PT1000 sensors connected to our team measuring cards. The exact location of these sensors will be decided before the hot fire test. Data obtained from the initial hot fire will be used to verify our calculations and assumptions. They will be also used for further design work.

The pressures will be compared our cold flow results, simulations and calculations and will be used to adjust the operating pressures and flowrates of the prototype based on the performance. The temperatures will help to evaluate the chamber cooling and determine the temperature of the bolted joint and injector head. This will show us the actual heat loading of the parts and allow us to adjust and improve our stress calculations for future iterations. If evaluation of data acquired during the initial hot fire proves it is safe to do so, a full duration hot fire will be performed.

We also have the ability to produce multiple test chambers, this gives us the opportunity to test variation in chamber characteristics like  $L^*$  and try different chamber cooling methods. If the cooling of the initial chamber proves to be sufficient, another hot fire with higher OF ratio or longer duration can be performed.

Every major update of the engine will undergo the entire testing campaign concluded with a hot fire test. A general test procedure created for hot fire testing can be seen in Appendix E.

## 7 Conclusion

In the beginning of the thesis, competition rules were analysed, and conceptual design of the engine was introduced. This gave us background for the injector development. Next, research of different injector types was done. The final research can serve as a starting ground for injector selection in future engines. Desirable and undesirable injector properties were identified, and optimum injector type was selected by a trade-off analysis. Once again, this trade-off analysis can serve as a blueprint for future injector concept selection.

In next chapter, design calculations were performed. The fuel calculations gave us the general dimensions necessary to achieve the desired thrust. We have chosen pressure drops and injections speeds which we will try to achieve. During fuel calculations a feature that can be used to tune the engine was introduced. A first concept of the injector was created, materials for all components were chosen, critical parts were identified and stress calculations for these parts were performed. These calculations served as a basis for our CAD model. We have also shown that all parts meet the competition and safety requirements.

3D model of the injector prototype was created based on the performed fluid calculations and stress requirements. Creation of the model was also governed by earlier experience with injector design. Locations of seals were identified, and specific sealing solution was chosen. Detailed features of the injector were created to ensure compatibility of the parts.

The FEM analysis of the assembly was performed. This analysis did not show any critical points of concern. The analysis has also shown that the engine should be able to withstand the expected loads during operation with prescribed safety margins. A CFD analysis was performed for the fuel manifold and for the pintle. CFD analysis of the fuel manifold showed results similar to our calculations. The pintle CFD analysis showed higher than expected pressure drop for the oxidizer. It was decided to go ahead with the current design and verify the simulation with a cold flow test. If the analysis is proven to be correct, design of the pintle is going to be adjusted. Another CFD of the pintle also showed overheating of the pintle tip for brass. This result was expected, and the material will be switched for the final design. In general, the simulations gave us an idea how the design might perform. We will build on these simulations during further development of the engine.

A test campaign was proposed along with requirements on the supporting infrastructure and data measurements. The collected data should give our team the possibility to evaluate the engine performance and confirm assumptions made during development. They will also serve to verify the simulations introduced in this thesis. Initial operating conditions were set and general procedures for all test types were created. The proposed procedures are universal and can be used for other liquid engines developed by our team. Engine which will successfully undergo the recommended test campaign will be qualified for operation.

Next course of action is going to be manufacturing and testing of the prototype. Based on the data obtained from the testing campaign, the design will be adjusted and modified. Thrust control can be studied during further work on the engine. When the engine reaches development maturity, it will be integrated into a new rocket for EuRoC competition. Development of this engine will serve as a cornerstone of future liquid rocket engine development by CTU Space Research.

# List of figures

Figure 1.1 Pressure fed cycle schematic [3] .....	14
Figure 1.2 Purdue Space Programme Liquids GSE [15] .....	15
Figure 2.1 Showerhead injector schematic [3].....	17
Figure 2.2 Most common impinging elements [11] .....	18
Figure 2.3 Triplet in bipropellant gas generator [5].....	18
Figure 2.4 F-1 engine with self-impinging injector .....	19
Figure 2.5 Configurations of quadlet and pentad [7] .....	19
Figure 2.6 Liquid rocket engine splash plate schematic [3].....	20
Figure 2.7 Pintle injector schematic [3].....	21
Figure 2.8 Recirculation zones created by the pintle injector [10].....	21
Figure 2.9 Thermal stress concentrated on the pintle tip [15].....	22
Figure 2.10 RS-25 engine schematic showing liquid/gas injection [16] .....	23
Figure 2.11 Coaxial injector element schematic diagram [4] .....	24
Figure 2.12 RS-25 main injector assembly [4] .....	24
Figure 2.13 Schematic of bi-swirl coaxial injector [14].....	25
Figure 2.14 Raptor engine schematic showing gas/gas injection [17] .....	25
Figure 2.15 Swirl element used by Copenhagen suborbitals [18].....	26
Figure 2.16 Schematic of a chosen injector type [19] .....	28
Figure 3.1 Injector discharge coefficients [4] .....	31
Figure 3.2 Movable pintle geometry [21] (edited).....	33
Figure 3.3 Relation between TMR and pray angle .....	34
Figure 3.4 Basic layout of the injector.....	39
Figure 3.5 Manufacturing of the first pintle prototype from brass.....	41
Figure 3.6 Galvanic table [26].....	41
Figure 3.7 Stress distribution in internally pressurized vessel [30] .....	42
Figure 3.8 Thread stripping failure [30].....	44
Figure 3.9 Injector face calculation schematic [2].....	45
Figure 3.10 Injector head calculation schematic [2] .....	48
Figure 3.11 Bolt parameters.....	52
Figure 4.1 Injector 3D model.....	57
Figure 5.1 Pintle FEM analysis mesh .....	58
Figure 5.2 Detail of the mesh around radial holes .....	59
Figure 5.3 Results of pintle FEM analysis .....	59
Figure 5.4 Stress concentration near radial holes .....	60
Figure 5.5 Manifold FEM mesh .....	61
Figure 5.6 Injector face von Mises stress .....	61
Figure 5.7 Injector face FEM detail.....	62
Figure 5.8 Injector head contact pressure.....	62
Figure 5.9 Stress distribution in the injector head .....	63
Figure 5.10 Stress distribution along the bolted connection .....	63
Figure 5.11 Detail of the stress concentration under the bolt head .....	63
Figure 5.12 Pintle CFD mesh.....	64
Figure 5.13 Detail of prism cells in radial hole .....	64
Figure 5.14 Detail of the pintle mesh .....	65
Figure 5.15 Pintle boundary conditions .....	65

Figure 5.16 Nitrous oxide injection parameters.....	66
Figure 5.17 Pintle injection parameters for water .....	66
Figure 5.18 Heat stress analysis of the pintle.....	67
Figure 5.19 Fuel manifold cutout .....	68
Figure 5.20 Fuel injection mesh .....	68
Figure 5.21 Manifold boundary conditions .....	69
Figure 5.22 Ethanol injection parameters .....	69
Figure 5.23 Manifold pressure losses.....	70
Figure 5.24 Fuel injection parameters for water.....	70
Figure 6.1 Hybrid injector cold flow test [2].....	71
Figure 6.2 Manual hydraulic pump.....	72
Figure 6.3 Pressure test adapter .....	72
Figure 6.4 Cold flow flange.....	73
Figure 6.5 Oxidizer only cold flow .....	74
Figure 6.6 Chosen pressure transducer [35] .....	74
Figure 6.7 Pressure transducer placement [2] .....	75
Figure 6.8 Bratronice test site [2].....	76

## List of tables

Table 1.1 Competition categories [1] .....	13
Table 1.2 Chosen CEA output data [2].....	16
Table 2.1 Selection criteria .....	27
Table 2.2 Grading of injector types .....	28
Table 2.3 Grading with weights .....	28
Table 2.4 Injector type selection summary .....	29
Table 3.1 Pintle sizing results.....	33
Table 3.2 Fuel sizing results .....	36
Table 3.3 Properties of selected materials .....	40
Table 3.4 Bolt connection configurations .....	52



## List of graphs

Graph 3.1 Relation between pressure drop and resulting spray angle .....	35
Graph 3.2 Fuel manifold design .....	38
Graph 3.3 Injector face stress distribution .....	47
Graph 3.4 Injector head stress distribution.....	50
Graph 5.1 Pintle tip temperature in time .....	67

## References

- [1] EUROOC. Rules and requirements [online]. Available at: <https://euroc.pt/rules-and-requirements/>
- [2] CTU Space Research internal documentation.
- [3] HEISTER, Stephen, William ANDERSON, Timothee POURPOINT a Joseph CASSADY. 2019. Rocket propulsion. Cambridge University Press. ISBN 978-1108422277.
- [4] Sutton, G. P. and Biblarz, O. (2001). Rocket Propulsion Elements. John Wiley & Sons.
- [5] Huzel, Dieter K. and Huang, David H. Modern Engineering for Design of Liquid-Propellant Rocket Engines. American Institute of Aeronautics and Astronautics, 1992.
- [6] HUZEL, D.K. and D.H. HUANG. 1967. Design of Liquid Propellant Rocket Engines. Second Edition. Technical Reports Server (NTRS).
- [7] GILL, G.S. a W.H. NURVICK. 1976. Liquid rocket engine injectors: NASA SP-8089.
- [8] ASHGRIZ, Nasser. 2011. Handbook of Atomization and Sprays. 2011th Edition. Springer. ISBN 978-1441972637.
- [9] SUTTON, George. 2005. History of Liquid Propellant Rocket Engines. AIAA. ISBN 978-1563476495.
- [10] Study on atomization and combustion characteristics of LOX/methane pintle injectors. 2017. Acta Astronautica 136.
- [11] STAR PUBLIC. Injectors [online]. Available at: <https://rocketry.gitbook.io/public/tutorials/p/propulsion/injectors>
- [12] Pintle injector [online]. Available at: <https://pintleinjector.blogspot.com/2016/12/pintle-injector.html>
- [13] Supercritical combustion of gas-centered liquid-swirl coaxial injectors for staged-combustion engines. 2018. Combustion and flame 197.
- [14] Experimental and Theoretical Study on Spray Angles of Bi-Swirl Coaxial Injectors. 2018. Journal of Applied Fluid Mechanics 11(5).
- [15] Purdue Space Program internal documentation
- [16] RS-25. 2024. Wikipedia: the free encyclopedia [online]. Wikimedia Foundation Available at: <https://en.wikipedia.org/wiki/RS-25>
- [17] Raptor engine. 2024. Wikipedia: the free encyclopedia [online]. Wikimedia Foundation. Available at: [https://en.m.wikipedia.org/wiki/File:Raptor\\_Engine\\_Unofficial\\_Combustion\\_Scheme.svg](https://en.m.wikipedia.org/wiki/File:Raptor_Engine_Unofficial_Combustion_Scheme.svg)
- [18] COPENHAGEN SUBORBITALS. Swirlers [online]. [cit. 2024-5-24]. Available at: <https://copenhagensuborbitals.com/swirlers/>
- [19] SUBEOM, Heo, Kim DAE HWAN and Yoon YOUNGBIN. 2022. Effects of Groove Structure on Spray Characteristics of a Throttleable Pintle Injector. JPP.
- [20] ECSS-E-ST-10C REV.1. System engineering general requirements. ESA-ESTEC, 15 February 2017n. I.

- [21] *Design Procedure of a Movable Pintle Injector for Liquid Rocket Engines*. 2017.
- [22] *ECSS-Q-ST-70-71C REV.1. Materials, processes and their data selection*. ESA-ESTEC, 15 October 2019n. I.
- [23] *iNerez* [online]. Available at: <https://www.inerez.cz/>
- [24] *ASM. Technical datasheets* [online]. Available at: <https://www.aerospacemetals.com/contact-aerospace-metals/>
- [25] *AALCO. Technical datasheets* [online]. Available at: <https://www.aalco.co.uk/datasheets/>
- [26] *MATWEB. Material property data* [online]. Available at: <https://www.matweb.com/index.aspx>
- [27] *Matmatch* [online]. [cit. 2024-5-24]. Available at: <https://matmatch.com/>
- [28] *CORROSIONPEDIA*. [online]. Available at: <https://www.corrosionpedia.com/>
- [29] *ECSS-E-HB-32-23A. Threaded fasteners handbook*. ESA-ESTEC, 16 April 2010n. I.
- [30] *Rotačně symetrické úlohy*. Available at: <https://docplayer.cz/36592968-Rotacne-symetricke-ulohy.html>.
- [31] *ŘEZNÍČEK, Jan. PRUŽNOST A PEVNOST II KOMENTOVANÉ PŘEDNÁŠKY. CTU in Prague*. Available at: [https://users.fs.cvut.cz/~simunale/PP\\_II\\_600\(2\).pdf](https://users.fs.cvut.cz/~simunale/PP_II_600(2).pdf)
- [32] *CPLABSAFETY. Viton chemical compatibility chart* [online]. Available at: <https://www.calpaclab.com/viton-chemical-compatibility-chart/>
- [33] *A numerical investigation into stripping failure of bolt assemblies at elevated temperatures*. 2020. *Structures* 27.
- [34] *PHISLINK. Coefficients of Friction* [online]. Available at: <https://www.physlink.com/reference/frictioncoefficients.cfm>
- [35] *AUTOSEN. Sensors, automation technology & solutions for Industry 4.0*. [online]. Available at: <https://autosen.com/cs/>
- [36] *ECSS-E-SR-32-02C. Structural design and verification of pressurized hardware*. ESA-ESTEC, 15 November 2008n. I.

# Appendixes

## Appendix A: Injector face calculation

Interval that describes the coordinates of the plate.

$$x \in (r_1; r_2)$$

The boundary conditions were set.

$$\begin{aligned}\varphi(r_2) &= 0 \\ \sigma_r(r_1) &= 0\end{aligned}$$

The used theory introduces general differential equation.

$$\left[ \frac{1}{x} \cdot (\varphi(x) \cdot x)' \right]' = -\frac{t(x)}{D}$$

For our case, loading per unit length is calculated.

$$t(x) = \frac{Q(x)}{2 \cdot \pi \cdot x} = \frac{q_0 \cdot \pi \cdot (x^2 - r_1^2)}{2 \cdot \pi \cdot x} = \frac{q_0 \cdot (x^2 - r_1^2)}{2 \cdot x}$$

Flexural rigidity of the flat plate can be expressed.

$$D = \frac{E \cdot h^3}{12 \cdot (1 - \nu^2)} = \frac{E^* \cdot h^3}{12}$$

Putting the equations above together gives us the following expression.

$$\left[ \frac{1}{x} \cdot (\varphi(x) \cdot x)' \right]' = -\frac{12 \cdot q_0 \cdot (x^2 - r_1^2)}{2 \cdot x \cdot E^* \cdot h^3}$$

We can make the following substitutions to simplify the calculation.

$$\begin{aligned}B &= \frac{6 \cdot q_0}{E^* \cdot h^3} \\ C &= \frac{6 \cdot q_0 \cdot r_1^2}{E^* \cdot h^3}\end{aligned}$$

Giving us a simplified expression.

$$\left[ \frac{1}{x} \cdot (\varphi(x) \cdot x)' \right]' = -B \cdot x + \frac{C}{x}$$

After first integration we get.

$$\frac{1}{x} \cdot (\varphi(x) \cdot x)' = -B \cdot \frac{x^2}{2} + C \cdot \ln(x) + C_1$$

We can move the variable  $x$  to the other side of the expression.

$$(\varphi(x) \cdot x)' = -B \cdot \frac{x^3}{2} + C \cdot x \cdot \ln(x) + C_1 \cdot x$$

During the second integration we will use per partes approach for the logarithm.

$$\int x \cdot \ln(x) dx$$

$$(uv)' = u'v + uv'$$

$$u = \ln(x)$$

$$u' = \frac{1}{x}$$

$$v' = x$$

$$v = \frac{x^2}{2}$$

$$uv' = (uv)' - u'v$$

$$\int uv' dx = uv - \int u'v dx$$

$$\int x \cdot \ln(x) dx = \frac{x^2 \cdot \ln(x)}{2} - \int \frac{x^2}{2} \cdot \frac{1}{x} dx = \frac{x^2 \cdot \ln(x)}{2} - \frac{x^2}{4}$$

Result of the entire integration.

$$\varphi(x) \cdot x = -B \cdot \frac{x^4}{8} + C \cdot \left( \frac{x^2 \cdot \ln(x)}{2} - \frac{x^2}{4} \right) + \frac{C_1 \cdot x^2}{2} + C_2$$

Final expression for bending angle of the plate can be seen below.

$$\varphi(x) = -\frac{B \cdot x^3}{8} + C \cdot \left( \frac{x \cdot \ln(x)}{2} - \frac{x}{4} \right) + \frac{C_1 \cdot x}{2} + \frac{C_2}{x}$$

Rate of angle change can be obtained by derivation and can be seen below.

$$\varphi'(x) = -\frac{3 \cdot B \cdot x^2}{8} + C \cdot \left( \frac{\ln(x)}{2} + \frac{1}{4} \right) + \frac{C_1}{2} - \frac{C_2}{x^2}$$

#### Calculation of the constants:

The first boundary condition prescribes.

$$\varphi(r_2) = 0$$

After imputing substituting know values, we get.

$$\varphi(r_2) = 0 = -\frac{B \cdot r_2^3}{8} + C \cdot \left( \frac{r_2 \cdot \ln(r_2)}{2} - \frac{r_2}{4} \right) + \frac{C_1 \cdot r_2}{2} + \frac{C_2}{r_2}$$

$$C_2 = \frac{B \cdot r_2^4}{8} - C \cdot \left( \frac{r_2^2 \cdot \ln(r_2)}{2} - \frac{r_2^2}{4} \right) - \frac{C_1 \cdot r_2^2}{2}$$

We can simplify the calculation by the following substitution.

$$K_1 = \frac{B \cdot r_2^4}{8} - C \cdot \left( \frac{r_2^2 \cdot \ln(r_2)}{2} - \frac{r_2^2}{4} \right)$$

We get expression for the first constant.

$$C_2 = K_1 - \frac{C_1 \cdot r_2^2}{2}$$

Now, we will use the boundary condition for radial stress.

$$\sigma_r(r_1) = E^* \cdot \frac{h}{2} \cdot \left( \varphi'(r_1) + v \cdot \frac{\varphi(r_1)}{r_1} \right)$$

$$\sigma_r(r_1) = 0$$

Inserting known expressions, we get.

$$\sigma_r(r_1) = 0 = E^* \cdot \frac{h}{2} \cdot \left\{ -\frac{3 \cdot B \cdot r_1^2}{8} + C \cdot \left( \frac{\ln(r_1)}{2} + \frac{1}{4} \right) + \frac{C_1}{2} - \frac{C_2}{r_1^2} + v \cdot \left[ -\frac{B \cdot r_1^2}{8} + C \cdot \left( \frac{\ln(r_1)}{2} - \frac{1}{4} \right) + \frac{C_1}{2} + \frac{C_2}{r_1^2} \right] \right\}$$

$$0 = -\frac{3 \cdot B \cdot r_1^2}{8} + C \cdot \frac{\ln(r_1)}{2} + \frac{C}{4} + \frac{C_1}{2} - \frac{C_2}{r_1^2} - \frac{v \cdot B \cdot r_1^2}{8} + \frac{v \cdot C \cdot \ln(r_1)}{2} - \frac{v \cdot C}{4} + \frac{v \cdot C_1}{2} + \frac{v \cdot C_2}{r_1^2}$$

We can make the following substitutions.

$$K_2 = -\frac{3 \cdot B \cdot r_1^2}{8} + C \cdot \frac{\ln(r_1)}{2} + \frac{C}{4} - \frac{v \cdot B \cdot r_1^2}{8} + \frac{v \cdot C \cdot \ln(r_1)}{2} - \frac{v \cdot C}{4}$$

The simplified expression is as follows

$$0 = K_2 + \frac{C_1}{2} - \frac{C_2}{r_1^2} + \frac{v \cdot C_1}{2} + \frac{v \cdot C_2}{r_1^2}$$

$$0 = K_2 + C_1 \cdot \left(\frac{1+v}{2}\right) + C_2 \cdot \left(\frac{v-1}{r_1^2}\right)$$

After substituting for the first constant, we get.

$$0 = K_2 + C_1 \cdot \left(\frac{1+v}{2}\right) + \left(K_1 - \frac{C_1 \cdot r_2^2}{2}\right) \cdot \left(\frac{v-1}{r_1^2}\right)$$

$$0 = K_2 + C_1 \cdot \left(\frac{1+v}{2} - \frac{r_2^2}{2} \cdot \frac{v-1}{r_1^2}\right) + K_1 \cdot \left(\frac{v-1}{r_1^2}\right)$$

To simplify we can make the following substitutions:

$$K_3 = \frac{1+v}{2} - \frac{r_2^2}{2} \cdot \frac{v-1}{r_1^2}$$

$$K_4 = K_1 \cdot \left(\frac{v-1}{r_1^2}\right)$$

After implementation the following expression is left.

$$0 = K_2 + C_1 \cdot K_3 + K_4$$

Giving us the expression for the constant.

$$C_1 = -\frac{K_2 + K_4}{K_3}$$

Finally, we can input the constants to equations for radial and tangential stress.

$$\sigma_r(x) = E^* \cdot \frac{h}{2} \cdot \left(\varphi'(x) + v \cdot \frac{\varphi(x)}{x}\right)$$

$$\sigma_t(x) = E^* \cdot \frac{h}{2} \cdot \left(\frac{\varphi(x)}{x} + v \cdot \varphi'(x)\right)$$

## Appendix B: Injector head calculation

The following boundary conditions need to be fulfilled:

$$\begin{aligned}\sigma_r^I(r_1) &= 0 \\ \varphi_I(r_2) &= \varphi_{II}(r_2) \\ \sigma_r^I(r_2) &= \sigma_r^{II}(r_2) \\ \sigma_r^{II}(r_3) &= 0\end{aligned}$$

### First section:

The first plate section has the following coordinate system.

$$x_I \in (r_1; r_2)$$

The used theory introduces general differential equation.

$$\left[ \frac{1}{x} \cdot (\varphi_I(x) \cdot x)' \right]' = -\frac{t(x)}{D}$$

For the first section, loading per unit length is calculated.

$$t(x) = \frac{Q(x)}{2 \cdot \pi \cdot x} = \frac{q_0 \cdot \pi \cdot (x^2 - r_1^2)}{2 \cdot \pi \cdot x} = \frac{q_0 \cdot (x^2 - r_1^2)}{2 \cdot x}$$

Flexural rigidity of the flat plate can be expressed.

$$D = \frac{E \cdot h^3}{12 \cdot (1 - \nu^2)} = \frac{E^* \cdot h^3}{12}$$

Putting the equations above together gives us the following expression.

$$\left[ \frac{1}{x} \cdot (\varphi_I(x) \cdot x)' \right]' = -\frac{12 \cdot q_0 \cdot (x^2 - r_1^2)}{2 \cdot x \cdot E^* \cdot h^3}$$

We can make the following substitutions to simplify the calculation.

$$\begin{aligned}B_I &= \frac{6 \cdot q_0}{E^* \cdot h^3} \\ C &= \frac{6 \cdot q_0 \cdot r_1^2}{E^* \cdot h^3}\end{aligned}$$

Giving us a simplified expression.

$$\left[ \frac{1}{x} \cdot (\varphi_I(x) \cdot x)' \right]' = -B_I \cdot x + \frac{C}{x}$$

After first integration we get.

$$\frac{1}{x} \cdot (\varphi_I(x) \cdot x)' = -B_I \cdot \frac{x^2}{2} + C \cdot \ln(x) + C_1$$

We can move the variable  $x$  to the other side of the expression.



$$(\varphi_I(x) \cdot x)' = -B_I \cdot \frac{x^3}{2} + C \cdot x \cdot \ln(x) + C_1 \cdot x$$

During the second integration we will use per partes approach for the logarithm.

$$(uv)' = u'v + uv'$$

$$u = \ln(x)$$

$$u' = \frac{1}{x}$$

$$v' = x$$

$$v = \frac{x^2}{2}$$

$$uv' = (uv)' - u'v$$

$$\int uv' dx = uv - \int u'v dx$$

$$\int x \cdot \ln(x) dx = \frac{x^2 \cdot \ln(x)}{2} - \int \frac{x^2}{2} \cdot \frac{1}{x} dx = \frac{x^2 \cdot \ln(x)}{2} - \frac{x^2}{4}$$

Result of the entire integration.

$$\varphi_I(x) \cdot x = -B_I \cdot \frac{x^4}{8} + C \cdot \left( \frac{x^2 \cdot \ln(x)}{2} - \frac{x^2}{4} \right) + \frac{C_1 \cdot x^2}{2} + C_2$$

Final expression for bending angle of the first plate section can be seen below.

$$\varphi_I(x) = -\frac{B_I \cdot x^3}{8} + C \cdot \left( \frac{x \cdot \ln(x)}{2} - \frac{x}{4} \right) + \frac{C_1 \cdot x}{2} + \frac{C_2}{x}$$

Rate of angle change can be obtained by derivation and can be seen below.

$$\varphi_I'(x) = -\frac{3 \cdot B_I \cdot x^2}{8} + C \cdot \left( \frac{\ln(x)}{2} + \frac{1}{4} \right) + \frac{C_1}{2} - \frac{C_2}{x^2}$$

### Second section:

Interval that describes the coordinates of the plate

$$x_{II} \in \langle r_2; r_3 \rangle$$

The used theory introduces general differential equation.

$$\left[ \frac{1}{x} \cdot (\varphi_{II}(x) \cdot x)' \right]' = -\frac{t(x)}{D}$$

For our case, loading per unit length is this time calculated as follows.

$$t(x) = \frac{Q(x)}{2 \cdot \pi \cdot x} = \frac{q_0 \cdot \pi \cdot (r_2^2 - r_1^2)}{2 \cdot \pi \cdot x} = \frac{q_0 \cdot (r_2^2 - r_1^2)}{2 \cdot x}$$

Flexural rigidity of the flat plate can be expressed.

$$D = \frac{E \cdot h^3}{12 \cdot (1 - \nu^2)} = \frac{E^* \cdot h^3}{12}$$

Putting the equations above together gives us the following expression.

$$\left[ \frac{1}{x} \cdot (\varphi_{II}(x) \cdot x)' \right]' = -\frac{12 \cdot q_0 \cdot (r_2^2 - r_1^2)}{2 \cdot x \cdot E^* \cdot h^3}$$

We can make the following substitution to simplify the calculation.

$$B_{II} = \frac{6 \cdot q_0 \cdot (r_2^2 - r_1^2)}{E^* \cdot h^3}$$

Giving us a simplified expression.

$$\left[ \frac{1}{x} \cdot (\varphi_{II}(x) \cdot x)' \right]' = -\frac{B_{II}}{x}$$

After first integration we get.

$$\frac{1}{x} \cdot (\varphi_{II}(x) \cdot x)' = -B_{II} \cdot \ln(x) + C_3$$

We can move the variable  $x$  to the other side of the expression.

$$(\varphi_{II}(x) \cdot x)' = -B_{II} \cdot x \cdot \ln(x) + C_1 \cdot x$$

During the second integration we will use per partes approach for the logarithm.

$$\int x \cdot \ln(x) dx$$

$$(uv)' = u'v + uv'$$

$$u = \ln(x) \quad u' = \frac{1}{x}$$

$$v' = x \quad v = \frac{x^2}{2}$$

$$uv' = (uv)' - u'v$$

$$\int uv' dx = uv - \int u'v dx$$

$$\int x \cdot \ln(x) dx = \frac{x^2 \cdot \ln(x)}{2} - \int \frac{x^2}{2} \cdot \frac{1}{x} dx = \frac{x^2 \cdot \ln(x)}{2} - \frac{x^2}{4}$$

Result of the entire integration.

$$\varphi_{II}(x) \cdot x = -B_{II} \cdot \left( \frac{x^2 \cdot \ln(x)}{2} - \frac{x^2}{4} \right) + \frac{C_3 \cdot x^2}{2} + C_4$$

Final expression for bending angle of the second plate section can be seen below.

$$\varphi_{II}(x) = -B_{II} \cdot \left( \frac{x \cdot \ln(x)}{2} - \frac{x}{4} \right) + \frac{C_3 \cdot x}{2} + \frac{C_4}{x}$$

Rate of angle change can be obtained by derivation and can be seen below.

$$\varphi_{II}'(x) = -B_{II} \cdot \left( \frac{\ln(x)}{2} + \frac{1}{4} \right) + \frac{C_3}{2} - \frac{C_4}{x^2}$$

### Calculation of the constants:

From the first boundary condition we get.

$$\sigma_r^I(r_1) = 0 = E^* \cdot \frac{h}{2} \cdot \left\{ -\frac{3 \cdot B_I \cdot r_1^2}{8} + C \cdot \left( \frac{\ln(r_1)}{2} + \frac{1}{4} \right) + \frac{C_1}{2} - \frac{C_2}{r_1^2} + v \cdot \left[ -\frac{B_I \cdot r_1^2}{8} + C \cdot \left( \frac{\ln(r_1)}{2} - \frac{1}{4} \right) + \frac{C_1}{2} + \frac{C_2}{r_1^2} \right] \right\}$$

$$0 = -\frac{3 \cdot B_I \cdot r_1^2}{8} + C \cdot \frac{\ln(r_1)}{2} + \frac{C}{4} + \frac{C_1}{2} - \frac{C_2}{r_1^2} - \frac{v \cdot B_I \cdot r_1^2}{8} + \frac{v \cdot C \cdot \ln(r_1)}{2} - \frac{v \cdot C}{4} + \frac{v \cdot C_1}{2} + \frac{v \cdot C_2}{r_1^2}$$

We can make the following substitution.

$$K_1 = -\frac{3 \cdot B_I \cdot r_1^2}{8} + C \cdot \frac{\ln(r_1)}{2} + \frac{C}{4} - \frac{v \cdot B_I \cdot r_1^2}{8} + \frac{v \cdot C \cdot \ln(r_1)}{2} - \frac{v \cdot C}{4}$$

Simplified equation for the first boundary condition can be written as.

$$0 = K_1 + \frac{C_1}{2} - \frac{C_2}{r_1^2} + \frac{v \cdot C_1}{2} + \frac{v \cdot C_2}{r_1^2}$$

$$0 = K_1 + C_1 \cdot \left(\frac{1 + \nu}{2}\right) + C_2 \cdot \left(\frac{\nu - 1}{r_1^2}\right)$$

The second boundary condition states that:

$$\sigma_r^{II}(r_3) = 0 = E^* \cdot \frac{h}{2} \cdot \left\{ -B_{II} \cdot \left(\frac{\ln(r_3)}{2} + \frac{1}{4}\right) + \frac{C_3}{2} - \frac{C_4}{r_3^2} + \nu \cdot \left[ -B_{II} \cdot \left(\frac{\ln(r_3)}{2} - \frac{1}{4}\right) + \frac{C_3}{2} + \frac{C_4}{r_3^2} \right] \right\}$$

We can start solving the equation

$$0 = -B_{II} \cdot \frac{\ln(r_3)}{2} + \frac{C}{4} + \frac{C_3}{2} - \frac{C_4}{r_3^2} - \frac{\nu \cdot B_{II} \cdot \ln(r_3)}{2} - \frac{\nu \cdot C}{4} + \frac{\nu \cdot C_3}{2} + \frac{\nu \cdot C_4}{r_3^2}$$

And make the following substitution.

$$K_2 = -B_{II} \cdot \frac{\ln(r_3)}{2} + \frac{C}{4} - \frac{\nu \cdot B_{II} \cdot \ln(r_3)}{2} - \frac{\nu \cdot C}{4}$$

Giving us another simplified expression.

$$0 = K_2 + \frac{C_3}{2} - \frac{C_4}{r_3^2} + \frac{\nu \cdot C_3}{2} + \frac{\nu \cdot C_4}{r_3^2}$$

$$0 = K_2 + C_3 \cdot \left(\frac{1 + \nu}{2}\right) + C_4 \cdot \left(\frac{\nu - 1}{r_3^2}\right)$$

Third boundary condition can be used as follows.

$$\varphi_I(r_2) = \varphi_{II}(r_2)$$

Substituting for bending angles.

$$-\frac{B_I \cdot r_2^3}{8} + C \cdot \left(\frac{r_2 \cdot \ln(r_2)}{2} - \frac{r_2}{4}\right) + \frac{C_1 \cdot r_2}{2} + \frac{C_2}{r_2} = -B_{II} \cdot \left(\frac{r_2 \cdot \ln(r_2)}{2} - \frac{r_2}{4}\right) + \frac{C_3 \cdot r_2}{2} + \frac{C_4}{r_2}$$

$$-\frac{B_I \cdot r_2^3}{8} + C \cdot \left(\frac{r_2 \cdot \ln(r_2)}{2} - \frac{r_2}{4}\right) + B_{II} \cdot \left(\frac{r_2 \cdot \ln(r_2)}{2} - \frac{r_2}{4}\right) = \frac{C_3 \cdot r_2}{2} + \frac{C_4}{r_2} - \frac{C_1 \cdot r_2}{2} - \frac{C_2}{r_2}$$

We can once again make a substitution.

$$K_3 = -\frac{B_I \cdot r_2^3}{8} + C \cdot \left(\frac{r_2 \cdot \ln(r_2)}{2} - \frac{r_2}{4}\right) + B_{II} \cdot \left(\frac{r_2 \cdot \ln(r_2)}{2} - \frac{r_2}{4}\right)$$

The result is a relatively simple equation.

$$K_3 = \frac{C_3 \cdot r_2}{2} + \frac{C_4}{r_2} - \frac{C_1 \cdot r_2}{2} - \frac{C_2}{r_2}$$

$$K_3 = \frac{C_3 \cdot r_2}{2} + \frac{C_4}{r_2} - \frac{C_1 \cdot r_2}{2} - \frac{C_2}{r_2}$$

The last boundary condition states that.

$$\sigma_r^I(r_2) = \sigma_r^{II}(r_2)$$

Substituting for radial stresses we get.

$$\begin{aligned} E^* \cdot \frac{h}{2} \cdot \left\{ -\frac{3 \cdot B_I \cdot r_2^2}{8} + C \cdot \left( \frac{\ln(r_2)}{2} + \frac{1}{4} \right) + \frac{C_1}{2} - \frac{C_2}{r_2^2} + v \cdot \left[ -\frac{B_I \cdot r_2^2}{8} + C \cdot \left( \frac{\ln(r_2)}{2} - \frac{1}{4} \right) + \frac{C_1}{2} + \frac{C_2}{r_2^2} \right] \right\} \\ = E^* \cdot \frac{h}{2} \cdot \left\{ -B_{II} \cdot \left( \frac{\ln(r_2)}{2} + \frac{1}{4} \right) + \frac{C_3}{2} - \frac{C_4}{r_2^2} + v \cdot \left[ -B_{II} \cdot \left( \frac{\ln(r_2)}{2} - \frac{1}{4} \right) + \frac{C_3}{2} + \frac{C_4}{r_2^2} \right] \right\} \\ -\frac{3 \cdot B_I \cdot r_2^2}{8} + C \cdot \frac{\ln(r_2)}{2} + \frac{C}{4} + \frac{C_1}{2} - \frac{C_2}{r_2^2} - \frac{v \cdot B_I \cdot r_2^2}{8} + \frac{v \cdot C \cdot \ln(r_2)}{2} - \frac{v \cdot C}{4} + \frac{v \cdot C_1}{2} + \frac{v \cdot C_2}{r_2^2} \\ = -B_{II} \cdot \frac{\ln(r_2)}{2} + \frac{C}{4} + \frac{C_3}{2} - \frac{C_4}{r_2^2} - \frac{v \cdot B_{II} \cdot \ln(r_2)}{2} - \frac{v \cdot C}{4} + \frac{v \cdot C_3}{2} + \frac{v \cdot C_4}{r_2^2} \\ -\frac{3 \cdot B_I \cdot r_2^2}{8} + C \cdot \frac{\ln(r_2)}{2} + \frac{C}{4} - \frac{v \cdot B_I \cdot r_2^2}{8} + \frac{v \cdot C \cdot \ln(r_2)}{2} - \frac{v \cdot C}{4} + B_{II} \cdot \frac{\ln(r_2)}{2} - \frac{C}{4} + \frac{v \cdot B_{II} \cdot \ln(r_2)}{2} \\ + \frac{v \cdot C}{4} = \frac{C_3}{2} - \frac{C_4}{r_2^2} + \frac{v \cdot C_3}{2} + \frac{v \cdot C_4}{r_2^2} - \frac{C_1}{2} + \frac{C_2}{r_2^2} - \frac{v \cdot C_1}{2} - \frac{v \cdot C_2}{r_2^2} \end{aligned}$$

We can simplify the equation by the following substitution

$$\begin{aligned} K_4 = -\frac{3 \cdot B_I \cdot r_2^2}{8} + C \cdot \frac{\ln(r_2)}{2} + \frac{C}{4} - \frac{v \cdot B_I \cdot r_2^2}{8} + \frac{v \cdot C \cdot \ln(r_2)}{2} - \frac{v \cdot C}{4} + B_{II} \cdot \frac{\ln(r_2)}{2} - \frac{C}{4} \\ + \frac{v \cdot B_{II} \cdot \ln(r_2)}{2} + \frac{v \cdot C}{4} \end{aligned}$$

Now the final expression can be written as.

$$\begin{aligned} K_4 = \frac{C_3}{2} - \frac{C_4}{r_2^2} + \frac{v \cdot C_3}{2} + \frac{v \cdot C_4}{r_2^2} - \frac{C_1}{2} + \frac{C_2}{r_2^2} - \frac{v \cdot C_1}{2} - \frac{v \cdot C_2}{r_2^2} \\ K_4 = -C_1 \cdot \frac{1+v}{2} + C_2 \cdot \frac{1-v}{r_2^2} + C_3 \cdot \frac{1+v}{2} - C_4 \cdot \frac{1-v}{r_2^2} \end{aligned}$$

We can rewrite the expression for all boundary conditions.

$$\begin{aligned} 0 &= K_1 + C_1 \cdot \left( \frac{1+v}{2} \right) + C_2 \cdot \left( \frac{v-1}{r_1^2} \right) \\ 0 &= K_2 + C_3 \cdot \left( \frac{1+v}{2} \right) + C_4 \cdot \left( \frac{v-1}{r_3^2} \right) \\ K_3 &= \frac{C_3 \cdot r_2}{2} + \frac{C_4}{r_2} - \frac{C_1 \cdot r_2}{2} - \frac{C_2}{r_2} \\ K_4 &= -C_1 \cdot \frac{1+v}{2} + C_2 \cdot \frac{1-v}{r_2^2} + C_3 \cdot \frac{1+v}{2} - C_4 \cdot \frac{1-v}{r_2^2} \end{aligned}$$

We express the first and third constant.

$$\begin{aligned} C_1 &= \frac{2}{1+v} \cdot \left[ C_2 \cdot \left( \frac{1-v}{r_1^2} \right) - K_1 \right] \\ C_3 &= \frac{2}{1+v} \cdot \left[ C_4 \cdot \left( \frac{1-v}{r_3^2} \right) - K_2 \right] \end{aligned}$$

And input them in the third equation.

$$K_3 = \frac{2}{1+v} \cdot \left[ C_4 \cdot \left( \frac{1-v}{r_3^2} \right) - K_2 \right] \cdot \frac{r_2}{2} + \frac{C_4}{r_2} - \frac{2}{1+v} \cdot \left[ C_2 \cdot \left( \frac{1-v}{r_1^2} \right) - K_1 \right] \cdot \frac{r_2}{2} - \frac{C_2}{r_2}$$

$$K_3 = \frac{r_2}{1+v} \cdot C_4 \cdot \left( \frac{1-v}{r_3^2} \right) - \frac{r_2}{1+v} \cdot K_2 - \frac{r_2}{1+v} \cdot C_2 \cdot \left( \frac{1-v}{r_1^2} \right) + \frac{r_2}{1+v} \cdot K_1 + \frac{C_4}{r_2} - \frac{C_2}{r_2}$$

$$K_3 + \frac{r_2}{1+v} \cdot K_2 - \frac{r_2}{1+v} \cdot K_1 = C_4 \cdot \left[ \frac{r_2}{1+v} \cdot \frac{1-v}{r_3^2} + \frac{1}{r_2} \right] + C_2 \cdot \left[ \frac{r_2}{1+v} \cdot \frac{v-1}{r_1^2} - \frac{1}{r_2} \right]$$

After some rearranging, we can make the following substitutions.

$$K_5 = K_3 + \frac{r_2}{1+v} \cdot K_2 - \frac{r_2}{1+v} \cdot K_1$$

$$K_6 = \frac{r_2}{1+v} \cdot \frac{1-v}{r_3^2} + \frac{1}{r_2}$$

$$K_7 = \frac{r_2}{1+v} \cdot \frac{v-1}{r_1^2} - \frac{1}{r_2}$$

Now we have a really simple equation.

$$K_5 = C_4 \cdot K_6 + C_2 \cdot K_7$$

We will do the same for the last equation.

$$K_4 = -\frac{2}{1+v} \cdot \left[ C_2 \cdot \left( \frac{1-v}{r_1^2} \right) - K_1 \right] \cdot \frac{1+v}{2} + C_2 \cdot \frac{1-v}{r_2^2} + \frac{2}{1+v} \cdot \left[ C_4 \cdot \left( \frac{1-v}{r_3^2} \right) - K_2 \right] \cdot \frac{1+v}{2} - C_4$$

$$\cdot \frac{1-v}{r_2^2}$$

$$K_4 = -C_2 \cdot \left( \frac{1-v}{r_1^2} \right) + K_1 + C_2 \cdot \frac{1-v}{r_2^2} + C_4 \cdot \left( \frac{1-v}{r_3^2} \right) - K_2 - C_4 \cdot \frac{1-v}{r_2^2}$$

$$K_4 + K_2 - K_1 = C_4 \cdot \left[ \frac{1-v}{r_3^2} - \frac{1-v}{r_2^2} \right] - C_2 \cdot \left[ \frac{v-1}{r_2^2} + \frac{1-v}{r_1^2} \right]$$

Again, we will make substitutions.

$$K_8 = K_4 + K_2 - K_1$$

$$K_9 = \frac{v-1}{r_2^2} + \frac{1-v}{r_3^2}$$

$$K_{10} = \frac{v-1}{r_2^2} + \frac{1-v}{r_1^2}$$

And obtain a final equation:

$$K_8 = C_4 \cdot K_9 - C_2 \cdot K_{10}$$

We can now express the second constant.

$$C_2 = \frac{C_4 \cdot K_9 - K_8}{K_{10}}$$

And solve the final equation.

$$K_5 = C_4 \cdot K_6 + \frac{C_4 \cdot K_9 - K_8}{K_{10}} \cdot K_7$$

$$K_5 = C_4 \cdot K_6 + \frac{C_4 \cdot K_9 \cdot K_7}{K_{10}} - \frac{K_8 \cdot K_7}{K_{10}}$$

$$K_5 + \frac{K_8 \cdot K_7}{K_{10}} = C_4 \cdot \left( K_6 + \frac{K_9 \cdot K_7}{K_{10}} \right)$$

$$K_{11} = K_5 + \frac{K_8 \cdot K_7}{K_{10}}$$

$$K_{12} = K_6 + \frac{K_9 \cdot K_7}{K_{10}}$$

$$K_{11} = C_4 \cdot K_{12}$$

$$C_4 = \frac{K_{11}}{K_{12}}$$

Now, we have solutions for all four constants.

Finally, we can input the constants to equations for radial and tangential stress.

$$\sigma_r(x) = E^* \cdot \frac{h}{2} \cdot \left( \varphi'(x) + v \cdot \frac{\varphi(x)}{x} \right)$$

$$\sigma_t(x) = E^* \cdot \frac{h}{2} \cdot \left( \frac{\varphi(x)}{x} + v \cdot \varphi'(x) \right)$$

# Appendix C: Pressure testing procedure



Project Deadalus



## Qualification Pressure Test Checklist

Date: \_\_\_\_\_

Responsible person: \_\_\_\_\_

Test MEOP: \_\_\_\_\_

Test MDP: \_\_\_\_\_

#	Item	Check
	Assembly checklists	
1.	<u>Pump checklist</u>	<input type="checkbox"/>
2.	<u>Data collection checklist</u>	<input type="checkbox"/>
3.	<u>Avionics checklist</u>	<input type="checkbox"/>
	Operation	
4.	<u>Visual inspection</u>	<input type="checkbox"/>
5.	<u>No personnel near test article</u>	<input type="checkbox"/>
6.	<u>Pressurization to MEOP</u>	<input type="checkbox"/>
7.	<u>30s dwell time</u>	<input type="checkbox"/>
8.	<u>Depressurization</u>	<input type="checkbox"/>
9.	<u>Test article at zero pressure</u>	<input type="checkbox"/>
10.	<u>Data acquisition check</u>	<input type="checkbox"/>
11.	<u>Visual leak inspection</u>	<input type="checkbox"/>
12.	<u>Pressurization to MDP</u>	<input type="checkbox"/>
13.	<u>30s dwell time</u>	<input type="checkbox"/>
14.	<u>Depressurization</u>	<input type="checkbox"/>

- 
- 15. Test article at zero pressure
  - 16. Data acquisition check
  - 17. Visual leak inspection
  - 18. Test complete

Signature: \_\_\_\_\_



# Appendix D: Cold flow testing procedures

---



Project Deadalus



## OX Water Cold Flow Test Checklist

Date: \_\_\_\_\_

Responsible person: \_\_\_\_\_

Pressurizer MEOP: \_\_\_\_\_

Oxidizer MEOP: \_\_\_\_\_

#	Item	Check
	Assembly checklists	
1.	<u>GSE Assembly checklist</u>	<input type="checkbox"/>
2.	<u>Test Stand Assembly checklist</u>	<input type="checkbox"/>
3.	<u>Leak Test checklist</u>	<input type="checkbox"/>
	Operation	
4.	<u>Switch to YELLOW state</u>	<input type="checkbox"/>
5.	<u>Regulators set</u>	<input type="checkbox"/>
6.	<u>Pressure QD connected</u>	<input type="checkbox"/>
7.	<u>Manual valves in "OPERATION" position</u>	<input type="checkbox"/>
8.	<u>All BV and PV valves CLOSED</u>	<input type="checkbox"/>
	Oxidizer tank fill	
9.	<u>Oxidizer tank plug removed</u>	<input type="checkbox"/>
10.	<u>Oxidizer tank filled with water</u>	<input type="checkbox"/>
11.	<u>Oxidizer tank plug secured</u>	<input type="checkbox"/>
12.	<u>Only critical personnel near test stand</u>	<input type="checkbox"/>
13.	<u>Switch to RED state</u>	<input type="checkbox"/>

- 
14. Pressure bottle (MV-N2-01) OPEN
  15. Reading on PG-N2-01 same as PT-N2-01
  16. No personnel near test stand   
Pressure tank fill
  17. Pressure fill (BV-N2-01) OPEN
  18. Pressure section (PT-N2-02) at MEOP
  19. Pressure fill (BV-N2-01) CLOSE
  20. Wait 30-60s observe Pressure tank pressure (PT-N2-02)
  21. PT-N2-02 stable   
Pressurisation
  22. Oxidizer high servo (BV-N2-03) OPEN
  23. Oxidizer tank pressure (PT-OX-02) at MEOP
  24. Countdown
  25. Main valve (PV-OX-01) OPEN
  26. IF main valve does not open go to line 29
  27. COLD FLOW   
System shutdown
  28. Tank pressures zero (PT-N2-02, PT-OX-02)
  29. Main valve (PV-OX-01) CLOSE
  30. Oxidizer high servo (BV-N2-03) CLOSE
  31. Pressure release (BV-N2-02) OPEN
  32. Critical personnel near test stand
  33. Pressure bottle (MV-N2-01) CLOSE
  34. No personnel near test stand
  35. Pressure fill (BV-N2-01) OPEN
  36. GSE pressures (PT-N2-01, PT-OX-01) at zero
  37. Pressure fill (BV-N2-01) CLOSE
  38. Pressure release (BV-N2-02) CLOSE

---

39. Switch to YELLOW state \_\_\_\_\_ □

40. Test complete

Signature: \_\_\_\_\_



# Project Deadalus



## F Water Cold Flow Test Checklist

Date: \_\_\_\_\_

Responsible person: \_\_\_\_\_

Pressurizer MEOP: \_\_\_\_\_

Fuel MEOP: \_\_\_\_\_

#	Item	Check
	Assembly checklists	
1.	<u>GSE Assembly checklist</u>	<input type="checkbox"/>
2.	<u>Test Stand Assembly checklist</u>	<input type="checkbox"/>
3.	<u>Leak Test checklist</u>	<input type="checkbox"/>
	Operation	
4.	<u>Switch to YELLOW state</u>	<input type="checkbox"/>
5.	<u>Regulators set</u>	<input type="checkbox"/>
6.	<u>Pressure QD connected</u>	<input type="checkbox"/>
7.	<u>Manual valves in "OPERATION" position</u>	<input type="checkbox"/>
8.	<u>All BV and PV valves CLOSED</u>	<input type="checkbox"/>
	Fuel tank fill	
9.	<u>Fuel tank plug removed</u>	<input type="checkbox"/>
10.	<u>Fuel tank filled with water</u>	<input type="checkbox"/>
11.	<u>Fuel tank plug secured</u>	<input type="checkbox"/>
12.	<u>Only critical personnel near test stand</u>	<input type="checkbox"/>
13.	<u>Switch to RED state</u>	<input type="checkbox"/>

- 
14. Pressure bottle (MV-N2-01) OPEN
  15. Reading on PG-N2-01 same as PT-N2-01
  16. No personnel near test stand   
Pressure tank fill
  17. Pressure fill (BV-N2-01) OPEN
  18. Pressure section (PT-N2-02) at MEOP
  19. Pressure fill (BV-N2-01) CLOSE
  20. Wait 30-60s observe Pressure tank pressure (PT-N2-02)
  21. PT-N2-02 stable   
Pressurisation
  22. Fuel high servo (BV-N2-04) OPEN
  23. Fuel tank pressure (PT-OX-02) at MEOP
  24. Countdown
  25. Main valve (PV-F-01) OPEN
  26. IF main valves do not open go to line 29
  27. COLD FLOW   
System shutdown
  28. Tank pressures zero (PT-N2-02, PT-F-02)
  29. Main valve (PV-F-01) CLOSE
  30. Fuel high servo (BV-N2-04) CLOSE
  31. Pressue release (BV-N2-02) OPEN
  32. Critical personnel near test stand
  33. Pressure bottle (MV-N2-01) CLOSE
  34. No personnel near test stand
  35. Pressure fill (BV-N2-01) OPEN
  36. GSE pressures (PT-N2-01, PT-F-01) at zero
  37. Pressure fill (BV-N2-01) CLOSE
  38. Pressue release (BV-N2-02) CLOSE

---

39. Switch to YELLOW state \_\_\_\_\_ □

40. Test complete

Signature: \_\_\_\_\_



# Project DeaDalus



## Water Cold Flow Test Checklist

Date: \_\_\_\_\_

Responsible person: \_\_\_\_\_

Pressurizer MEOP: \_\_\_\_\_

Test MEOP: \_\_\_\_\_

#	Item	Check
	Assembly checklists	
1.	<u>GSE Assembly checklist</u>	<input type="checkbox"/>
2.	<u>Test Stand Assembly checklist</u>	<input type="checkbox"/>
3.	<u>Leak Test checklist</u>	<input type="checkbox"/>
	Operation	
4.	<u>Switch to YELLOW state</u>	<input type="checkbox"/>
5.	<u>Regulators set</u>	<input type="checkbox"/>
6.	<u>Pressure QD connected</u>	<input type="checkbox"/>
7.	<u>Manual valves in "OPERATION" position</u>	<input type="checkbox"/>
8.	<u>All BV and PV valves CLOSED</u>	<input type="checkbox"/>
	Oxidizer tank fill	
9.	<u>Oxidizer tank plug removed</u>	<input type="checkbox"/>
10.	<u>Oxidizer tank filled with water</u>	<input type="checkbox"/>
11.	<u>Oxidizer tank plug secured</u>	<input type="checkbox"/>
	Fuel tank fill (when needed)	
12.	<u>Fuel tank plug removed</u>	<input type="checkbox"/>

- 
13. Fuel tank filled with water
  14. Fuel tank plug secured
  15. Only critical personnel near test stand
  16. Switch to RED state
  17. Pressure bottle (MV-N2-01) OPEN
  18. Reading on PG-N2-01 same as PT-N2-01
  19. No personnel near test stand
  - Pressure tank fill
  20. Pressure fill (BV-N2-01) OPEN
  21. Pressure section (PT-N2-02) at MEOP
  22. Pressure fill (BV-N2-01) CLOSE
  23. Wait 30-60s observe Pressure tank pressure (PT-N2-02)
  24. PT-N2-02 stable
  - Pressurisation
  25. Oxidizer high servo (BV-N2-03) OPEN
  26. Fuel high servo (BV-N2-04) OPEN
  27. Oxidizer tank pressure (PT-OX-02) at MEOP
  28. Fuel tank pressure (PT-OX-02) at MEOP
  29. Countdown
  30. Main valves (PV-OX-01 and PV-F-01) OPEN
  31. IF main valves do not open go to line
  32. COLD FLOW
  - System shutdown
  33. Tank pressures zero (PT-N2-02, PT-OX-02, PT-F-02)
  34. Main valves (PV-OX-01 and PV-F-01) CLOSE
  35. Fuel high servo (BV-N2-04) CLOSE
  36. Oxidizer high servo (BV-N2-03) CLOSE
  37. Pressure release (BV-N2-02) OPEN



- 
- 38. Critical personnel near test stand
  - 39. Pressure bottle (MV-N2-01) CLOSE
  - 40. No personnel near test stand
  - 41. Pressure fill (BV-N2-01) OPEN
  - 42. GSE pressures (PT-N2-01, PT-OX-01, PT-F-01) at zero
  - 43. Pressure fill (BV-N2-01) CLOSE
  - 44. Pressure release (BV-N2-02) CLOSE
  - 45. Switch to YELLOW state
  - 46. Test complete

Signature: \_\_\_\_\_



# Project Deadalus



## Cold Flow Test Checklist

Date: \_\_\_\_\_

Responsible person: \_\_\_\_\_

Pressurizer MEOP: \_\_\_\_\_

Oxidizer MEOP: \_\_\_\_\_

Fuel MEOP: \_\_\_\_\_

#	Item	Check
	Readiness checklists	
1.	<u>GSE Assembly checklist</u>	<input type="checkbox"/>
2.	<u>Test Stand Assembly checklist</u>	<input type="checkbox"/>
3.	<u>Leak Test checklist</u>	<input type="checkbox"/>
	Operation	
4.	<u>Switch to YELLOW state</u>	<input type="checkbox"/>
5.	<u>Regulators set</u>	<input type="checkbox"/>
6.	<u>Pressure QD connected</u>	<input type="checkbox"/>
7.	<u>Oxidizer QD connected</u>	<input type="checkbox"/>
8.	<u>Fuel QD connected</u>	<input type="checkbox"/>
9.	<u>Manual valves in "OPERATION" position</u>	<input type="checkbox"/>
10.	<u>All BV and PV valves CLOSED</u>	<input type="checkbox"/>
11.	<u>Only critical personnel near test stand</u>	<input type="checkbox"/>
12.	<u>Switch to RED state</u>	<input type="checkbox"/>
13.	<u>Pressure bottle (MV-N2-01) OPEN</u>	<input type="checkbox"/>

- 
14. Reading on PG-N2-01 same as PT-N2-01
  15. Oxidizer bottle (MV-OX-01) OPEN
  16. Reading on PG-OX-01 same as PT-OX-01
  17. Fuel bottle (MV-F-01) OPEN
  18. Reading on PG-F-01 same as PT-F-01
  19. No personnel near test stand   
Pressure tank fill
  20. Pressure fill (BV-N2-01) OPEN
  21. Pressurize pressure section (PT-N2-02) at MEOP
  22. Pressure fill (BV-N2-01) CLOSE
  23. Wait 30-60s observe Pressure tank pressure (PT-N2-02)
  24. PT-N2-02 stable
  25. Oxidizer high servo (BV-N2-03) OPEN
  26. Oxidizer tank pressure (PT-OX-02) at 30 bars
  27. Oxidizer high servo (BV-N2-03) Close   
Oxidizer tank fill
  28. Oxidizer fill (BV-OX-01) OPEN
  29. Oxidizer tank pressure (PT-OX-02) stabilised
  30. Oxidizer low servo (BV-OX-03) OPEN
  31. Oxidizer tank filled signal
  32. Oxidizer low servo (BV-OX-03) CLOSE
  33. Oxidizer fill (BV-OX-01) CLOSE   
Fuel tank fill
  34. Fuel fill (BV-F-01) OPEN
  35. Fuel low servo (BV-F-03) OPEN
  36. Fuel tank filled signal
  37. Fuel low servo (BV-OX-03) CLOSE
  38. Fuel fill (BV-F-01) CLOSE

- 
39. Data collection check
- Pressurisation
40. Oxidizer high servo (BV-N2-03) OPEN
41. Fuel high servo (BV-N2-04) OPEN
42. Oxidizer tank pressure (PT-OX-02) at MEOP
43. Fuel tank pressure (PT-OX-02) at MEOP
44. Start SIREN
45. Start Countdown
46. Main valves (PV-OX-01 and PV-F-01) OPEN
47. IF main valves do not open go to line 50
48. Cold flow
49. Data acquisition check
- System shutdown
50. Tank pressures at zero (PT-N2-02, PT-OX-02, PT-F-02)
51. Main valves (PV-OX-01 and PV-F-01) CLOSE
52. Fuel high servo (BV-N2-04) CLOSE
53. Oxidizer high servo (BV-N2-03) CLOSE
54. Pressure release (BV-N2-02) OPEN
55. Oxidizer release (BV-OX-02) OPEN
56. Fuel release (BV-F-02) OPEN
57. 5 minute wait, data check
58. Critical personnel near test stand
59. Pressure bottle (MV-N2-01) CLOSE
60. Oxidizer bottle (MV-OX-01) CLOSE
61. Fuel bottle (MV-F-01) CLOSE
62. No personnel near test stand
63. Pressure fill (BV-N2-01) OPEN
64. Oxidizer fill (BV-OX-01) OPEN

- 
65. Fuel fill (BV-F-01) OPEN
  66. 5 minute wait
  67. GSE pressures (PT-N2-01, PT-OX-01, PT-F-01) at zero
  68. Pressure fill (BV-N2-01) CLOSE
  69. Oxidizer fill (BV-OX-01) CLOSE
  70. Fuel fill (BV-F-01) CLOSE
  71. Pressure release (BV-N2-02) CLOSE
  72. Oxidizer release (BV-OX-02) CLOSE
  73. Fuel release (BV-F-02) CLOSE
  74. Switch to YELLOW state
  75. Test complete

Signature: \_\_\_\_\_

# Appendix E: Hot fire testing procedure



Project Daedalus



## Hot Fire Test Checklist

Date: \_\_\_\_\_

Responsible person: \_\_\_\_\_

Pressurizer MEOP: \_\_\_\_\_

Oxidizer MEOP: \_\_\_\_\_

Fuel MEOP: \_\_\_\_\_

#	Item	Check
	Readiness checklists	
1.	<u>GSE Assembly checklist</u>	<input type="checkbox"/>
2.	<u>Test Stand Assembly checklist</u>	<input type="checkbox"/>
3.	<u>Igniter checklist</u>	<input type="checkbox"/>
4.	<u>Leak Test checklist</u>	<input type="checkbox"/>
	Operation	
5.	<u>Switch to YELLOW state</u>	<input type="checkbox"/>
6.	<u>Regulators set</u>	<input type="checkbox"/>
7.	<u>Pressure QD connected</u>	<input type="checkbox"/>
8.	<u>Oxidizer QD connected</u>	<input type="checkbox"/>
9.	<u>Fuel QD connected</u>	<input type="checkbox"/>
10.	<u>Manual valves in "OPERATION" position</u>	<input type="checkbox"/>
11.	<u>All BV and PV valves CLOSED</u>	<input type="checkbox"/>
12.	<u>Only critical personnel near test stand</u>	<input type="checkbox"/>
13.	<u>Switch to RED state</u>	<input type="checkbox"/>

- 
14. Pressure bottle (MV-N2-01) OPEN
  15. Reading on PG-N2-01 same as PT-N2-01
  16. Oxidizer bottle (MV-OX-01) OPEN
  17. Reading on PG-OX-01 same as PT-OX-01
  18. Fuel bottle (MV-F-01) OPEN
  19. Reading on PG-F-01 same as PT-F-01
  20. No personnel near test stand   
Pressure tank fill
  21. Pressure fill (BV-N2-01) OPEN
  22. Pressurize pressure section (PT-N2-02) at MEOP
  23. Pressure fill (BV-N2-01) CLOSE
  24. Wait 30-60s observe Pressure tank pressure (PT-N2-02)
  25. PT-N2-02 stable
  26. Oxidizer high servo (BV-N2-03) OPEN
  27. Oxidizer tank pressure (PT-OX-02) at 30 bars   
Oxidizer tank fill
  28. Oxidizer fill (BV-OX-01) OPEN
  29. Oxidizer tank pressure (PT-OX-02) to stabilised
  30. Oxidizer low servo (BV-OX-03) OPEN
  31. Oxidizer tank filled signal
  32. Oxidizer low servo (BV-OX-03) CLOSE
  33. Oxidizer fill (BV-OX-01) CLOSE   
Fuel tank fill
  34. Fuel fill (BV-F-01) OPEN
  35. Fuel low servo (BV-F-03) OPEN
  36. Fuel tank filled signal
  37. Fuel low servo (BV-OX-03) CLOSE
  38. Fuel fill (BV-F-01) CLOSE

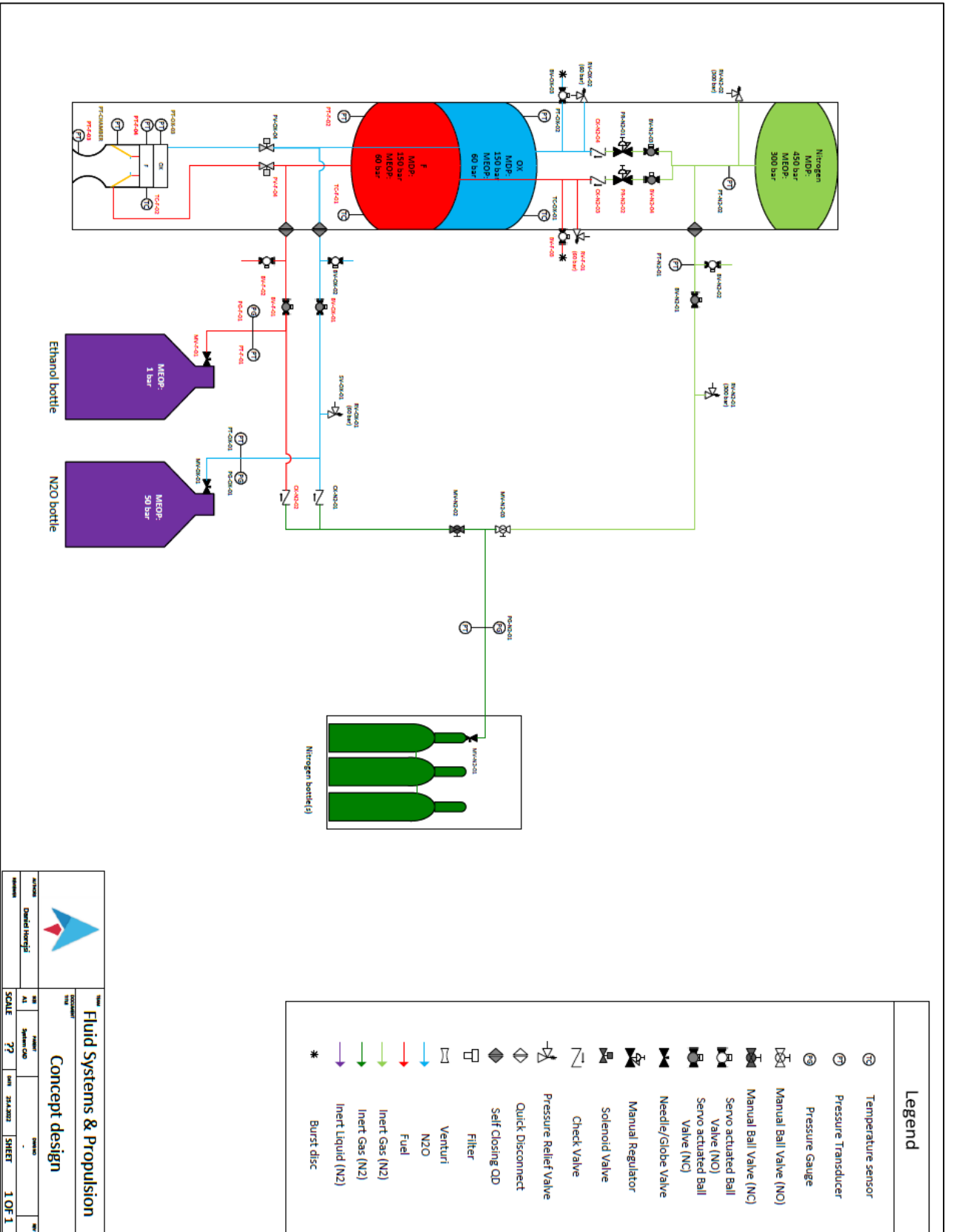
- 
39. Data collection check
- Pressurisation
40. Oxidizer high servo (BV-N2-03) OPEN
41. Fuel high servo (BV-N2-04) OPEN
42. Oxidizer tank pressure (PT-OX-02) at MEOP
43. Fuel tank pressure (PT-OX-02) at MEOP
44. Start SIREN
45. Start Countdown
46. Ignition
47. IF ignition fails go to line 51
48. Main valves (PV-OX-01 and PV-F-01) OPEN
49. Hot Fire
50. Data acquisition check
- System shutdown
51. Tank pressures zero (PT-N2-02, PT-OX-02, PT-F-02)
52. Main valves (PV-OX-01 and PV-F-01) CLOSE
53. Fuel high servo (BV-N2-04) CLOSE
54. Oxidizer high servo (BV-N2-03) CLOSE
55. Pressure release (BV-N2-02) OPEN
56. Oxidizer release (BV-OX-02) OPEN
57. Fuel release (BV-F-02) OPEN
58. 5 minute wait, data check
59. Critical personnel near test stand
60. Pressure bottle (MV-N2-01) CLOSE
61. Oxidizer bottle (MV-OX-01) CLOSE
62. Fuel bottle (MV-F-01) CLOSE
63. No personnel near test stand
64. Pressure fill (BV-N2-01) OPEN




- 
- 65. Oxidizer fill (BV-OX-01) OPEN
  - 66. Fuel fill (BV-F-01) OPEN
  - 67. 5 minute wait
  - 68. GSE pressures (PT-N2-01, PT-OX-01, PT-F-01) at zero
  - 69. Pressure fill (BV-N2-01) CLOSE
  - 70. Oxidizer fill (BV-OX-01) CLOSE
  - 71. Fuel fill (BV-F-01) CLOSE
  - 72. Pressure release (BV-N2-02) CLOSE
  - 73. Oxidizer release (BV-OX-02) CLOSE
  - 74. Fuel release (BV-F-02) CLOSE
  - 75. Switch to YELLOW state
  - 76. Test complete

Signature: \_\_\_\_\_

# Appendix F: Test stand P&ID



		<b>Fluid Systems &amp; Propulsion</b>	
		<b>Concept design</b>	
Drawn: <b>David Knight</b>	Scale: <b>??</b>	Sheet: <b>3A/33</b>	Sheet: <b>1 OF 1</b>